

Novel Interferometric Methods for
Characterization of Microscale
Components for External-Cavity
Semiconductor Lasers

Master of Science Thesis

ANDERS CAMENIUS

Department of Microtechnology and Nanoscience - MC2

Photonics Laboratory

CHALMERS UNIVERSITY OF TECHNOLOGY

Göteborg, Sweden, 2011

Abstract

External cavity lasers (ECL:s) have found widespread use in various applications, and many different wavelength tuning techniques have been demonstrated over the years. A novel wavelength tuning concept, utilizing longitudinal cavity dispersion provided by a diffractive optical element (DOE) has been invented by Dr. Kennet Vilhelmsson [1]. The laser design has been demonstrated and tested, but various aspects of the laser performance have not yet been fully understood. The work carried out in the master thesis project presented in this report has been focused on the characterization of the critical cavity components of the ECL functional prototype.

In the report, an overview of the field of external cavity lasers is given, as well as a presentation of different wavelength tuning methods found in the literature. The new concept for wavelength tuning (see [1]) is explained. The results from characterization of the external mirror and spectral measurement equipment are described. The external mirror properties are shown to fulfil the design criteria. However, the power reflectance is only about 87%, and the laser threshold could probably be reduced by choosing a mirror with slightly higher reflectance.

In this work, the first main issue has been to study the gain chip used in the laser, which was known to produce an astigmatic and elliptical beam. The design, assembly and test of a lateral shear interferometer for beam characterization is presented. The white-light compensated interferometer can be utilized to measure the astigmatism and beam parameters of the semiconductor gain medium. Test results from the interferometer are given, proving the functionality of the equipment. A method for extraction of the wavefront radius of curvature from captured interferograms by means of the Gabor transform was implemented. The full characterization of the gain chip still remains to be carried out, when the laser is assembled, so that the gain medium can be studied under lasing conditions.

The second important task of the project has been to study the properties of the diffractive optical element (DOE) used to provide the necessary longitudinal dispersion of the cavity. An experimental method for determination of the DOE focal length is introduced. The results show that the *relative* focal lengths of the four different elements available are in very good agreement with the design criteria. When the measured focal lengths are normalized to the measurement on the DOE with the longest focal length, and compared to normalized design values, the agreement is almost perfect.

When *absolute* focal lengths are considered, a discrepancy of 7-10% between the measured and intended values is detected. This observation can probably be explained from systematic errors in the measurement setup and difficulties in locating the focal points correctly from simple ocular inspections of camera images.

The most extensive part of the project has been to quantify the diffraction efficiency of the DOE. Only the DOE having the longest focal length has been subject to this investigation. A direct measurement technique, measuring the optical power in the principal diffraction order and comparing to the total power, has been tested. The estimated diffraction efficiency is found to be $77 \pm 5\%$ (including one Fresnel reflection). The value is rather uncertain due to limitations of the measurement method.

The need for a more robust way to measure the DOE efficiency was obvious, and led to the development of a self-interferometric measurement method. The idea is to measure the interference pattern formed by the overlapping diffraction orders from the DOE. A theoretical model of the DOE has been set up, which can be adjusted until the agreement with the measured data is as good as possible. In this way, the DOE profile can be determined, and the efficiency can be simulated when the micro-scale shape of the DOE is known. This method led to an estimation of the DOE diffraction efficiency of $82 \pm 2\%$ (including one Fresnel reflection). The measurement method can be modified to work for diffractive optical elements of arbitrary shape, as long as their diffraction orders overlap spatially.

Finally, the more robust DOE model mentioned above was used to simulate the behavior of the DOE focal length as a function of the wavelength, thus verifying the paraxial model of the DOE. The paraxial model is shown to overestimate the DOE focal length by about 3%. Also, data from the interferometric measurement were used to calculate the focal length for one of the DOEs, and after compensation for the 3% overestimation introduced by the paraxial model, the focal length is found to be only 0.75% from its design value. Hence, the combined results from this investigation and the previous focal length measurement indicate that the focal lengths of all four DOEs are very close to the intended design values.

Acknowledgements

First of all, I would like to thank my supervisor and chief, Dr. Kennet Vilhelmsson, for the opportunity to carry out my master thesis work at Alfa Exx AB, in the very stimulating research environment at his company. The importance of his encouraging support cannot be overestimated. The project to which I have had the privilege to contribute has implied many educative challenges and incentive investigations at the research front. Furthermore, I want to express my thankfulness to the engineers at Alfa Exx, especially Dr. Johan Backlund and Dr. Niklas Eriksson, who have always been available for fruitful discussions and heartening comments.

I must express my gratitude to my supervisor at Chalmers, Dr. Jörgen Bengtsson, who has been very supporting and has given invaluable contributions at difficult steps of the project. Further, my examiner, Prof. Anders Larsson, has given me the backing needed in order not to give up, for which I am very thankful. Special thanks also to Carl-Magnus Kihlman, for his unbeaten expertise in mechanical manufacturing.

Finally, I want to send many thanks to my friends, Gustav Bobeck and Johan Bondeson, for their support and never ceasing faith in me. My fellow students from the Photonics master programme, Martin Wahlsten and Erik Haglund, also deserve to be mentioned here; thank you for many hours of successful studies and joyful collaboration at Photonic Sundays and otherwise.

Contents

Abstract	i
Acknowledgements	ii
Key words	v
List of Symbols	v
List of Acronyms	vi
1 Introduction	1
1.1 Introduction to external-cavity lasers	1
1.2 Aim of the project	2
1.3 Method	3
1.4 Overview of thesis work and report	3
2 Wavelength tuning concepts in ECTLs	7
2.1 Tunable monolithic diode lasers	7
2.1.1 Various tuning techniques	7
2.1.2 Wide tuning	8
2.2 General aspects of external-cavity lasers	8
2.2.1 ECTL configurations	8
2.2.2 Characteristics of ECTLs	9
2.2.3 ECTLs in MEMS technology	9
2.3 Components of ECTLs	10
2.4 Wavelength tuning concepts of ECTLs	11
2.4.1 Mechanical tuning techniques	11
2.4.2 Electronic tuning techniques	13
2.5 ECL with longitudinal dispersion	14
2.5.1 Cavity setup	14
2.5.2 Longitudinal dispersion	16
2.5.3 Mode-hop free operation	17
3 Interferometer for beam characterization	19
3.1 Lateral shearing interferometry	20
3.2 Modified Jamin interferometer	20
3.3 Data evaluation	22
3.3.1 Sinusoidal fitting	24
3.3.2 Gabor transform filtering	24
3.4 Test of interferometer functionality	26
3.4.1 Determination of a lens focal length	26
3.4.2 Reference measurement on a known laser	29
3.4.3 Discussion and summary	32
4 Characterization of spectrometer and external mirror	33
4.1 Spectral characterization of fiber and spectrometer	33
4.2 External mirror characterization	35
5 Characterization of DOE	37
5.1 DOE effective focal length	37
5.1.1 Measurement setup and theory	37

5.1.2	Measurement results	38
5.1.3	Discussion and summary	40
5.2	DOE efficiency, direct measurement	40
5.2.1	Measurement setup	41
5.2.2	Total power at DOE	42
5.2.3	Power in the diffraction orders	43
5.2.4	Measurement without DOE	45
5.2.5	Summary and conclusions	46
5.3	DOE efficiency, interferometric measurement	47
5.3.1	Measurement setup	47
5.3.2	Model of the DOE	48
5.3.3	Model of the measurement setup	50
5.3.4	Interferogram examples	51
5.3.5	Results	53
5.3.6	DOE efficiency at $\lambda_0 = 770$ nm	56
5.3.7	Renewed investigation of DOE focal length	62
5.3.8	DOE profile depth	63
5.3.9	Discussion and summary	65
6	Discussion	67
7	Conclusions	69
7.1	ECL concept and functional prototype	69
7.2	Spectrometer and external mirror	69
7.3	Characterization of SOA	69
7.4	Characterization of DOE	70
7.4.1	DOE focal lengths	70
7.4.2	DOE efficiency	70
8	Further research	73
A	Theoretical derivations	75
A.1	Interpreting a lateral shear interferogram	75
A.2	Paraxial model of lens and DOE	76

Key words

External-cavity laser, ECL, ECTL, diffractive optical element, DOE, proximity effects, wavelength tuning, lateral shear interferometry, modified Jamin interferometer, diffraction efficiency, semiconductor optical amplifier, SOA, Gabor transform.

List of Symbols

c	Speed of light
f	Focal length, frequency
f_0	Design focal length
f_{DOE}	Focal length of the DOE
h	Planck's constant
I	Intensity, electrical current
k	Boltzmann's constant
k_0	Wave number
λ, λ_0	Wavelength, design wavelength
L_1, L_2	Cavity lens 1, 2
n_D	DOE index of refraction
n_g	Group index
ΔN	Charge carrier density
P	(Optical) power
q	Mode number
r	Radial coordinate
R	Wavefront radius of curvature, spectral reflectance
σ	$1/e$ half width of Gaussian function
S	Sensitivity
T	Temperature, spectral transmittance
U	Voltage
V	Visibility
W, W_0	Beam width, beam width at beam waist
x, y	Coordinates transverse to optical axis
z	Coordinate along optical axis
z_0	Rayleigh range

List of Acronyms

AFM	Atomic Force Microscope
AO	Acousto-Optic
AOM	Acousto-Optic Modulator
AR	Anti-Reflection
CCD	Charge Coupled Device
DBR	Distributed Bragg Reflector
DFB	Distributed Feedback
DOE	Diffraction Optical Element
ECL	External-Cavity Laser
ECTL	External-Cavity Tunable Laser
EO	Electro-Optic
FP (etalon)	Fabry-Perot (etalon)
FWHM	Full Width at Half Maximum
LED	Light-Emitting Diode
MEMS	Micro-Electro-Mechanical Systems
MMF	Multi-Mode Fiber
OD	Optical Density
PZT	Piezo-electric Transducer
QCL	Quantum Cascade Laser
RF	Radio Frequency
SMF	Single-Mode Fiber
SOA	Semiconductor Optical Amplifier
VCSEL	Vertical Cavity Surface-Emitting Laser
WBG	Waveguide Bragg Grating
WDM	Wavelength-Division Multiplexing

Chapter 1

Introduction

In this chapter, a short introduction to the field of external cavity lasers (ECLs) will be given, as well as the aim and methods of this master thesis project. Also, the scope of this report will be presented.

1.1 Introduction to external-cavity lasers

The demonstration by T. Maiman of the first laser in 1960 [2] was the starting point of a tremendous development. The laser is one of the key components for the the entire photonics industry and field of research. Lasers have found widespread use in the most diverse disciplines, such as telecommunication, metrology, industrial mass production, medicine, entertainment and military applications.

A vast number of different laser configurations have been developed over the years. The construction of the first semiconductor laser in 1962 [3] has subsequently led to the possibility to fabricate cheap, miniaturized, stable lasers for virtually any wavelength. The semiconductor laser is nowadays the most widely used laser of all, and a topic for intense research.

With time, developments in various fields of applications has led to new demands on coherent light sources. Fiber optical communication systems utilizing wavelength-division multiplexing (WDM) or coherent detection, high resolution spectroscopy, and precise coherent measurement techniques are some instances where semiconductor lasers must fulfil stringent requirements [4][5]; in particular: stable single mode operation, narrow line-width, wideband mode-hop free wavelength tunability, high speed, and insensitivity to environmental changes.

Various techniques to achieve longitudinal single-mode operation of a semiconductor laser exist; they all have in common that some kind of wavelength-dependent loss is introduced to suppress lasing at side modes. The distributed feedback (DFB) laser and the distributed Bragg reflector (DBR) laser are examples of devices exploiting such mechanisms [4]. When it comes to wavelength tunability, these lasers can indeed be tuned, but only by varying the injection current and/or the temperature of the diode [4]. This comes at the expense of variations in the optical output power and other characteristics of the laser radiation, and the tuning range is also rather limited.

The problem of limited continuous tuning range can be addressed in different ways. One way is to modify monolithic lasers by introducing additional sections in the structure, used for wavelength control. Wide tuning ranges can be achieved by more or less complicated methods. This is a large area of research, with many different techniques demonstrated over the years [6]. One main advantage is the possibility to integrate the laser and tuning elements in a very compact single monolithic structure. Also, no movable parts are needed for the wavelength tuning.

A different approach to the wide tuning issue is the *external-cavity laser* (ECL). These lasers have, for a long time, been the subject for great interest, as they offer an opportunity to meet the requirements outlined earlier using quite simple designs. The term "external cavity" refers to the fact that the resonant cavity is extended (often quite far) beyond the end facet(s) of the gain medium. The external cavity can be designed to have the required wavelength selective properties needed to force single-mode operation of the laser,

and also very narrow line-width. The long propagation distance in air outside the gain medium makes the laser very insensitive to variations in the refractive index of the semiconductor material, hence overcoming a well-known problem of solitary laser diodes [5].

In addition to the above, the ECL provides the possibility of wavelength tuning by altering the properties of the *external cavity itself*, thereby placing the wavelength selection mechanism *outside* the gain medium. This leads to very stable operation as well as a large number of ways to perform wavelength tuning, mechanically or electronically [4]. To stress the important aspect of wavelength tunability, the term external-cavity tunable laser (ECTL) will sometimes be used.

A few, by now classic, ECTL configurations are still dominating, although many other designs have been proposed and tested. As mentioned before, narrow line-width and single mode operation can be considered inherent of an ECL (if properly arranged). However, the different techniques utilized for wavelength tuning so far have proved to have various drawbacks. In particular, the concept of wide band continuous tunability remains a difficulty.

A number of methods to perform mode-hop free tuning have been proposed (an excellent review can be found in [4], and a more extensive survey is given in [7]). Mode-hop free tunable lasers are indeed commercially available, even as lab equipment [8][9], but usually are both costly and bulky. A simple and stable method for mode-hop free tuning of ECTLs, suitable for mass production, could reduce device cost and size of semiconductor ECTLs, thereby making them available as standard components for a huge number of applications. The foundation for this project is a new type of ECTL, utilizing "longitudinal dispersion" for continuous wavelength tuning [1], addressing the stability and ease-of-tuning issues. The concept is outlined in section 2.5.

1.2 Aim of the project

Extensive work has been carried out at Alfa Exx AB during the last 10 years to build a functional prototype of an ECTL with longitudinal dispersion, including build-up of a theoretical model of the laser gain medium, simulations of the laser cavity, design and manufacturing of a dispersive element, design and assembly of a prototype setup, and test and characterization of the wavelength tuning mechanism. Mode-hop free wavelength tuning over a bandwidth > 10 nm has been successfully demonstrated. Nonetheless, mode-hops have been observed when tuning is performed over a wider bandwidth, and the reason for this behavior is so far not understood, although various explanations have been proposed.

One of the more probable reasons for the observed mode-hopping could be the fact that the gain medium used in the cavity is an edge-emitting semiconductor optical amplifier (SOA), whose beam divergence is different in the lateral and transverse directions (a factor 2-3), and has a certain astigmatism as far as the beam waist locations in the two orthogonal directions are concerned. The idea is therefore that the existence of different focus positions in the x and y directions could give rise to mode-hops.

The aim of this master thesis project has been to develop techniques and tools for verification of the functionality of the components in the functional prototype external-cavity laser built at Alfa Exx AB in 2007. In order to improve the performance of the laser, the cavity components must be evaluated. If components deviate from the intended design, this might be part of an explanation to the observed unexpected behavior of the laser. Also, quantification of the possible errors is crucial in order to allow a new setup to be built, with a modified cavity, thus compensating for the measured imperfections.

The most important cavity components are the diffractive optical element (DOE) and the semiconductor gain chip, and these are subject to most of the attention in the project. In addition, the external mirror is examined. The project has been focused on the development of experimental techniques and equipment for measurements of the relevant parameters of these components. Also, one object has been to propose modifications to the functional prototype setup for improved stability and ease of measurements. Finally, as a smaller part of the project, an overview of the field of external-cavity lasers has been compiled, with the intention to look for designs similar to the Alfa Exx laser in recent research publications.

1.3 Method

As described above, the purpose of the thesis work has been to examine various aspects of the laser cavity components, and in order to make this possible, suitable experimental techniques, technical equipment and theoretical models have been developed. The method can be summarized in 8 different steps:

1. Identification of relevant component parameters for quantification.
2. Development of a theoretical framework, relating the parameters in question to measurable quantities.
3. Development of an experimental technique for measuring the quantities necessary.
4. Development of software tools for measured data analysis.
5. Design and assembly of an experimental setup.
6. Conduction of the experiment.
7. Evaluation of measured data by means of the software tool.
8. Interpretation of results, ultimately telling the performance of the component under test.

It has not always been possible to determine the performance of the component examined, due to different limitations in the preceding steps, and in these cases, the reasons for the shortcoming are discussed, and alternative/improved methods are proposed. Finally, a literature research has also been carried out in order to get a knowledge of external-cavity lasers in general, and to confirm the absence or identify the possible existence of a wavelength tuning concept similar to the Alfa Exx patent, in the laser research community.

1.4 Overview of thesis work and report

In this section, an outline of the different topics of this master thesis' work and report will be given, before results are presented from the major parts of the project in the following chapters.

Literature research

The first important step of the project has been to make a literature research, to get an orientation in the field of external-cavity lasers, in particular to give an overview of different wavelength tuning techniques. Also, the intension has been to look for ECTL designs similar to the concept with longitudinal dispersion described in the patent [1]. In chapter 2, the results from the literature study are presented. Also, the novel tuning technique [1] will be outlined in the last section of chapter 2.

Gain medium astigmatism

One important object in the project has been to develop a measurement technique to quantify the astigmatism and beam parameters of the SOA used in the system. When these parameters are known, their effect on the wavelength tuning characteristics could be calculated and compared to measurements. When knowledge of these quantities has been gained, possible changes in the cavity design could be proposed in order to overcome the unwanted phenomena related to the astigmatic gain medium. Consequently, as a part of the thesis work, a lateral shear interferometer for beam characterization has been designed, assembled and tested on a known laser. In addition, methods for extraction of the relevant information from the measured interferograms have been developed.

The interferometer is white-light compensated and is therefore functional also under non-lasing conditions. It can be used to study the naked SOA used in the ECL, although it is indeed questionable whether the beam parameters extracted from the amplified spontaneous emission of the SOA are representative for the characteristics of the SOA under lasing conditions in the external cavity. The intension has been to study the output beam from the lasing ECL. These experiments remain to be carried out, as the laser has not yet been assembled to the extent that a collimated output beam has been accessible during the project. The interferometer for beam characterization is described in chapter 3.

Laboratory setup design

Further, a few limitations in the functional prototype setup were identified during the laboratory work carried out a few years ago, and therefore, time has been spent during the thesis work to address these problems in the design of a new setup. First, the external mirror was mounted on a manual translation stage in the previous setup, which proved to be rather unstable, and repeatability was difficult to achieve. A piezo-electric translator (PZT) and some mechanical components were ordered. The PZT was vertically mounted, and the output beam emerged inside the PZT (which was not solid).

After verifying lasing and tunability with this new setup, further modifications were made in order to improve stability and add the possibility to collimate the divergent output beam. A flexure mount for high precision translation of the external mirror and a mechanical interface for mounting of a collimating lens behind the mirror were designed and ordered. Unfortunately, as most of the cavity components had to be characterized before assembly of the cavity, this last setup remains to be built and tested.

Spectrometer and external mirror

In order to study the spectral characteristics of the laser light, a spectrometer fiber must be inserted into the output beam. Reflections from the fiber end facets cannot be allowed to travel backwards into the laser, as even very small reflections may severely affect the laser behavior. A single-mode fiber was sent for polishing of both end facets at an angle, so that reflections will be deflected away from the laser. The fiber was then characterized and tested to verify functionality, and the sensitivity of the fiber-spectrometer system was measured in order to get a calibration curve for the measurement device. A short description of the result is given in chapter 4. The external mirror used in the test setup has also been spectrally characterized; the investigation is presented in the same chapter.

DOE focal lengths

Probably, the most important element of the cavity is the diffractive optical element (DOE). The characterization of this component has been the dominating task of the entire project, and several different investigations have been carried out to measure the DOE focal length and diffraction efficiency. Chapter 5 of this report is focused entirely on the DOE. First, a paraxial model of the foci locations of the DOE diffraction orders was developed, and subsequently, these locations were measured using some imaging optics and a CCD camera. The focal lengths were calculated from the model and compared to design parameters for the 4 different DOE designs available. This investigation is presented in section 5.1.

DOE diffraction efficiency

A very crucial aspect of the DOE is its diffraction efficiency, *i. e.*, how large fraction of the optical power incident on the DOE will be diffracted into the desired first order? Power ending up in other orders due to the DOE being non-ideal will contribute to the cavity loss factor. The antireflection coated lenses have very low loss (on the order of $< 0.4\%$ for each lens/air interface). The external mirror has a transmission factor of about 12%, but the mirror loss only contributes once per cavity roundtrip, and the loss represents the useful output beam. The DOE, on the other hand, is traversed twice per roundtrip, and a good DOE may still have a loss factor in the range of 10-20%. It is therefore important to measure the DOE efficiency, and any improvement of the DOE may give significantly reduced cavity loss.

As a first step, a direct measurement method for the DOE efficiency was developed and tested. The method and its results are presented in section 5.2. The idea is simple; assemble the entire ECL without the external mirror, and use a laser as light source. Measure the total power emerging from the DOE with an integrating detector. Then mount a small aperture on the detector and measure the power in the first diffraction order focus. The efficiency can then be immediately calculated.

The measurement as described in the previous paragraph was carried out, and the DOE efficiency could be estimated. However, the results are quite unreliable, as the method suffers from a number of problems. As absolute power levels are measured, it is crucial that the laser power is constant during the entire measurement. The output power of a free-running semiconductor laser usually drifts considerably over time due to

temperature variations and other factors. Hence, a monitor detector mounted behind the laser rear facet was used to control the optical output power and keep it constant.

Now, when a detector is inserted into the output beam, strong reflections will result, some of which will reach the monitor detector and disturb the power control. Even worse, when the detector is positioned close to the focus, it will act as nothing but an external mirror, coupling a lot of power back into the laser source itself, with chaotic resonant effects as a result. The problem could be slightly reduced by arranging a small air gap between the aperture and the detector surface, so that the reflection has diverged to some extent before going back through the pinhole, thereby truncating the reflected beam, but the direct measurement method is simply not very suitable for quantifying the DOE efficiency, let alone the small dimensions of the system, making it cumbersome to get access to the diffraction orders with the detector in the first place. These observations led to the conclusion that a better method must be found to determine the DOE efficiency.

It had been observed that the diffraction orders from the DOE are spatially overlapping, thus forming concentric ring-shaped interference patterns when the DOE is illuminated by a narrow-band light field. The idea was therefore born, that the relative amplitudes of the different diffraction orders could be calculated by recording intensity interferograms, and then setting up a theoretical model of the DOE, whose parameters could be adjusted until the measured interferograms were reproduced.

The work on this method has been the most extensive subproject of the thesis work, and started with the development of a simple model of the DOE where its diffraction orders were described as an ensemble of Gaussian beams. The difficulty with this model was how to relate the phases of the different orders to each other (which is necessary to determine the interference pattern). The DOE cannot be assumed to be an optically "thin" structure under these conditions. Therefore, a more robust model had to be developed, where the DOE is modeled as a structure having a physical depth, and also parameters describing the non-idealness due to the limited resolution of sharp edges in the manufacturing process. The model, the measurements and the results are outlined in section 5.3, and concludes the scope of this master thesis' work.

Chapter 2

Wavelength tuning concepts in ECTLs

2.1 Tunable monolithic diode lasers

A lot of work has been carried out in the field of monolithically integrated lasers. Distributed feedback (DFB) lasers and distributed Bragg-reflector (DBR) lasers are well-known devices. DFB lasers have become the standard in WDM optical communication systems due to their wavelength stability, narrow linewidth, ease of fabrication, high modulation speed and long-term reliability [7].

Different solutions to achieve wavelength tunability in monolithic diode lasers have been developed. Here, we will discuss some aspects of tuning principles in general, and then explain the idea behind wide-band tuning in monolithic diode lasers.

2.1.1 Various tuning techniques

Wavelength tuning in a monolithic laser can be realized by changing the effective gain spectrum of the diode, changing the comb-mode spectrum, or changing both these properties simultaneously [6]. The effective gain spectrum can be varied by affecting the medium gain, or using a tunable wavelength selective mirror. The comb-mode spectrum is varied by changing the optical length of the diode. As the physical length is generally fixed, this means that the effective mode index of the laser must be changed [6].

When the effective gain spectrum is varied, only discrete tuning can be achieved. The laser will operate at the wavelength experiencing the highest gain; when the gain spectrum is affected, the lasing wavelength is constant until a neighboring wavelength sees a higher gain. A mode hop will then occur. Hence, the lasing wavelength can only take discrete values, and one has no access to the spectrum between the peaks of the comb-mode spectrum [6].

If the comb-mode spectrum is made to drift, continuous tuning can be realized, but only up to the longitudinal mode spacing. A mode hop occurs whenever the drift becomes larger than the cavity free spectral range, as the laser will then prefer lasing in the neighboring mode. The difference compared to the gain-tuning scheme outlined above is that the comb-mode spectrum can be moved in arbitrarily small steps; this enables linear continuous wavelength tuning. In practice, the optical length of the structure is changed by tuning the refractive index of the structure. This can be achieved by either varying the charge carrier density ΔN , or the temperature T of the device [10]. Continuous tuning ranges of about 15 nm have been observed using carrier density tuning at $\lambda = 1550$ nm [10].

By combined tuning of both the gain and the comb-mode spectrum, a larger range of continuous tuning is possible. Tuning the gain, and making sure that the comb-mode spectrum is simultaneously shifted so that the same longitudinal mode is always at the gain peak, the laser can be tuned over a larger range without mode hopping [6].

2.1.2 Wide tuning

It can be shown that the continuous tuning range $\Delta\lambda$ for semiconductor lasers is limited to $\Delta\lambda/\lambda \approx \Delta n/n_g$, where Δn is the refractive index change and n_g is the effective group index [6]. This means that only about 15 nm continuous tuning is possible at normal operation [6]. This is far less than the available the gain spectrum, which can be over 100 nm wide. Other tuning methods have been developed to access a larger part of the gain spectrum. The idea is to utilize not the refractive index itself as the tuning parameter, but instead a refractive index *difference* [6].

Consider a semiconductor laser having two different wavelength selective mirrors at its ends. The mirrors are designed to have comb-like reflectance spectra, with quite sharp reflectance peaks. These two spectra are periodic, but the period of mirror 1 is slightly different from mirror 2. Lasing will occur at the wavelength where the reflectance peaks of the two mirrors overlap.

Now, by shifting the reflectance spectrum of, say, mirror 2, by a small amount, the wavelength of reflectance peak overlap shifts by a much larger amount. This is the so called Vernier effect [6]. Tuning the spectrum of both mirrors simultaneously, quasi-continuous tuning over a large spectral range can be realized [6].

2.2 General aspects of external-cavity lasers

Although some tuning can be achieved in a solitary laser diode, as described above, the external-cavity concept is essential to reach good performance of a tunable semiconductor laser [4]. In this section, we turn our interest to the important characteristics of an ECTL.

The concept of the external-cavity laser has been known since 1964 [4][11]. Many different designs have been demonstrated, but some of the earliest configurations are still being among the most widely used, namely the Littman and the Littrow types [4] (see section 2.3). Presently, much research is being conducted in the fields of quantum cascade lasers (QCLs) or vertical cavity surface emitting lasers (VCSELs) in external cavity configurations. Also, much interest is being directed to the implementation of ECTLs in MEMS technology [4][12]; this will be briefly discussed in section 2.2.3. New wavelength-tuning concepts are demonstrated every year, but still, quite many of these can be seen as modifications and improvements of the old designs used for a long time.

2.2.1 ECTL configurations

External-cavity tunable lasers can be categorized in 3 different main groups, depending on the configuration of the external cavity [13]. We shall here briefly mention these, before analyzing the various ways to achieve tuning and wavelength selectivity in an ECTL.

In the *extended-cavity*¹ configuration, one of the facets of the semiconductor amplifier is coated with an anti-reflection layer. Using collimating optics, a wavelength selective element and a feedback mirror, the cavity is extended beyond the gain medium. The back facet of the diode is left uncoated or is made (almost) 100% reflective. Hence, the cavity is extended in *one* direction compared to the solitary laser diode [13].

Extending the principle of the extended-cavity to *both* facets of the SOA, we get a *double-ended external-cavity* laser [13]. In this case, the optical feedback is positioned truly away from the gain medium. The main advantage of this configuration is that both SOA facet reflectivities are made small, which makes the laser less sensitive to the intrinsic modes of the diode [13]. On the other hand, the number of components are doubled compared to the (single-ended) extended-cavity, increasing system cost, complexity and loss factors.

Finally, if we "connect" the two arms of the double-ended ECL, we arrive at a *ring external-cavity* laser; a concept that is more difficult to realize in practice compared to the preceding ones, due to its increased sensitivity to misalignment [13].

¹Not all authors distinguish between the terms "extended" and "external" cavity. Both are being used to refer to the general concept of a cavity reaching beyond the semiconductor end facets.

2.2.2 Characteristics of ECTLs

In section 2.1, tuning of ordinary monolithic semiconductor lasers was introduced. External-cavity lasers have a number of advantages compared to the solitary diode laser. The most obvious characteristic of an ECL is the possibility of truly mode-hop free tuning. Tuning in ordinary diode lasers is complicated, and usually only quasi-continuous tuning can be achieved, especially if the entire gain bandwidth is used.

Another general feature of external-cavity lasers is that single-mode operation can be easily implemented [13]. In addition, the linewidth of an ECL is much smaller than for a solitary laser diode, due to the heavily enhanced photon life time resulting from using a long cavity [13]. Moreover, the wide gain bandwidth of the semiconductor can be fully exploited by placing the wavelength selective mechanism in the external cavity instead of inside the gain medium itself [13].

The behavior of a solitary diode laser is very much dependent on the ambient temperature, as well as the injection current. The reason is that the refractive index of the chip changes rapidly with these parameters, and the result will be phase fluctuations in the output optical field [4]. In contrast, an ECL will be highly insensitive to refractive index variations of the gain medium, due to the long propagation distance (usually in air) in the external cavity [4].

Of course, many different types of tunable lasers exist, and also many types of external-cavity lasers utilizing other gain media than a semiconductor. Compared to these competitors, the external-cavity semiconductor laser has the advantage of being small, being highly efficient, it needs only air cooling, it is electrically pumped, and it usually has a very long lifetime [13]. A possible drawback is that the output power is generally low, although high-power demonstrations have become more common with time [13].

2.2.3 ECTLs in MEMS technology

During recent years, the progress in the area of Micro-Electro-Mechanical Systems (MEMS) technology, has led to new possibilities for ECTL design. An excellent review of the field has been published by Liu and Zhang [12].

The MEMS implementation of ECTLs shows several advantages. In particular, ECLs can now be miniaturized, and mechanical tuning elements can be made very small in size, which in turn leads to enhanced modulation speed and robustness. Moreover, grating and mirror structures can be fabricated directly on micro-scale in arbitrary shapes, consequently making new laser configurations possible. Finally, the external cavity itself can be made extremely short when micro-fabrication methods are used (as short as 10 μm), heavily increasing the free spectral range of the ECL, and consequently making continuous tuning easier, as well as opening up new tuning regimes not reached before [12].

Various tuning schemes can be implemented in the MEMS technology. The simplest case is a SOA combined with a flat, tunable external mirror; the optical feedback is poor, but still some tuning is possible [12]. This principle can be improved by making the mirror curved in one direction, and adding a cylindrical lens in the orthogonal direction [12].

The MEMS technology has evolved rapidly during recent years, so that now some of the macroscopic designs discussed earlier have been realized on microscale; for instance, the Littrow, Littman, and Fabry-Perot etalon tuning principles have been demonstrated [14][15][16] (see section 2.4 for a description of these configurations).

The ultimate goal of MEMS external-cavity lasers is to fabricate all-integrated chips, containing the ECL with its laser diode, MEMS components and temperature control, as well as an optical fiber pig-tail and electronic drive circuits for operation of the laser. The results so far are promising, but much work still remains to be done [12].

2.3 Components of ECTLs

In this section, the common components in a (semiconductor) external-cavity laser are presented.

Semiconductor Optical Amplifier (SOA)

A semiconductor optical amplifier (SOA) is used as the gain medium in semiconductor ECTLs. Quantum well structures are commonly used, due to their low threshold current, broadband gain and the possibility to tailor the gain curve [4]. The SOA can be made from an ordinary edge emitting semiconductor laser, with one facet anti-reflection (AR) coated (the other facet is often used as the end mirror of the ECTL). The residual reflectance must be very small, usually on the order of 10^{-4} or smaller [4].

It is very difficult to achieve good facet reflectivity suppression over the entire tuning range, as the AR coating is optimized for a specific wavelength. This can in fact be the very limitation to the maximum available continuous tuning range, as the internal modes of the SOA causes the ECTL to mode hop [4]. The ECTL then behaves as two coupled cavities rather than a single one.

Collimating and beam shaping optics

Usually, some kind of positive lens is used to collimate the light emerging from the SOA. Many different kinds of lenses can be used to this end, and depending on the configuration of the laser, additional optics may be needed to shape the beam properly. One common design is the "cat's eye", comprising a positive lens and a concave or planar mirror (*i. e.*, the external mirror), a setup which becomes very insensitive to misalignment [17].

Optical isolator

ECTLs can be very sensitive to optical feedback into the cavity. Therefore, it is not uncommon to include some kind of optical isolator in the design [13], or other means of handling ghost reflections, in order to prevent potentially devastating back reflections.

Dispersive element

In order to achieve wavelength *selectivity*, the cavity must somehow be made dispersive. Of course, a natural dispersion is always present in the form of the wavelength dependent gain, but the dispersion must be correctly tailored to reach mode-hop free operation. In addition, to get the desired wavelength *tunability*, it must be possible to vary the dispersion, and the variation must be controlled in combination with other parameters, such as the cavity length, in order to avoid mode-hops. Many different devices for cavity dispersion have been utilized in ECLs, and section 2.4 is dedicated to this issue. For instance, diffraction gratings, acousto-optic modulators (AOMs) or electro-optically controlled filters may be used as dispersive elements.

External mirror

The external mirror is of course a key component in an external cavity. Metallic or dielectric mirrors can be used. Surfaces of other cavity components may also be used to give the desired feedback, for example the end facet of a fiber. Also, some ECTL designs do not need a specific mirror, for instance, the Littrow cavity design presented in figure 2.4.1 uses a grating for both wavelength selection and optical feedback. Thus, the grating effectively plays the role of an external mirror in this case. In any event, the external cavity must always provide the necessary optical feedback, be it from a true mirror, a grating or something else.

2.4 Wavelength tuning concepts of ECTLs

There are many different ways to implement wavelength tunability in an external-cavity laser. In this section, a number of methods will be presented. The classic designs in the Littrow and Littman configurations, respectively, are given rather a thorough description. Then, various other techniques will be briefly discussed.

The section is divided into "mechanical" and "electronic" tuning techniques, respectively. This distinction is neither universal nor very precise; some electronic tuning methods require some kind of mechanical movement as well, and many concepts are more or less complicated combinations of mechanical and electronic control principles. Nevertheless, the division into the two categories may still be useful in order to get some overview, and the presentation here focuses on rather "pure" tuning methods.

2.4.1 Mechanical tuning techniques

As mentioned above, the tuning methods can be either mechanical (physical movement of cavity components) or electronic (changing the dispersive properties of the cavity electronically). In this section, we are concerned with the former methods, the latter being considered in the next section.

Diffraction grating

There are two "classical" configurations utilizing movable diffraction gratings to perform tuning, namely the *Littrow* and *Littman*² versions, respectively [4]. Both are still widely used; for example, recent applications of ECTLs in the Littrow configuration have been demonstrated by Jechow *et al* [18] and Liu *et al* [19]. For a lately published investigation on an ECTL of the Littman type, see [20] or [21].

The basic Littrow ECTL configuration is shown in figure 2.4.1. The external cavity contains a collimating lens, and a reflection grating to provide optical feedback [4]. The grating angle is chosen so that the diffracted beam follows the same path as the incident beam, utilizing any diffraction order of the grating (usually the first order) [4]. Usually, the output beam is formed by the zeroth diffraction order, *i. e.*, the specular reflection from the grating, which will unavoidably contain some power due to imperfections of the grating.

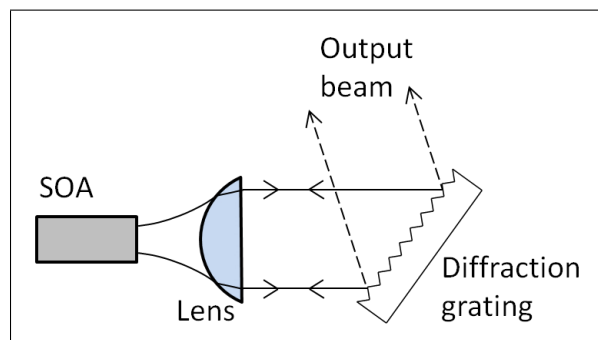


Figure 2.4.1: The Littrow configuration of an ECL.

The design is simple, as only two components are required apart from the SOA. Wavelength tuning is performed by rotating the grating, and relies on the fact that different wavelengths have different angles of diffraction. However, in order to avoid mode-hops, the cavity length must be adjusted simultaneously (by translation of the grating), so that the number of half wavelengths within the cavity is fixed. This makes continuous wavelength tuning cumbersome, although by no means impossible to achieve; see for instance [22] for a 40 nm continuously tunable ECL utilizing this technique.

Mode-hop free tuning can be realized by rotating the grating about an optimally chosen pivot point; in this way only one degree of freedom is necessary [23]. However, this advantage does not come for free; stable

²The Littman design is sometimes referred to as the Littman-Metcalf or the Grazing Incidence (GI) configuration.

rotation of the grating mounted on a fairly long arm is one issue, and it has also been shown that the laser performance is very sensitive to the exact location of the pivot point [23].

An additional drawback of the Littrow configuration is the angular change in direction of the output beam with the rotation of the grating. Alternatively, the rear facet of the SOA can be used for outcoupling [4]. In that case, the zeroth order diffracted beam will be useless, only adding cavity loss.

The Littman configuration addresses the inconvenience of the moving Littrow output beam, by introducing an extra mirror for optical feedback. A sketch of the Littman setup is shown in figure 2.4.2. The light from the SOA is incident on the grating at a high angle, and the first diffraction order is diffracted onto the mirror. The beam hits the external mirror at normal incidence, and the reflected beam will therefore follow its own path back into the SOA via the grating [4]. Wavelength tuning is now performed by rotation of the *mirror*. As different wavelengths emerge at different angles from the grating, only one wavelength will be incident normally on the mirror for a certain mirror angle; this wavelength will experience the highest optical feedback. The output beam, which is formed by the zeroth order diffracted beam just as in the Littrow case, remains stationary when the mirror rotates.

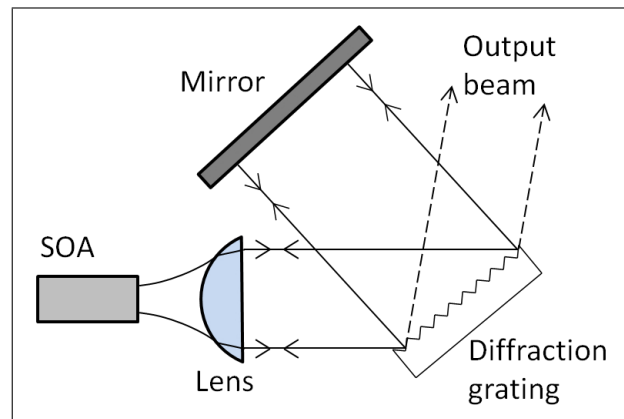


Figure 2.4.2: The Littman configuration of an ECL.

The problem of mode-hopping in the Littman ECTL is identical to the Littrow case; mode-hop free operation can be reached by rotating the mirror about a pivot point [4]. An additional feature of the Littman arrangement is its enhanced dispersive power, which is due to the grazing incidence of light on the grating. Hence, wavelength selectivity and side-mode suppression is improved compared to the Littrow type [4].

Distributed Bragg Reflector

A distributed Bragg reflector (DBR) is a periodic disturbance in the refractive index of a waveguide. An optical wave experiences strong feedback if the wavelength is equal to twice the period of the index variation. Hence, if the period of the index modulation can be tuned, the lasing wavelength is tuned as well. The change in the refractive index can be accomplished by both electronic and mechanical means.

Implementing mechanical tuning, a grating of varying pitch can be brought in contact with an optical fiber, polished so that part of the cladding is removed. The fiber serves as the external feedback section of the ECL. The grating is "fan-shaped", so that the grating period changes when walking along the grating lines. By sliding the grating over the polished fiber, the effective pitch of the feedback is varied. The evanescent field in the cladding senses the presence of the grating, which then plays the role of a DBR for the field in the waveguide [24].

In the electronic approach, the refractive index variation is written directly in a semiconductor waveguide, thus forming a waveguide Bragg grating (WBG). The feedback wavelength can then be varied by changing the global refractive index of the waveguide. Two different methods have been proposed; the index of refraction can be varied by either tuning the temperature [25] or through the electro-optic effect by applying an external voltage [26]. An extra phase-control section must be added in order to make the tuning mode-hop free.

Fabry-Perot etalon

Wavelength tuning can be accomplished by placing a Fabry-Perot (FP) etalon in the cavity [13]. The cavity feedback characteristics can be changed by either rotation of the etalon, or by varying the etalon mirror separation.

The etalon may also be combined with **more dispersive elements**, for example a grating [27], or a wavelength selective mirror [28][29]. The wavelength selection can be arranged so that either the etalon or the dispersive element provides the coarse and fine spectral resolution, respectively [13].

A combination of an etalon and a wavelength selective mirror of liquid-crystal type is demonstrated in [29] for a WDM system. Then, the periodic structure of sharp transmission peaks of the etalon allows an ensemble of lasing modes over the entire tuning bandwidth. The wavelength selective mirror has a rather slowly varying reflectance, and can be tuned so that only a specific mode of the etalon is allowed to lase. The etalon provides side-mode suppression close to the lasing mode, and the mirror gives suppression of the adjacent modes of the etalon. Finally, a phase-control section in the gain chip is needed in order to avoid adjustments of the cavity length.

Interference filter

An interference filter can be used as the wavelength selective element in the external cavity [30]. By tilting the filter, its favored transmission wavelength is varied. The filter can be designed to be narrow-band enough to force single-mode lasing. In practice, the wavelength tuning by tilting of the filter must be accompanied by an appropriate cavity length adjustment if mode-hops should be avoided; continuous tuning was not mentioned in [30].

2.4.2 Electronic tuning techniques

Mechanical tuning, although simple as it might appear, is associated with a number of drawbacks; in particular, it is difficult to achieve stable operation and high speed tunability, simply because of bulky moving mechanical parts. These problems can be overcome by turning to electronic tuning principles, a concept that will be discussed in this section.

Birefringent filter

Wavelength tuning by means of a birefringent filter has been reported. Tuning can be either mechanical or electronic, but electronic tuning is the more common choice [13]. A well-known solution utilizes *Lyot filters*, (a Lyot filter consists of a birefringent plate and a polarizer). A number of such filters are mounted in a stack. The plate thicknesses are not equal, but if properly chosen, the entire structure will show narrow transmission bands separated by quite a large free spectral range. To make the filter electronically tunable, the birefringence of the plates must be controlled. This can be done by exploiting the electro-optic effect, or by using liquid crystal cells as birefringent plates [13].

Electro-optic filter

The electro-optic (EO) effect can be a tool for wavelength tuning. The EO effect is the dependence of the index of refraction on an applied external voltage. By positioning of an EO crystal inside the external cavity, the effective length of the cavity can be varied (through the variation of the optical path length in the crystal). The number of half wavelengths in the cavity will then change accordingly, and the mode-hop free tuning range will therefore be rather limited [4]. It can, however, be enhanced by making the EO crystal thin and slightly wedge-shaped; in such a setup, comprising a Littrow grating as feedback element, a continuous tuning range of 50 GHz at $\lambda = 793$ nm was achieved [31].

Acousto-optic filter

An acousto-optic modulator (AOM) can be used for wavelength tuning. The AO device is arranged so that it scatters linearly polarized light into the orthogonal polarization by diffraction from a traveling acoustic wave [4]. The diffraction efficiency is strongly wavelength dependent (reaching its maximum when the Bragg condition for reflection from a periodic structure is fulfilled), and the peak wavelength of the diffraction can be varied by changing the RF frequency of the AO modulator. This makes wavelength tuning possible. The fast response of the AO device is an important aspect of this ECL design; recently, tuning over 90 GHz with a speed of $0.47 \text{ GHz}/\mu\text{s}$ and a repetition rate of 2.5 kHz has been demonstrated [32].

An inherent problem with the AO technique is the Doppler shift associated with the diffracted wave [13]. To compensate for this frequency shift, an extra AO device, providing an equally large but opposite shift can be used [32][33], although this makes the design somewhat complicated.

2.5 ECL with longitudinal dispersion

A new wavelength-tuning concept for mode-hop free operation of an ECL has been proposed [1]. This ECL design utilizes longitudinal dispersion, provided by a transmissive diffractive optical element (DOE). The concept will be described in this section, as well as its advantages and possible difficulties. No wavelength tuning concept similar to [1] has been found in the literature, but the author does not claim to have conducted a very extensive research.

2.5.1 Cavity setup

The cavity design contains a semiconductor optical amplifier (SOA), having one of its facets antireflection coated, a collimating lens L_1 , a focusing lens L_2 , a diffractive optical element (DOE), and an external mirror. A sketch of the setup is shown in figure 2.5.1. The setup is of the single-ended extended-cavity type (see section 2.2.1). Disregarding the DOE for the moment, this system is in itself a very stable laser. The output facet of the SOA is imaged onto the external mirror. Therefore, it will also be imaged onto itself after one roundtrip in the cavity, and this is true even if the components of the system are misaligned, due to the reciprocity of an imaging system. Hence, this is a robust laser setup even without the DOE.

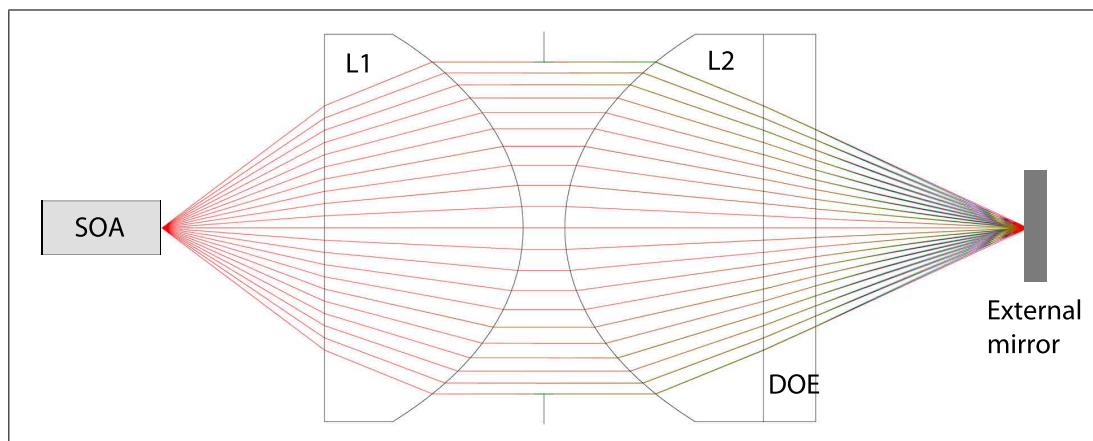


Figure 2.5.1: A sketch of the ECL design described in [1]. Picture from [34] (the SOA and the mirror have been added).

In figures 2.5.2 and 2.5.3, photos of the laser lab setup are presented. Adjustment screws are used to align the cavity components to each other, and tiny springs keep each component in place until the adjustment has been completed. Then, the component is fastened with small screws, and one proceeds to align the next component.

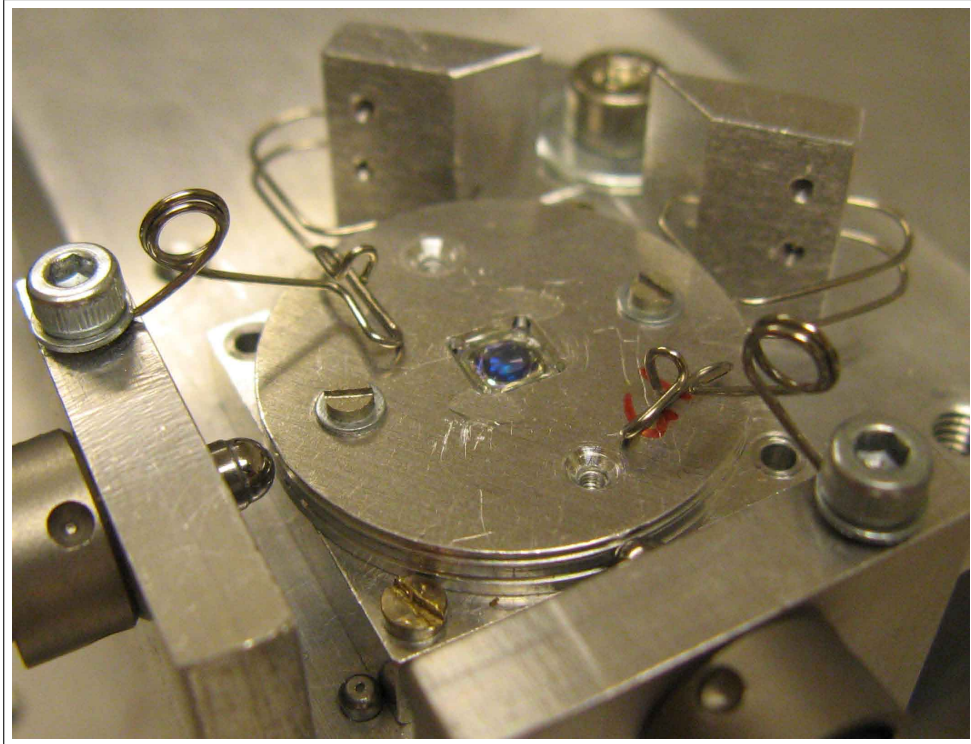


Figure 2.5.2: A photo of the lab setup of the laser with longitudinal dispersion. The optical axis is in the vertical direction.

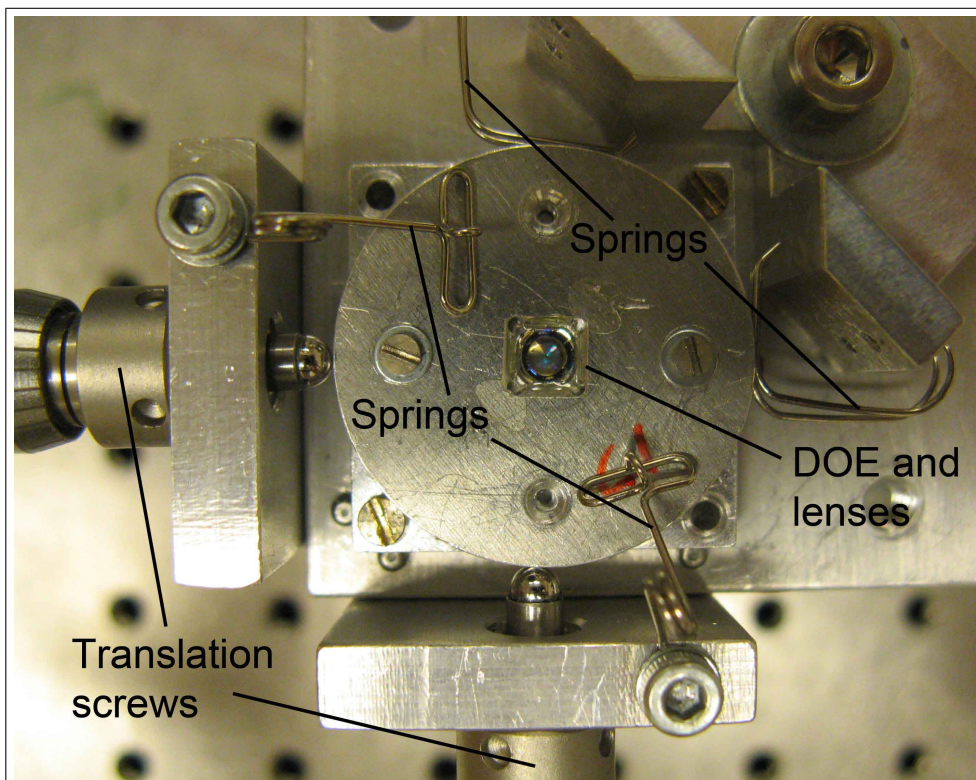


Figure 2.5.3: A photo of the lab setup of the laser with longitudinal dispersion, looking along the optical axis. The adjustment screws and springs are visible in the figure. The diameters of the Aluminum disc-shaped lens and DOE holders are about 25 mm.

2.5.2 Longitudinal dispersion

The new ECL design relies on "longitudinal dispersion", in contrast to most ECL types where the dispersion acts transverse to the length direction of the laser. For instance, the Littrow laser design in figure 2.4.1 utilizes the fact that only one wavelength will be reflected exactly backwards from the grating. All other wavelengths are diffracted at different angles (in the "transverse" direction), therefore experiencing higher loss.

In the ECL design [1], the DOE gives the desired dispersion of the cavity; however, it does not act as a grating, but rather as a very dispersive negative lens. The symmetry around the optical axis of the system will then be preserved regardless of wavelength, but different wavelengths will be focused at different points on the optical axis to the right of the DOE in figure 2.5.1. Hence the nomenclature *longitudinal dispersion*.

In figure 2.5.4, the situation at the external mirror for 3 different wavelengths is depicted. The picture shows that these wavelengths are focused to different points on the optical axis. When the mirror is inserted, one wavelength will have its focus exactly on the mirror, and will form an image of the laser output facet. When reflected from the mirror, this wavelength will be imaged back into the SOA. All other wavelengths will be defocused to some extent, and will therefore experience higher cavity loss. This gives the wavelength selection mechanism of the cavity.

The amount of defocus for unwanted wavelengths governs the cavity loss profile, and therefore the side-mode suppression. The defocus of a certain wavelength is determined by two parameters: the "average" angle of divergence of the optical field, and the dispersive power of the DOE. If the DOE has high dispersion, the focus of the *undesired* wavelength will be located a large distance away from the focus of the *desired* laser mode. The angle of divergence decides the amount of defocus of the undesired wavelength at the mirror. High divergence means strong defocus. The angle of divergence is given by the focal lengths of the DOE and lens L_2 (see figure 2.5.1).

A DOE of a certain focal length f_{DOE} will have a certain dispersion (see appendix A.2). Hence, the side-mode suppression ratio can be tailored by changing the DOE focal length f_{DOE} and the lens L_2 focal length f_2 . However, in order to get mode-hop free wavelength tuning, these parameters cannot be arbitrarily chosen. The criteria are outlined in the following section.

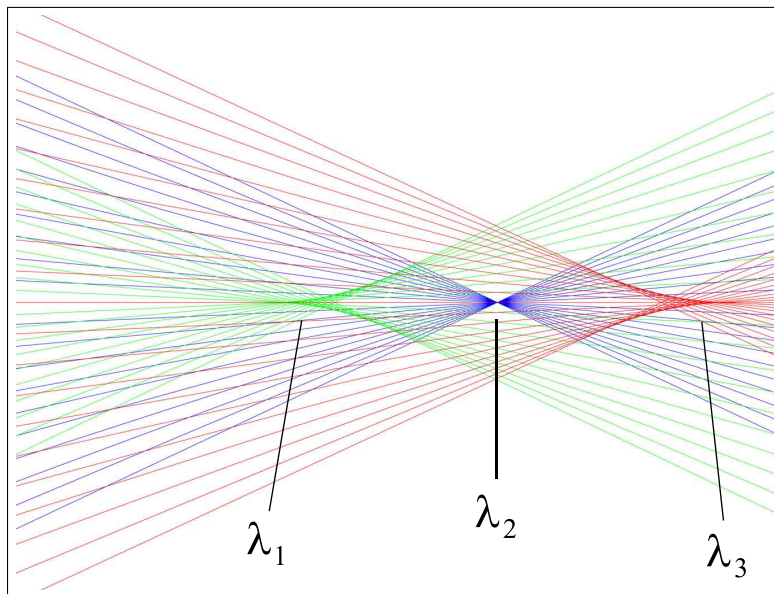


Figure 2.5.4: Three different wavelengths focused at different points on the optical axis. Only one wavelength can be focused on the mirror; all other wavelengths will be defocused and therefore suffer from higher cavity loss. Picture from [34].

2.5.3 Mode-hop free operation

The diffractive optical element (DOE) is essentially a negative lens of focal length f_{DOE} , Fresnelized so that at the design wavelength, ideally all power should be diffracted into the first-order focus (which is virtual for a negative lens, *i. e.*, a divergent order). As the DOE is inserted in the convergent field after the lens L_2 , the focus will become real, but it is moved away from the lens compared to the case without the DOE. The dispersive power of the DOE is given by its focal length f_{DOE} ; the shorter the focal length, the more the different wavelengths are spread out (see appendix A.2).

In order only to get wavelength tuning, the focal length of the DOE is unimportant; the dispersion is enough to get wavelength selection. However, the tuning will in general not be mode-hop free. Mode-hop free operation requires that the number of half wavelengths in the cavity remains constant during tuning.

We have seen that wavelength tuning is performed by moving the external mirror. The DOE dispersion changes the favored lasing wavelength as function of the mirror position. When the mirror is moved, the length of the cavity is changed accordingly. Therefore, if the cavity length can be made to change just the amount required to keep the number of half wavelengths fixed – we have a mode-hop free laser. This is exactly the function of the DOE – it makes the *optical distance* from the SOA to the focus (measured in wavelengths) equal for all wavelengths. This is the reason for choosing a negative DOE; the dispersion must act so that shorter wavelengths are focused closer to the DOE in order to avoid mode-hops.

In figure 2.5.5, a simple sketch of the cavity net gain curve and the modes of the laser is shown. A simple model of the laser cavity of length L gives for mode number q that $L = q\lambda/2$. Hence, for a larger L , λ must increase for a specific mode q .

In order to have mode-hop free operation, the cavity gain must move along with mode q when the cavity length is changed. The focal length of the DOE is shorter for longer wavelengths (see equation (A.2.15) in appendix A.2). This means that longer wavelengths will be focused *further away from the DOE* than shorter wavelengths, if a DOE with *negative* focal length is chosen. Then, the gain is moved towards longer wavelengths at increased cavity length (when the external mirror is moved away from the DOE).

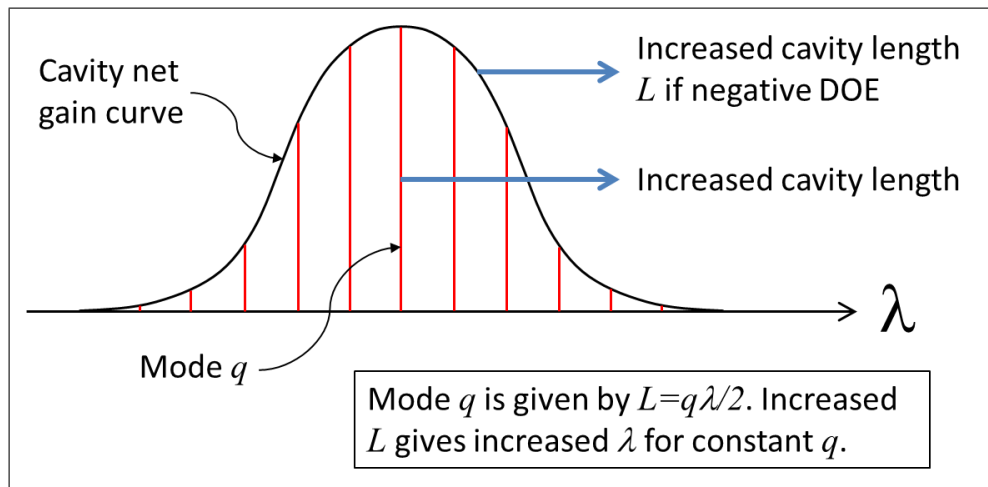


Figure 2.5.5: Schematic sketch of the ECL net gain curve and modes of the cavity. In the simplest model, mode number q in a cavity of length L is given by $L = q\lambda/2$, so that when L is increased, λ must increase as well for a certain mode q . For mode-hop free operation, the net cavity gain peak must be made to move along with mode q when the cavity length is changed.

A specific DOE of focal length f_{DOE} has a fixed dispersion. In combination with the focal length f_2 of lens L_2 , this determines how the focal point moves with the wavelength (as was shown in figure 2.5.4). The change in the cavity length L with λ is slightly different for each cavity mode. Only for one specific mode q , the change in cavity length with wavelength will be exactly the same as the focal point movement caused by the DOE. Then, we have mode-hop free operation.

The cavity length is of course the sum of all *optical* lengths through the cavity. Hence, the focal lengths of the lenses, the DOE, as well as the distances between the lenses and the length of the SOA will have to be tailored so that the total optical length through the system gives the desired mode q .

Chapter 3

Interferometer for beam characterization

The external cavity must be properly designed to compensate for wavefront aberrations associated with the gain chip itself; in particular, the beam may be astigmatic, which is clearly undesirable and must be accounted for [13]. Also, the divergence angles are usually quite different in the two orthogonal directions for edge-emitting laser diodes (or SOAs). It is known that the present gain chip produces a beam of elliptic cross section, and probably a certain amount of longitudinal astigmatism.

Thorough knowledge of the beam emitted from the gain chip is required in order to choose the cavity parameters correctly. To this end, interferometric measurement methods are most suitable, as it is the wavefront information that is of interest here. A multitude of interferometric measurement techniques exist, and different classes of interferometers are useful in very different situations. An appropriate setup must be chosen, so that the beam of interest in our case can be fully characterized.

An interferometer can be designed to handle either a collimated or a divergent/convergent optical field. The beam emitted from the gain chip is strongly divergent. In the current setup, the beam emerging from the external mirror under lasing conditions is also divergent, which suggests that the interferometer should be designed for a divergent beam. On the other hand, the strong divergence makes the beam unmanageably wide after a short distance of propagation. It is much more convenient to have a collimated output beam, whose cross section can be studied at subsequent measurement planes without significant beam spreading.

Furthermore, the CCD array available for sampling is only about 1×1 cm large, and a divergent beam will overfill the CCD. A divergent beam can always be collimated using a well-corrected lens of appropriate focal length. Hence, a collimated light interferometer is the most suitable solution for our ends.

The simple SOA is a fairly wide-band source; the total width of the spontaneous emission spectrum is about 32 nm, with a FWHM spectral width of approximately 10 nm, which corresponds to a coherence length of $\approx 60 \mu\text{m}$. The interferometer must therefore be white-light compensated if the spontaneous emission of the SOA is to be examined.

It is not clear that the output beam under spontaneous emission is representable for the beam under lasing conditions. The ultimate object is therefore to measure the beam parameters on the output beam from the entire external-cavity laser. However, it might be of interest to compare the two cases, and the white-light compensation is then necessary.

In the following, the design and assembly of a lateral shear interferometer is presented. Due to limited time available, no full measurements on the SOA have been carried out in this project. Still, good interferograms from the spontaneously emitting SOA have been captured, thus confirming that the white-light compensation works satisfactory. The functionality of the interferometer is proven in various ways, methods for interferogram interpretation are introduced and a test measurement on a known laser source is described.

3.1 Lateral shearing interferometry

Lateral shearing interferometry has been utilized for many applications and a variety of setups exists. A lateral shear interferometer can be constructed for either collimated or divergent beam measurements, and white light compensation can be readily realized. The technique relies on splitting the beam in two, and then adding the beams slightly displaced in the lateral direction relative to each other. The resulting interference pattern then contains information about the *derivative* of the wavefront in the direction of shear; the wavefront itself can be reconstructed by integration [35]. The first-order curvature of the wavefront can be calculated from the spatial frequency of the interferogram.

Lateral shear interferometers have properties that make them highly suitable for the application at hand. White-light compensation has been mentioned already, and the splitting-and-adding principle makes it possible to arrange a highly stable setup which is very insensitive to vibrations and disturbances in the environment. Also, many shear interferometers can be built with relatively few and simple components.

3.2 Modified Jamin interferometer

A Jamin interferometer can be modified to serve as a device which realizes lateral shear with white-light compensation in the collimated beam case, as shown by Murty [36]. This can be done in several ways, but one of the simplest variants, minimizing the need for movable components and precise control of those components, is shown in figure 3.2.1.

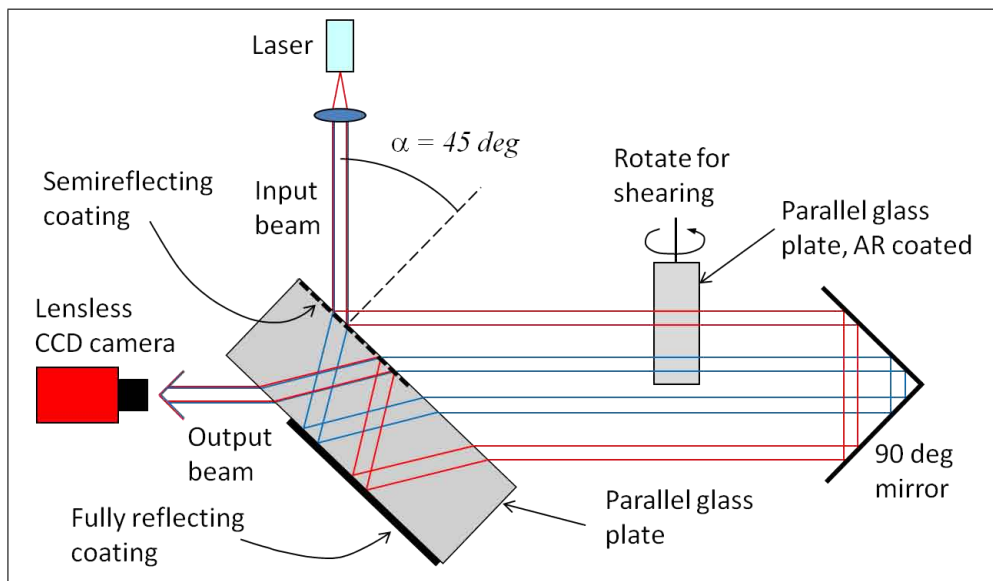


Figure 3.2.1: Modified Jamin interferometer implementing a lateral shear interferometer.

The setup in figure 3.2.1 has one major disadvantage: if a piece of glass without coating is used as beamsplitter and -combiner (relying only on Fresnel reflections), one of the beams undergoes only 1 reflection, whereas the other suffers from 3 subsequent reflections, before they are recombined. This results in poor visibility of the interference fringes. The problem can be solved by introducing a semireflecting coating where the beamsplitting occurs, and perfectly reflective coatings at points where pure reflections occur [35], as shown in the figure. However, this means that a custom-made glass plate must be ordered, at high cost.

Another, much simpler, solution is to utilize the modified Jamin interferometer in a slightly different manner, so that the output beam emerges parallel to the incident beam; thereby 2 Fresnel reflections per beam are necessary. Consequently, the visibility will be strongly improved as the measurement and the reference beam are now carrying almost equal powers, and no coatings are needed for the beamsplitter, so that an off-the-shelf component can be purchased. A sketch of this setup is shown in figure 3.2.2.

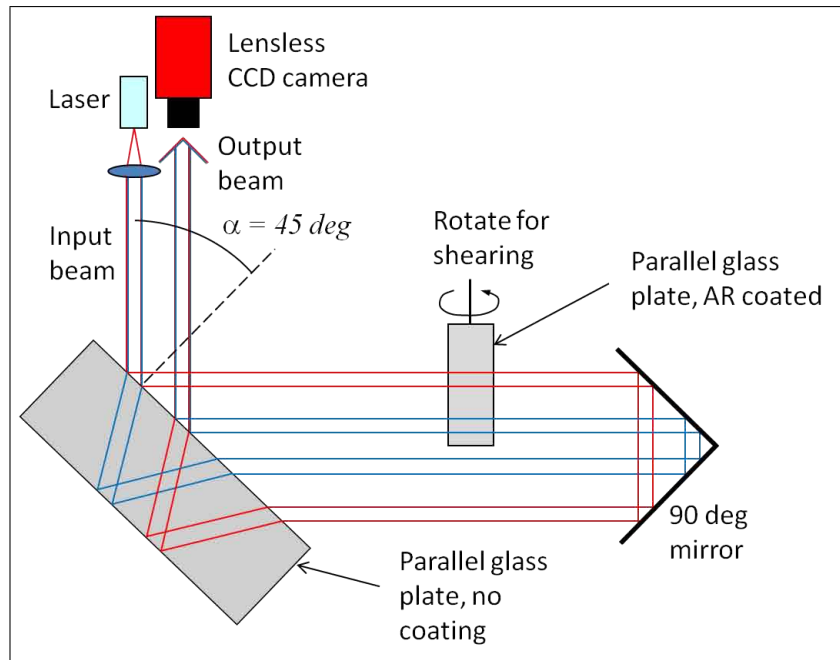


Figure 3.2.2: A simplified variant of the modified Jamin interferometer implementing a lateral shear interferometer. The two beams will undergo an equal number of glass/air boundary reflections and transmissions.

The advantages described above come at the expense of the output beam traveling very close to the input beam. In order to get access to the output field, an extra mirror may have to be inserted to deflect the beam away from the light source, where the camera can be mounted without obscuring the input beam. This is not a serious problem, but adds some extra length to the optical path length of the beam in the interferometer, and an extra optical surface. Another aspect of this is that a deflection mirror must not block the incident beam, and therefore the input and output beams must be sufficiently separated. This separation is governed by the thickness of the beamsplitter and the corner mirror configuration.

White-light compensation in this interferometer is accomplished if the optical path lengths, experienced by the measurement and reference beams, do not differ by more than the temporal coherence length of the light source. In the Jamin interferometer, this condition is automatically fulfilled if ideal components are used, simply because of the geometry of the setup. All distances of propagation in air and glass, respectively, are equal for the two beams. This makes the alignment procedure very easy; as long as the two beams are combined into one at the last surface, white-light compensation is guaranteed.

In a real situation, stringent requirements must be placed on the intrinsic parallelity of the surfaces of both glass plates in figure 3.2.2; typically ≤ 1 minute of arc. The effect of poor parallelity is that the two beams will experience different glass thicknesses, causing a difference in optical path length. In addition to parallelity, all surfaces must also be of high optical quality, typically with surface accuracy $< \lambda/10$, in order not to add wavefront aberrations that will be indistinguishable from the original beam properties.

The modified Jamin interferometer in figure 3.2.2 was built up on a breadboard using a HeNe-laser for alignment purposes. The gain chip with collimation lens was then mounted in place of the HeNe-laser. Photos of the setup with the gain chip in place are shown in figures 3.2.3 and 3.2.4. The chip is mounted on a rotation stage, so that the direction of shear can be chosen arbitrarily. The CCD camera is mounted on a manual translation stage, so that the wavefront can be investigated at different planes.

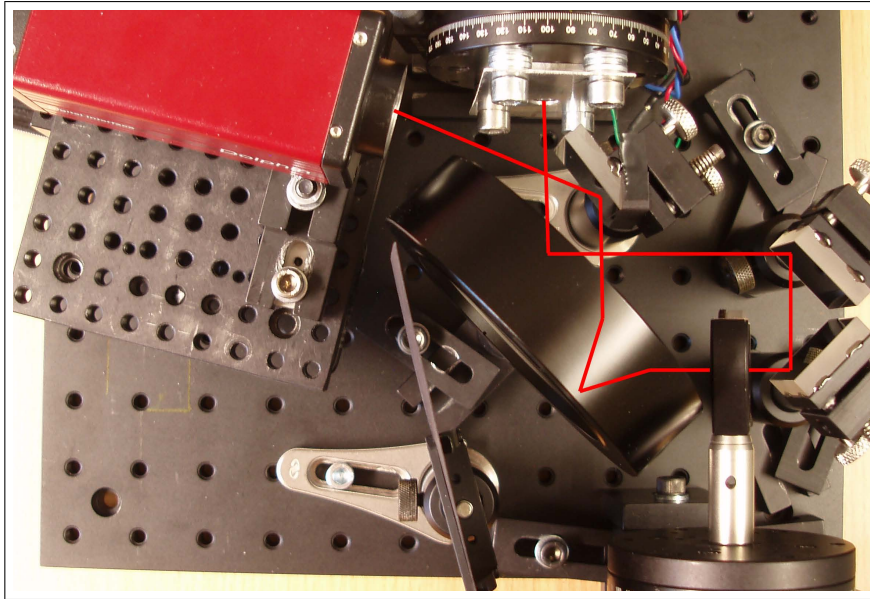


Figure 3.2.3: A photo of the modified Jamin interferometer setup. One of the 2 interfering beams is displayed.

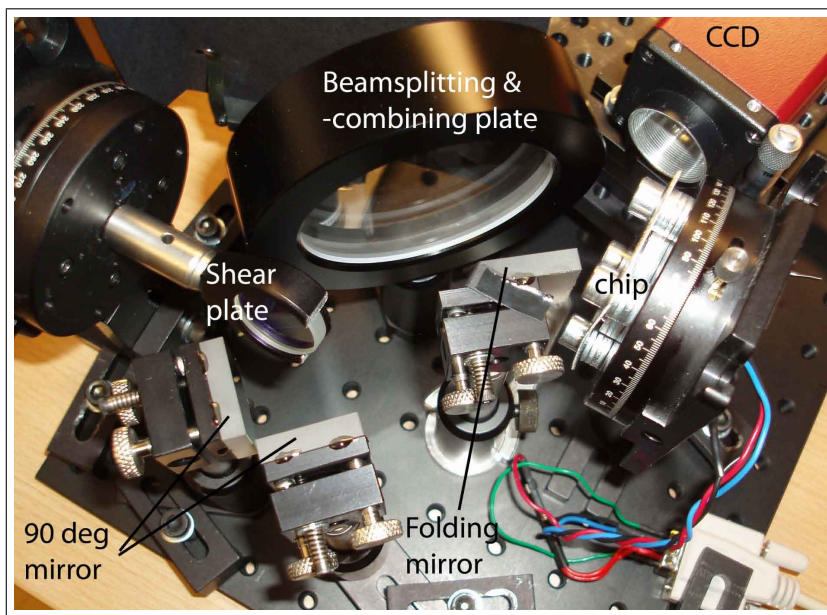


Figure 3.2.4: A photo of the modified Jamin interferometer setup.

3.3 Data evaluation

Interferograms were recorded at a few measurement planes. An example of the raw data is shown in figure 3.3.1. After filtering and normalization, and also subtraction of the DC level, the resulting image is shown in figure 3.3.2.

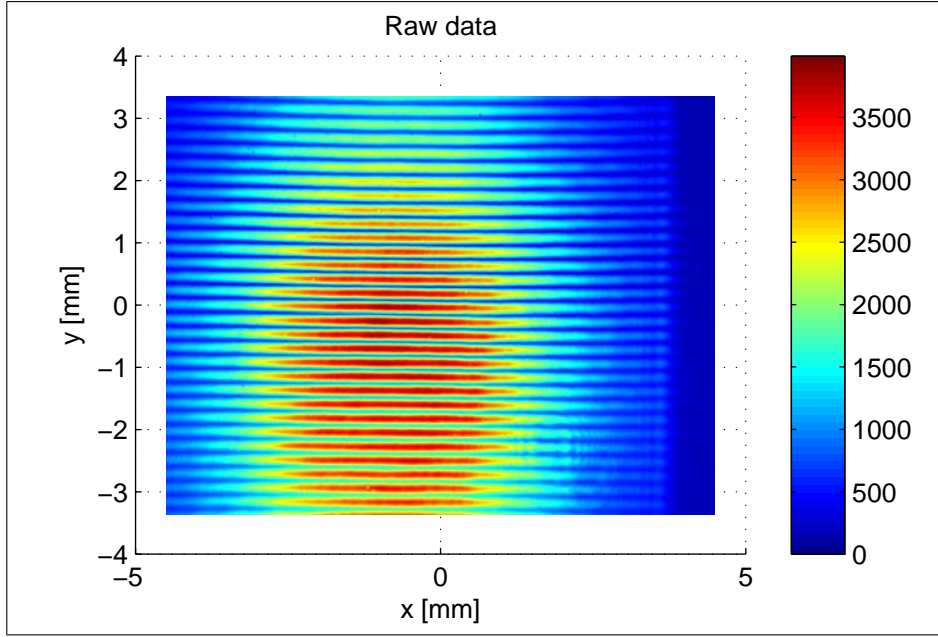


Figure 3.3.1: Example of interferogram captured from the collimated beam from the gain chip, under spontaneous emission. Raw data.

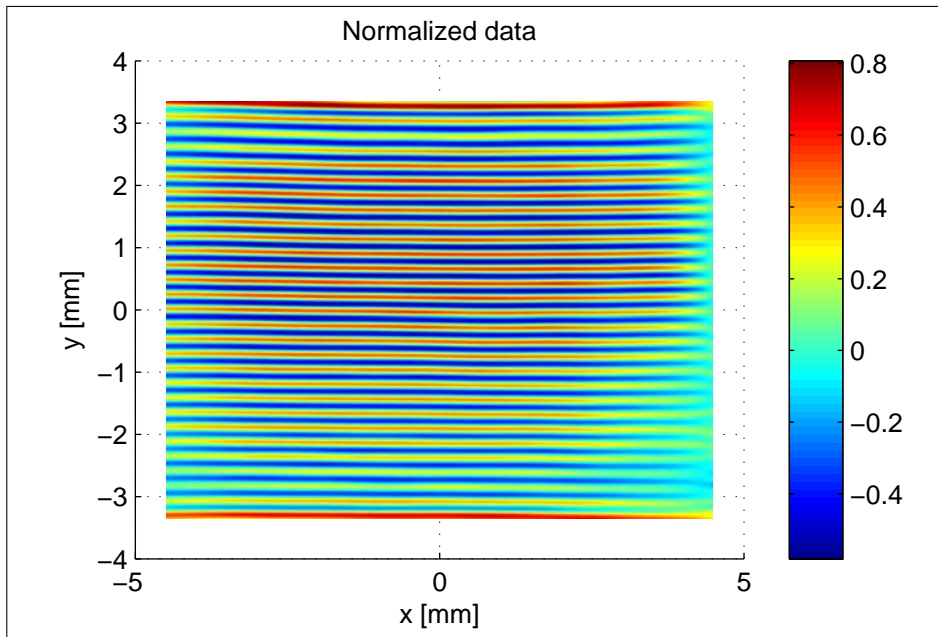


Figure 3.3.2: Example of interferogram captured from the collimated beam from the gain chip, under spontaneous emission. Filtered and normalized data. The DC level has been subtracted.

The fringe visibility V is very good in figure 3.3.1. Using the usual definition,

$$V = \frac{I_{\max} - I_{\min}}{I_{\max} + I_{\min}}, \quad (3.3.1)$$

where I_{\max} and I_{\min} are the maximum and minimum intensity values of the pattern, respectively, the maximum visibility is found to be $V = 72\%$. Thus, the white-light compensation works satisfactory.

3.3.1 Sinusoidal fitting

The fringe pattern in figure 3.3.2 can clearly not be described as an ensemble of equally spaced parallel lines; the lines are somewhat curved due to various wavefront aberrations arising in the optical system or the source itself. Furthermore, the period of the pattern actually becomes larger far away from $y = 0$. This is expected, as the condition of a constant period can only be fulfilled if the lateral shear S is small [35], and $|y| \ll |R|$, where R is the wavefront radius of curvature. The latter requirement will be proven in appendix A.1, where a first order relation between the spatial frequency of the interferogram and the wavefront radius of curvature is derived.

Taking a scan along the y direction at $x = 0$ in figure 3.3.2, only keeping a few periods close to $y = 0$, a very regular sinusoidal intensity distribution is obtained; this is displayed in figure 3.3.3. The important entity to be determined is the spatial angular frequency of this sinusoidal function, as this is related to the radius of curvature of the wavefront, R . Hence, an algorithm for fitting of a sinusoidal function to the intensity distribution was developed.

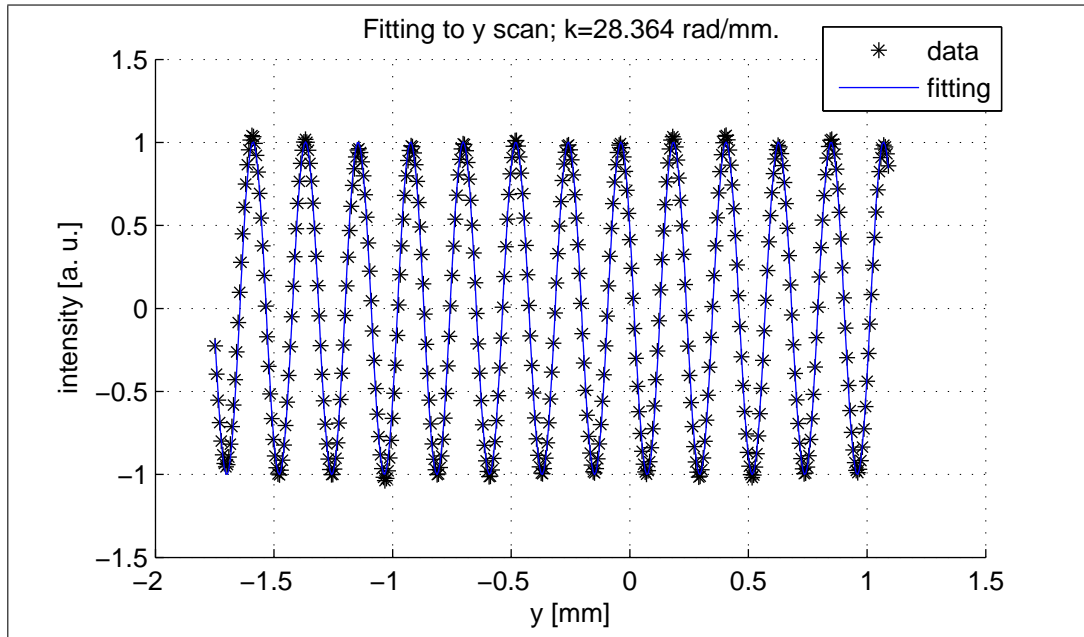


Figure 3.3.3: Scan along y in figure 3.3.2 (stars), and a fitting with the function $I(y) = I_0 \sin(ky + \phi)$ (solid line). The spatial angular frequency is found to be $k = 28.364$ rad/mm in this case.

3.3.2 Gabor transform filtering

The fitting with a sinusoidal function to the measured data works fairly well as long as the interferogram is regular and contains only very little noise at other frequencies. In order to determine the strongest frequency of the interferogram in presence of more noise, a more robust method must be employed. A powerful tool is then the Gabor transform, which can be described as a localized version of Fourier transform, using (most commonly) a Gaussian window that can be moved in time (or, in our case, space) [37]. It can be interpreted as an overlap integral between the measured signal and a complex exponential function of frequency f , localized around $y = y_0$. Its value therefore depends on two variables, f and y_0 . The mathematical definition is [37]:

$$G(f, y_0) = \int_{-\infty}^{\infty} S(y) e^{-\pi(y-y_0)^2} e^{-j2\pi fy} dy, \quad (3.3.2)$$

where $S(y)$ is the measured signal as function of y . By performing this calculation at a sequence of frequencies for each value of y_0 , the result can be visualized in a space-frequency graph. The modulus of the

overlap integral will be large at a point (f, y_0) if a strong modulation of frequency f appears in the neighborhood of y_0 . Hence, the value of a modulation frequency can be determined even in a very noisy signal, by calculating the Gabor transform with high resolution in the frequency domain. As an example, a y -scan from an interferogram is shown in figure 3.3.4, and the corresponding space-frequency graph is displayed in figure 3.3.5 (where the period $1/f$ is used instead of frequency).

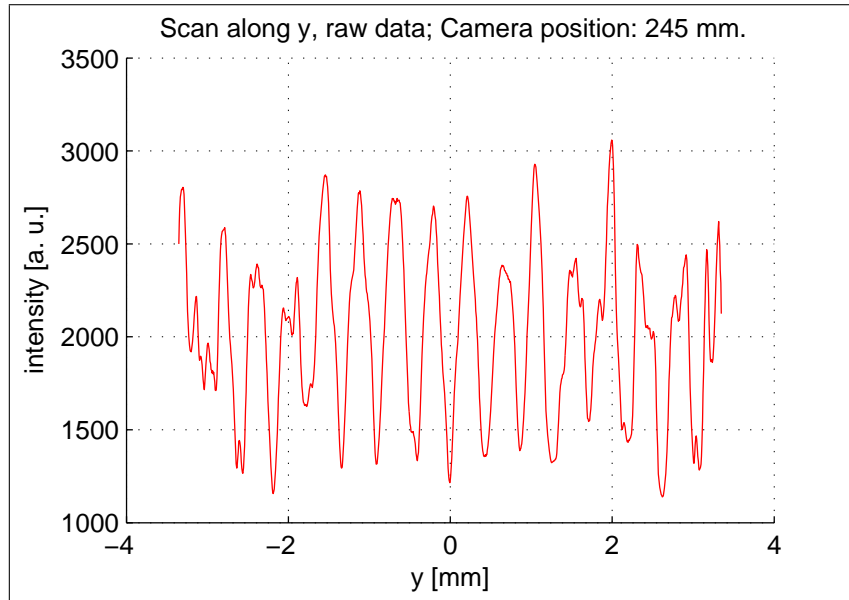


Figure 3.3.4: Example of y -scan from a noisy interferogram captured with the modified Jamin interferometer.

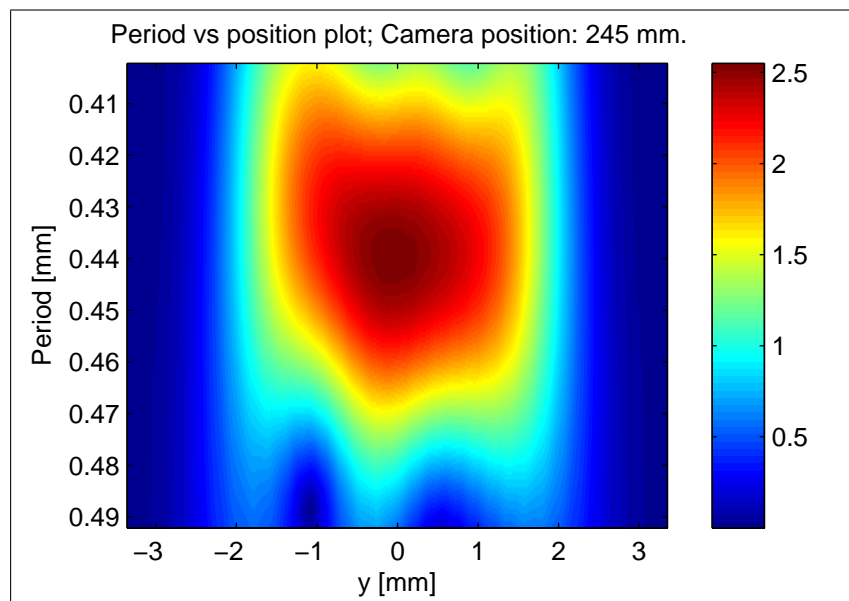


Figure 3.3.5: Space-frequency graph (in fact the spatial period $1/f$ is used instead of frequency) of the Gabor transform filtering applied to the signal in figure 3.3.4. By finding the maximum of this plot, the strongest frequency (period) of the signal can be determined with high resolution.

An additional advantage of the Gabor transform method, is that no a priori knowledge of the data is needed to extract the strongest frequency; when the sinusoidal fitting method is utilized, the parameters of the sine function must be set very close to the correct values in order for the fitting algorithm to converge. Hence, the implementation of the Gabor transform enables automatic interferogram analysis, with subsequent identification of a Gaussian beam if interferograms have been captured at various locations along the beam.

3.4 Test of interferometer functionality

The functionality of the interferometer had to be verified, and two different experiments were therefore conducted. First, the focal length of a known positive lens was measured by quantifying the beam parameters of a laser beam before and after the insertion of the lens, and relating the change in beam parameters to the lens focal length via a Gaussian description of the lens. This investigation is presented in the following section. The experiment also revealed different aspects of the experimental methodology that could be improved.

Using the improved methodology that resulted from the lens measurement, the interferometer was used to measure the beam parameters in the two orthogonal directions of a known edge-emitting laser chip. The measured characteristics were compared to the beam divergences from direct measurements and datasheet, and the astigmatism of the laser was calculated from the experimental data and compared to the specifications from the manufacturer. The results from this experiment are given in section 3.4.2.

3.4.1 Determination of a lens focal length

In order to test the interferometer, a measurement on a HeNe-laser beam was carried out. A positive lens ($f = +100$ mm), mounted immediately after the laser, was used to get a reasonable degree of beam divergence and large enough spot size on the CCD. As the beam emerging from the HeNe-laser is very collimated, this lens produces a focusing of the beam at a distance $\approx f$ from the lens (and this position is located inside the interferometer). The beam is then divergent as it reaches the CCD camera after the interferometer.

Interferograms were captured at a number of cross-sectional planes along the beam, and the wavefront radius of curvature was calculated from the CCD images, using the Gabor transform. Then, an extra lens of focal length $f_l = +250$ mm was inserted about 33 mm after the first lens, which makes the beam waist move slightly towards the laser, and the beam divergence to increase. Interferograms were captured and evaluated once more.

Now, the two different beams are related to each other, as one of them is produced by the first one transmitted through a lens of known focal length. If we can determine the position of this lens in the beam, the focal length of the lens can be calculated from the measured beam parameters. However, the resulting value of f is quite sensitive to the exact position of the lens in the beam, which is difficult to determine (The optical path length from source to CCD through the interferometer must be measured).

Lens transformation

In order to relate the beam parameters of the beam incident on the lens to the beam emerging from the lens, Gaussian lens transformation formulas may be applied. We make use of the following two equations for the scaling of the Rayleigh range z_0 and the change in waist position caused by a thin spherical lens of focal length f [38]:

$$z_{0t} = M^2 z_{0i}, \quad (3.4.1)$$

$$(z_t - f) = M^2 (z_i - f). \quad (3.4.2)$$

Here, z_{0i} and z_{0t} are the Rayleigh ranges of the incident and transmitted beam, respectively, and z_i and z_t are the distances from the waist positions to lens, defined analogously. The factor M^2 is given by:

$$M^2 = \frac{f^2}{(z - f)^2 + z_0^2} \quad (3.4.3)$$

where z is the distance from the waist positions to lens and z_0 is the Rayleigh range. Equation (3.4.3) is defined for the incident beam, but can equally well be used for the transmitted beam, if one wants to make backward calculations. Then, the indices i and t must be swapped in equations (3.4.1) and (3.4.2). This method is the one used here, so that the "transmitted beam" is viewed as the primary one.

Beam identification

We now turn the attention to the identification of beam parameters from measurements. The wavefront radius $R(z)$ of curvature of a Gaussian beam is given by [38]:

$$R(z) = z \left[1 + \left(\frac{z_0}{z} \right)^2 \right], \quad (3.4.4)$$

where z is the distance from the beam waist, and z_0 is the Rayleigh range. Using this model and adjusting the parameter z_0 and the location of the beam waist for best fitting, in least-square sense, to the measured data, the location of the beam waist can be robustly determined.

In figure 3.4.1, measurement data and the corresponding fittings of equation (3.4.4), are shown. It can be seen that the beam waist is moved about 9 mm towards the laser when the extra lens is inserted.

The waist of the beam in absence of the extra lens is found 100 mm from the laser lens, but this is from assumption; the optical path length through the interferometer has been adjusted to get this value. This is of course not a precise method, and it is therefore advisable to determine the distance from the source by other means, and use this as reference. For instance, the position of the waist may be estimated by inserting a small sheet of paper into the beam and locating the point where the beam size is minimum.

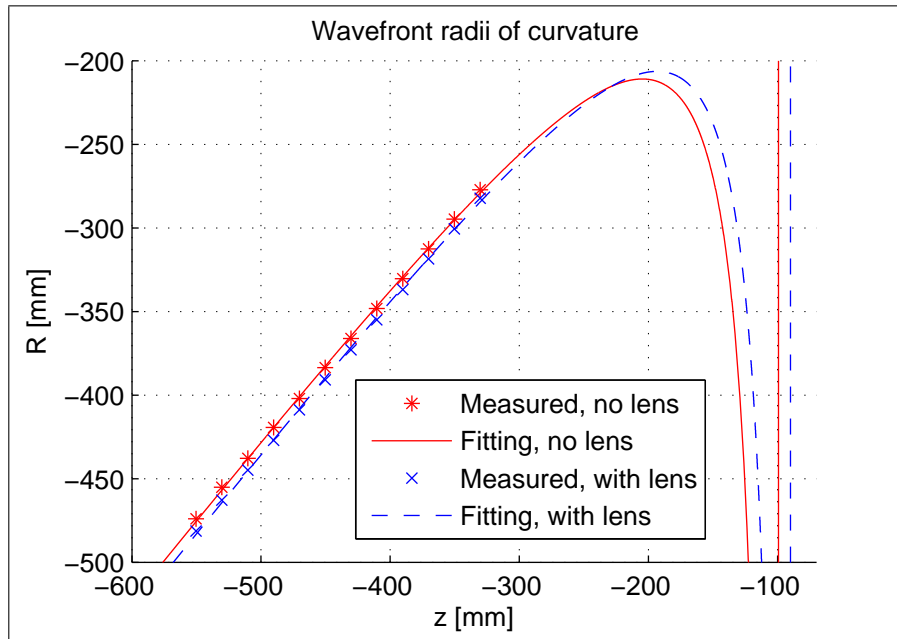


Figure 3.4.1: Wavefront radii of curvature, measured with HeNe-laser with and without an $f = +250$ mm lens, and corresponding fitting of equation (3.4.4). The waist (located where $|R| = \infty$) moves about 9 mm towards the source when the lens is inserted. The laser is positioned at $z = 0$, and z becomes more negative as we move away from the laser.

Equation (3.4.4) reveals that $R(z) \approx z$ when $z \gg z_0$, so that the information on z_0 is lost. This method is therefore not good for estimating the value of z_0 . In fact, the fitting gives almost identical values for z_0 with and without the extra lens, respectively, which does clearly not agree with the observed increase in beam divergence. Quantifying the beam divergence is a better method for determining the value of z_0 . This can be done by sampling the beam intensity in subsequent planes along the beam, and fitting a Gaussian function to the data. The width $W(z)$ of the beam at distance z from the waist is given by [38]:

$$W(z) = W_0 \sqrt{1 + \left(\frac{z}{z_0} \right)^2}, \quad (3.4.5)$$

where W_0 is the intensity $1/e^2$ half width at the beam waist. If we are far away from the beam waist, $z \gg z_0$, so that $W(z) \approx W_0 z/z_0$, which can be manipulated to the expression:

$$W(z) \approx z \cdot \sqrt{\frac{\lambda}{\pi z_0}} ; \quad z \gg z_0, \quad (3.4.6)$$

which is a linear function of z with a slope directly related to z_0 . The interferometer was used to capture pure intensity images of the beam, by turning the lateral shear to zero. The $1/e^2$ intensity radius of the beam was determined at successive planes, and equation (3.4.6) was used to extract a value of z_0 . In figure 3.4.2, a graph of the beam width versus CCD camera position is shown, with and without the $f = +250$ mm lens, respectively. The fitting gives the value $z_0 = 12.6$ mm without the lens, and $z_0 = 8.1$ mm with the lens in place, a difference of 36%.

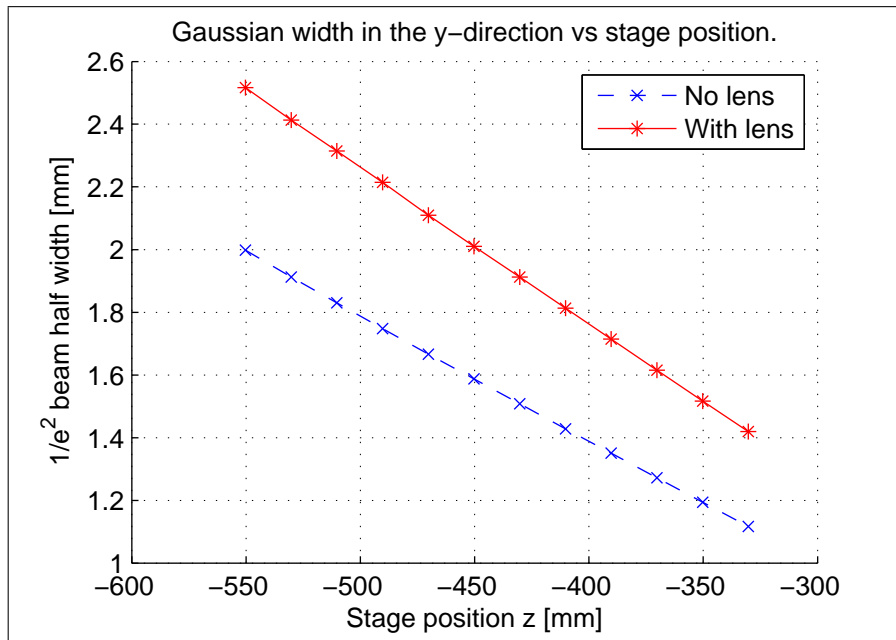


Figure 3.4.2: $1/e^2$ beam half width, measured with HeNe-laser with and without an $f = +250$ mm lens, and corresponding fitting of equation (3.4.6). The beam becomes more divergent as the lens is inserted, as anticipated. The laser is positioned at $z = 0$, and z becomes more negative as we move away from the laser.

The focal length can be calculated either from the change in waist position (equation (3.4.2)), or from the change in z_0 (equation (3.4.1)). Adjusting the lens position used for the calculations until the values of f found by both methods are consistent, the result is $f \approx 197$ mm, which differs by 21% from the nominal value.

Discussion

Of course, the focal length of a lens can be measured much more correctly by other means than the interferometric method outlined above, but the point here is that the interferometer can robustly identify a certain beam (its waist position and Rayleigh range). A number of methodological problems were identified, and are discussed in the following paragraphs. These shortcomings may explain the error of 21% in the lens focal length found through the measurement.

One problem was that the measurements on the beam intensity profile were made by turning the shear plate back to zero tilt (no shear). At zero shear, the two splitted beams will ideally be perfect replicas of each other and are superimposed at full constructive interference. This assumption can of course be questioned; interference between the beams may cause slight redistribution of optical power, which affects the beam

width. Another problem is the fact that the beam hitting the CCD is strictly speaking not the same with and without shear (the beam parameters are slightly dependent on the shear angle). This effect might be contributing to the discrepancy between the nominal and measured focal length of the lens.

The most robust way to capture intensity images is to block one of the two interfering beams, hence getting rid of the interference pattern, but letting the shear angle remain unchanged between the interferometric and intensity profile measurements. This method will be used henceforth.

Another problem related to the lateral shear was identified as well; in the measurement presented up to this point, the lateral shear (in mm) was calculated from the shear angle of the shear plate. The shear angle was read from a scale, and a simple ray model was used to calculate the resulting linear shear.

A more robust way to determine the shear is to block each of the beams in turn, and finding the centroid of the CCD image. The distance between the centroids is the lateral shear. It turned out that the shear calculated this way was slightly different than the shear calculated from the shear angle. In the following measurement, outlined in the next section, the shear has been determined from this type of intensity measurements.

The output beam from the laser used as light source in this experiment is elliptical. This makes the foci somewhat less distinct. Probably, the foci positions can be more easily determined if a beam of circular cross section is used.

A final remark regards the lens transformation formulas (3.4.1) and (3.4.2); the model used assumes that a Gaussian beam is transmitted through a *thin* spherical lens, which will produce a new beam, still being Gaussian. In this case, the collimating lens can hardly be considered to be thin (its thickness is on the same order of magnitude as its diameter), but on the other hand, it is parabolically shaped, hence reducing spherical aberrations, so that the beam can probably still be assumed to be Gaussian. The thickness may, however, still cause small errors in the calculated beam parameters.

Using the formulas for transformation of a Gaussian beam through a thin lens, the parameters of the beam incident on the external mirror can be calculated. Of course, this is also somewhat sensitive to the exact position of the lens in the beam (which is difficult to determine). On the other hand, as we are primarily interested in the *difference* between the two orthogonal directions of the beam, the same value for the lens position can be used in both calculations. The calculated relative difference between the beam parameters in the x - and y -directions is much less sensitive to the exact position of the lens.

In order to test the assumption that the *difference* between x - and y -directions can be properly determined, a reference measurement on a Thorlabs laser ($\lambda = 785$ nm) with known astigmatism and angles of divergence was made; this is presented in the following section. Then, the improved methods for beam width and lateral shear quantification mentioned above are also applied.

3.4.2 Reference measurement on a known laser

A laser from Thorlabs, HL7851G, was mounted with a collimating lens, $f = +4.5$ mm. The beam was then launched into the interferometer, and interferograms were captured for the two orthogonal directions of the beam. Blocking one of the interfering beams, the intensity profile of the beam was measured as well. The wavefront radius of curvature graph is shown in figure 3.4.3, and the beam width graph is found in figure 3.4.4. From these data, the Rayleigh range z_0 was determined from the intensity measurements, and the waist position (measured from the CCD) was calculated from the interferograms. The waist position in the x - and y -directions was found to differ by 5.0 mm.

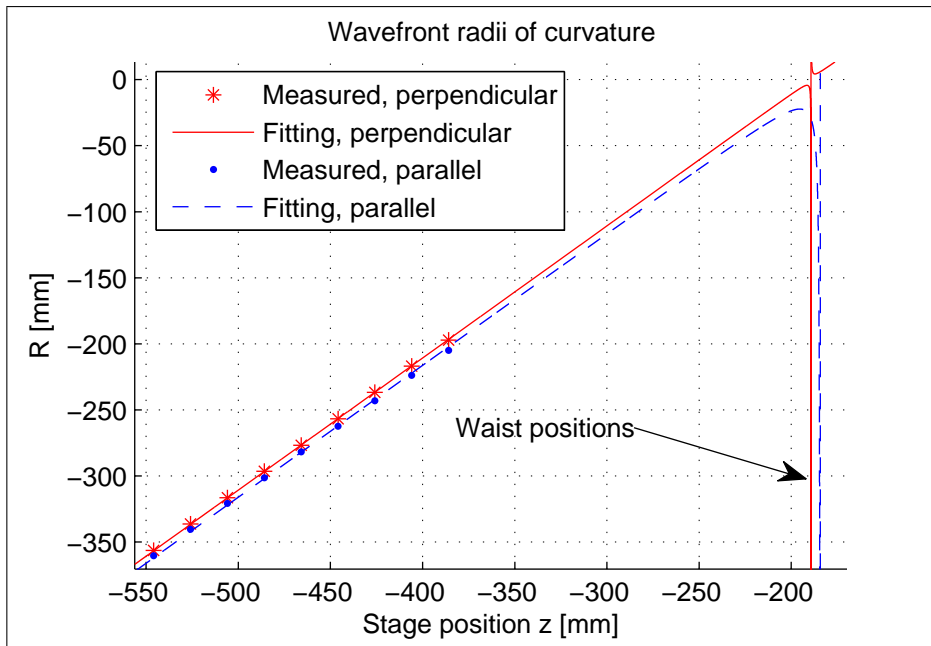


Figure 3.4.3: Wavefront radii of curvature, measured for the HL7851G laser, in the direction parallel and perpendicular to the epitaxy, respectively. The corresponding fitting of equation (3.4.4) is given as well. The waist position (located where $|R| = \infty$) differs by 5 mm between the two orthogonal directions. The laser is positioned at $z = 0$, and z becomes more negative as we move away from the laser.

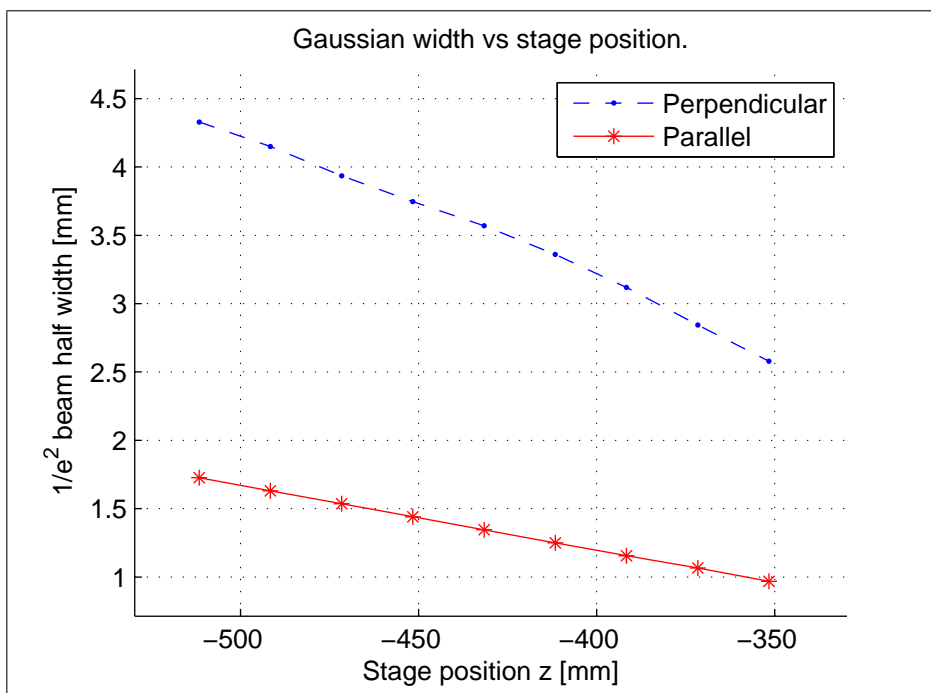


Figure 3.4.4: $1/e^2$ beam half width, measured for the HL7851G laser, and corresponding fitting of equation (3.4.6). The beam width is measured in the direction parallel and perpendicular to the epitaxy, respectively. The laser is positioned at $z = 0$, and z becomes more negative as we move away from the laser.

As pointed out earlier, it is important to know, at least roughly, the distance from the lens to the beam waist. Therefore, an extra measurement was carried out, with the collimated beam launched directly onto the CCD (without the interferometer). Measuring the intensity profile and calculating the beam width as function of distance from the lens, the waist position could be calculated by extrapolating the linear beam width function until it goes to zero. The beam waist was then found to lie about 190 mm from the lens. The optical path length through the interferometer (measured to be approximately 682 mm), was then calibrated (a small change by 36 mm) so that the beam waist position agrees with the result from the width measurement.

Now, using the lens transformation formulas (3.4.1) and (3.4.2), the beam parameters of the naked laser diode can be calculated. The results are presented in table 3.1, together with values given in the laser datasheet. In order to check the actual beam divergence of this diode, the beam intensity profile of the naked laser chip was measured with the CCD camera. These values are also given in table 3.1.

Table 3.1: Parameters of the laser HL7851G. Results from interferometric and intensity measurements on the collimated beam ("Interferometer"), compared to values given in datasheet ("Specified"). Also, beam divergence of the laser from a direct measurement is given ("Direct measurement"). All angles are for $1/e^2$ intensity half-widths. The datasheet values are given for an output power of 50 mW in the case of beam divergence, and 5 mW for the astigmatism. The measurements were conducted at an output power of ≈ 3 mW.

	Divergence, parallel			Divergence, perpendicular			Astigmatism
	<i>min</i>	<i>nominal</i>	<i>max</i>	<i>min</i>	<i>nominal</i>	<i>max</i>	<i>nominal</i>
Specified	6.8°	8.1°	10.2°	15.3°	19.5°	23.8°	5 μm
Interferometer	—	10.9°	—	—	25.4°	—	2.6 μm
Direct measurement	—	11.2°	—	—	27.4°	—	—

The calculated astigmatism indicates that the beam waist associated with the parallel direction is located 2.6 μm further *inside* the laser chip, compared to the perpendicular direction. This is the usual situation for ridge waveguide lasers [13]. It should be pointed out that the datasheet values of beam divergence are given for an output power of 50 mW, and the astigmatism for 5 mW. In the present measurements, the output power was only about 3 mW.

The calculated beam divergences agree very well with the values observed from the raw measurement on the naked chip. However, these divergence values are larger than the extreme values given in the datasheet. This may be due to the low output power used in our measurements; the divergence angles specified in the datasheet are given at an output power of 50 mW as mentioned above. It is likely that the divergence varies with the output power (for instance, the temperature and the charge carrier density change with output power, which may affect the divergence). Hence, it is not surprising that the measured divergence is slightly outside the specification.

The astigmatism follows the same principle; at higher output power, the smaller beam divergence will act to increase the astigmatism (the waists in the two orthogonal directions are drawn apart). The observed astigmatism of 2.6 μm is lower than the specified 5 μm , but is also measured at a lower output power. Hence, the measured beam parameters can be considered to be in agreement with the datasheet values.

To conclude this investigation, the functionality of the interferometer has been proven, and it can be used to reliably measure beam divergence and astigmatism of a laser diode — or an external-cavity laser. The white-light compensation makes it possible to study the naked semiconductor optical amplifier, without feedback. This experiment has not been conducted due to time limitations.

The interferometer can also be used to examine the operational ECL. The SOA without optical feedback will produce a superposition of all modes and wavelengths, and the "average phase front" may not at all be representable for the situation under lasing conditions. The interferometer should therefore, primarily, be used to study the beam produced by the functional external-cavity laser.

3.4.3 Discussion and summary

The interferometer has been tested and its functionality has been verified. The measurement on the known Thorlabs laser indicates that the beam parameters can be determined with high precision. The Gabor transform has been used to extract the spatial frequencies of the captured interferograms, and the wavefront radius of curvature can be calculated from this information. Direct intensity measurements give the beam divergence. Applying the Gaussian beam model, the conditions inside the light source or the focal length of a lens inserted in the beam can be determined.

It was observed that a lens focal length was underestimated by 21% from an experiment. However, quite uncertain ways of measuring the lateral shear and the beam divergence, respectively, were used in this measurement, and more robust methods were identified afterwards. Hence, it can be anticipated that the inaccurate methods were responsible for much of the observed error.

The interferometer can be used to measure the output beam parameters of the ECL, and the astigmatism of the gain chip may then be calculated by making use of the lens transformation formulas. The white-light compensation of the interferometer works properly, so that the spontaneous emission from the SOA may also be studied.

The method for determining the beam parameters could perhaps be made more robust by making the lens transformation calculations in the reverse direction. First, one would assume the beam divergence, in the two orthogonal directions, for the laser (or SOA) under test. The divergence angles are usually stated in datasheets or are easily measurable. Then, one proceeds calculate the parameters of the (almost) collimated beam that is formed by the lens, using equations (3.4.1) and (3.4.2). In the calculations, one would finally adjust the assumed divergence angles and the distance between the laser and the lens until the resulting beam agrees as well as possible with measured data.

The lateral shear interferometer has certain drawbacks, the most important one being, perhaps, the fact that it gives beam information only in one transverse direction. In order to compare the x - and y -directions, the laser itself must be rotated 90 degrees about the optical axis. This may be difficult, at least in a laboratory setup.

Other interferometric methods, that can be used to study both orthogonal directions simultaneously, may be considered. Some kind of longitudinal, instead of lateral, "shearing" could be possible, similar to a Michelson interferometer. The white-light compensation might then be difficult to achieve, but is perhaps not necessary if only the laser beam is being examined.

Chapter 4

Characterization of spectrometer and external mirror

In this chapter, the characterization of the spectrometer used for spectral measurements on the ECL is described, including the single-mode fiber used to collect light into the spectrometer. The results are found in section 4.1. Also, the external mirror has been investigated with respect to its spectral properties; this is presented in section 4.2.

4.1 Spectral characterization of fiber and spectrometer

A single-mode fiber (SMF) designed for the wavelength region 630-860 nm was used to couple light from the laser beam to the spectrometer. In order to avoid back reflections from the fiber end surfaces, which could disturb the laser, an FC/APC contact (the ferrule is polished at an angle of 8 degrees) is used at the end coupled to the laser.

The spectrometer interface, however, is an SMA contact, and such fiber contacts are not available with the angled facet version. Hence, the fiber was ordered with a standard SMA contact at the spectrometer end, and then sent to Micropol Fiberoptic AB for custom polishing of the ferrule at approximately 8 degrees. As the spectrometer images the fiber facet onto a CCD array, it works fine despite the fact that the angular distribution of light coupled out from the SMA end is changed due to the polishing. The position of the fiber facet is also changed as a small amount of the ferrule is removed in the polishing, but this only causes a slight defocus, and the spectral resolution is still limited by the CCD in the spectrometer.

In order to get the relative intensity of the laser output spectrum correct, the spectral sensitivity of the spectrometer itself plus the SMF must be measured. By using a black-body source of known color temperature as a spectral reference, the response of the spectrometer system can be determined. If the relative sensitivity of the spectrometer plus fiber is denoted $S(\lambda)$, and the captured spectrum is called $I(\lambda)$, the sensitivity of the measurement system can be calculated from

$$S(\lambda) = \frac{I(\lambda)}{H(\lambda, T)}, \quad (4.1.1)$$

where $H(\lambda, T)$ is the Planck black-body radiation spectrum at temperature T ,

$$H(\lambda, T) = \frac{8\pi hc}{\lambda^5} \frac{1}{\exp\left\{\frac{hc}{\lambda kT}\right\} - 1}. \quad (4.1.2)$$

As reference source, the HL2000-LL halogen lamp from Ocean Optics was used, with a specified color temperature of $T = 2800$ K. The measured spectrum $I(\lambda)$ with the SMF plus spectrometer is displayed in figure 4.1.1.

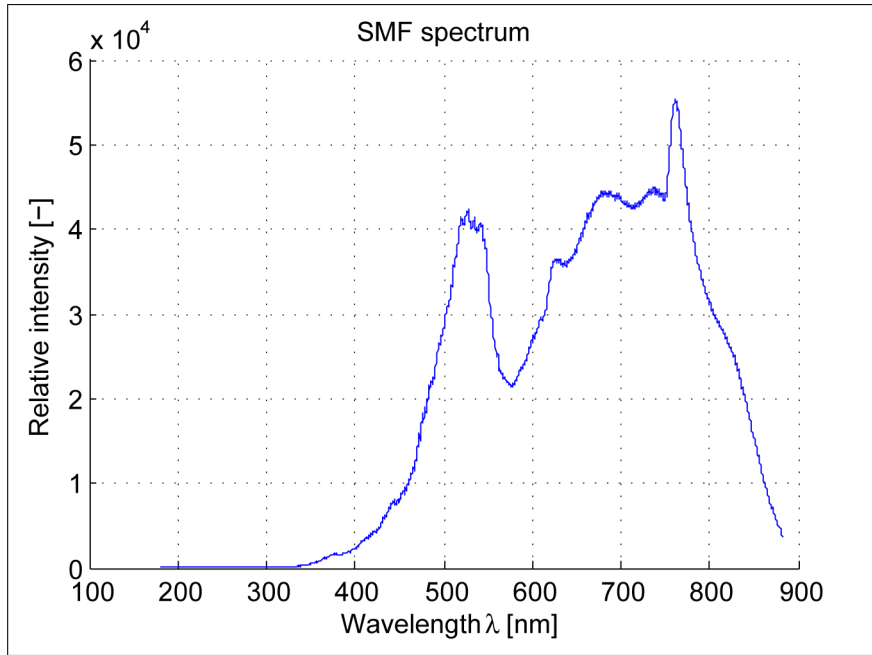


Figure 4.1.1: Raw data $I(\lambda)$ captured with the spectrometer plus the polished SMF, with the halogen lamp HL2000-LL as reference source, $T = 2800$ K.

The sensitivity spectrum $S(\lambda)$ is given by equations (4.1.1) and (4.1.2), and is shown in figure 4.1.2.

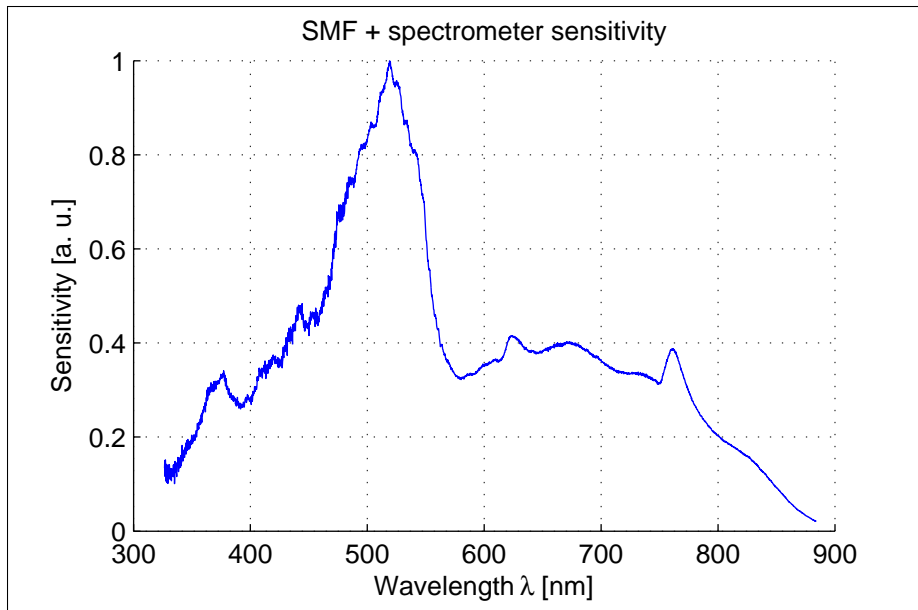


Figure 4.1.2: Sensitivity $S(\lambda)$ of the spectrometer plus the polished SMF.

In order to make sure that the SMF works properly, its transmittance spectrum can be found by measuring the spectral response of the interferometer with and without the SMF in place, respectively, and taking the ratio between the two measurements. A multi-mode fiber with core diameter $200 \mu\text{m}$ was used to couple light from the source to the SMF and to the spectrometer, respectively. The resulting transmission spectrum of the SMF is shown in figure 4.1.3.

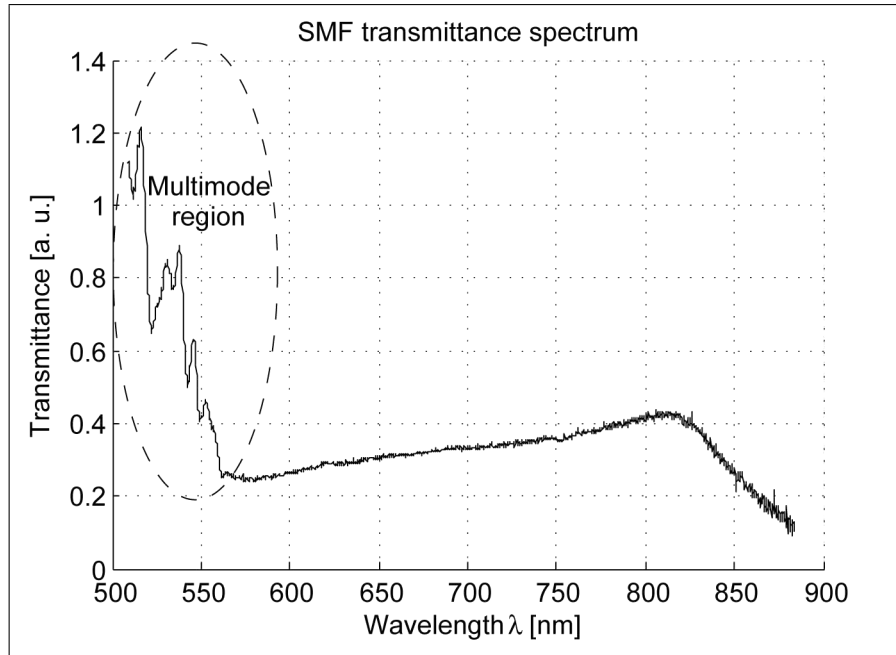


Figure 4.1.3: Transmittance of the polished SMF. The onset of the second mode can be seen at $\lambda \approx 570$ nm.

The multi-mode region can be observed to begin at $\lambda \approx 570$ nm. This is within the range specified by the manufacturer, which is 590 ± 30 nm. The transmittance is a smooth function of wavelength over the region of interest for the ECL, 750-800 nm. It can be concluded that the SMF still works as intended after the polishing operation. The sensitivity spectrum of figure 4.1.2 is implemented in the Labview controller software and is used to re-scale the data captured from the spectrometer.

4.2 External mirror characterization

The external mirror 05B200C.20 from Newport, used in the setup is a multi-layer dielectric mirror. For proper operation of the laser, the mirror reflectivity should be constant over the spectral range of interest, as the spectral properties of the laser radiation should be governed by the cavity, not the outcoupling mirror. It is thus crucial that the mirror be spectrally investigated, in order to secure that it is correctly designed.

Using a fiber-coupled imaging spectrometer (Ocean Optics USB4000) and a multimode fiber as light collector, the dielectric mirror transmittance $T(\lambda)$ was measured using a broad halogen DC source as reference. The corresponding spectral reflectance $R(\lambda)$, calculated as $R(\lambda) = 1 - T(\lambda)$ (assuming negligible mirror absorption), is displayed in figure 4.2.1.

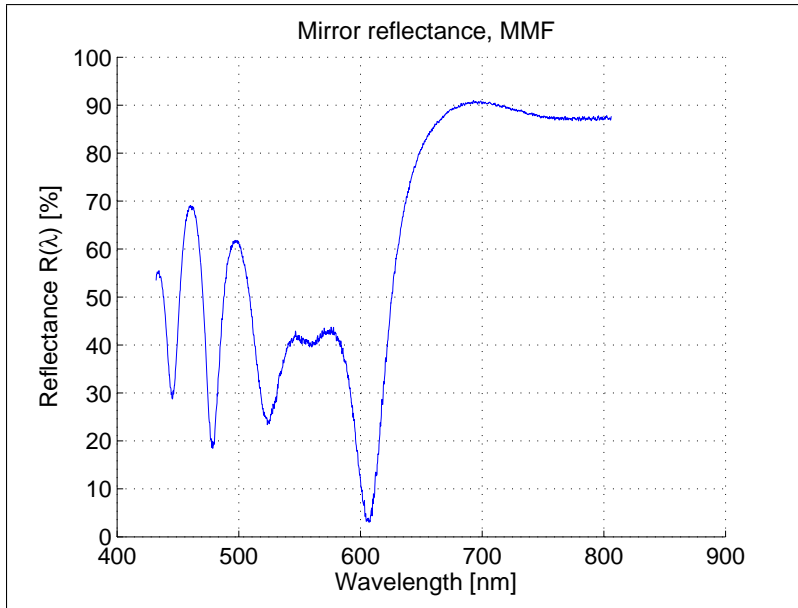


Figure 4.2.1: The spectral reflectance of the external mirror 05B20OC.20 from Newport, calculated from the transmittance spectrum captured by the Ocean Optics USB4000 spectrometer. As can be seen, the reflectance is fairly constant between 750 and 800 nm.

The reflectance is observed to be almost constant in the wavelength range $750 < \lambda < 800$ nm, as desired, and it is found to be approximately 87% in the same spectral region. The result well resembles the typical reference reflectance curve given by the manufacturer, shown in figure 4.2.2, but appears to be slightly shifted in wavelength. The mirror can therefore be assumed to work as intended, with virtually zero dispersion and quite high reflectivity in the wavelength region of interest.

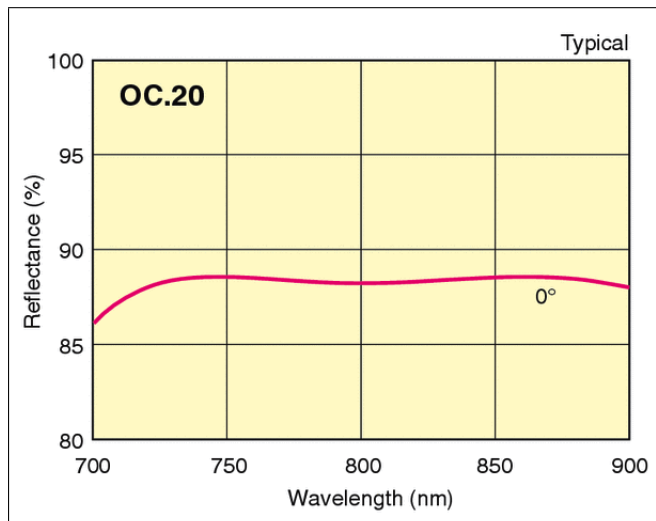


Figure 4.2.2: The spectral reflectance of the external mirror 05B20OC.20 at normal incidence; reference from Newport [39]. The reflectance is approximately constant at 88% in the wavelength region 750-800 nm.

It should be pointed out that 87% is rather a low reflectance. The lasing threshold could probably be lowered by using a mirror with a slightly higher coefficient of reflection. Of course, the output power will be affected as well when the mirror reflectance is changed, so the choice is not trivial, but it is certainly worth to investigate if the laser performance can be improved in this manner.

Chapter 5

Characterization of DOE

Four diffractive optical elements (DOEs) with different effective focal lengths, and consequently different dispersion characteristics, were fabricated in the Chalmers MC2 clean room facility in 2006. The DOE topography (groove quality, periodicity etc.) was evaluated in an atomic force microscope (AFM), and microscope images were taken [40]. Although the DOE of lowest dispersive power (named C1) was used in the operational laser tests performed in 2007, no full characterization of the DOE functionality was carried out at the time.

Two aspects of the DOEs are of main importance; their effective focal lengths and their efficiency, *i. e.*, the relative power focused in the first diffraction order, compared to all incident power. The efficiency is 100% for an ideal DOE, but is decreased due to imperfections in the manufacturing process. In section 5.1, a measurement method for determination of the DOE focal lengths is presented, along with a paraxial model of the DOE (see appendix A.2). In section 5.2, a direct measurement technique to find the DOE efficiency is given, and finally, section 5.3 explains a more robust experimental method to determine the efficiency from self-interferometric measurements on the DOE.

5.1 DOE effective focal length

The DOEs are designed to work in a convergent light field, as the DOE is positioned immediately after the second lens L_2 in the cavity, which is used to focus the field to a focus on the external mirror. The easiest method to achieve an accurate characterization is therefore to utilize the entire setup, except for the external mirror. The SOA was replaced by a 785 nm Thorlabs laser, in order to minimize the dispersive effects of the DOEs; then distinct foci will be formed, and the distance of each focus from the DOE can be measured.

5.1.1 Measurement setup and theory

A sketch of the measurement setup utilized to study the focusing properties of the DOEs is shown in figure 5.1.1. A positive lens is used to image each focus on a CCD array positioned far away from the lens. Using a micrometer slide to move the lens away from the DOE, and observing the formation of a focus on the CCD, the distance between successive foci could be measured. The absolute distance of the foci from the DOE surface could also be determined by imaging the DOE surface itself on the CCD, and using the corresponding lens position as the origin of the measurement.

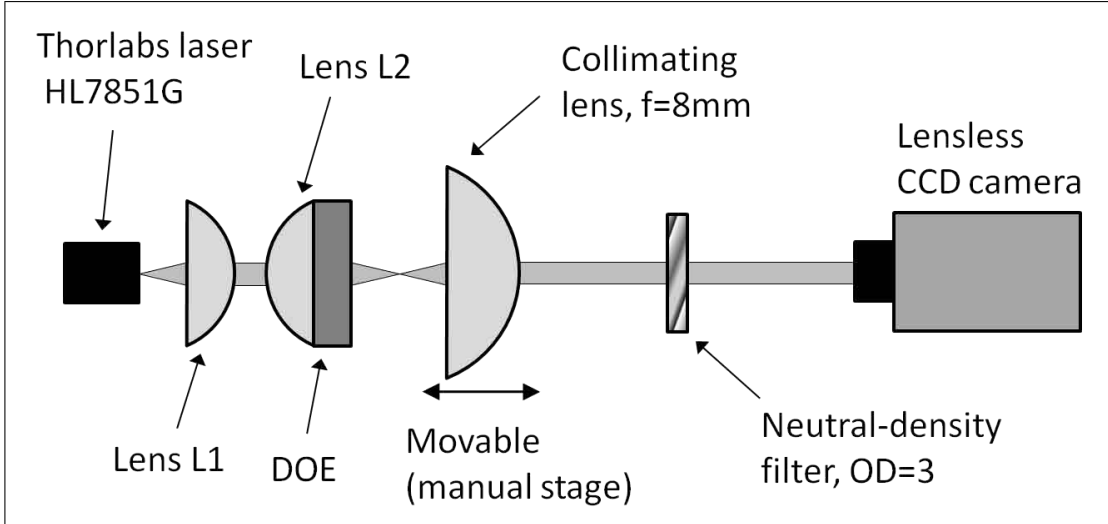


Figure 5.1.1: A sketch of the setup for measuring the location of the DOE focal points. The collimating lens is used to image the foci onto the CCD (positioned quite far away; the picture is not to scale). By moving the lens, subsequent foci can be imaged onto the CCD, and their distances from the DOE plane can be determined.

In order to calculate the effective focal length of the DOE, a simple paraxial model for the system containing the second cavity lens L_2 and the DOE was derived. The derivation can be found in appendix A.2, and the final result, giving the distance L_N from the DOE surface to the N :th diffraction order focus, is given here:

$$\frac{1}{L_N} = \left(w - \frac{b}{n_D} \right)^{-1} + \frac{N}{f_{DOE}}; \quad N \in \mathbb{Z}; \quad f_{DOE} < 0. \quad (5.1.1)$$

In equation (5.1.1), w is the working distance of the cavity lens, b is the DOE substrate thickness, n_D is the DOE refractive index, and f_{DOE} is the effective focal length of the DOE. Hence, $1/L_N$ is a linear function of N , with slope $1/f_{DOE}$. The design focus of the DOE (hereafter called the principal focus) is order $N = 1$.

5.1.2 Measurement results

The location of four to seven different foci were measured for each DOE, by the method described in the previous paragraph. As an example, a graph displaying the inverse distances from the DOE to foci as function of the number of the diffraction order for the DOE of longest focal length (C1), is shown in figure 5.1.2. The corresponding graphs for the remaining three DOE:s look very similar.

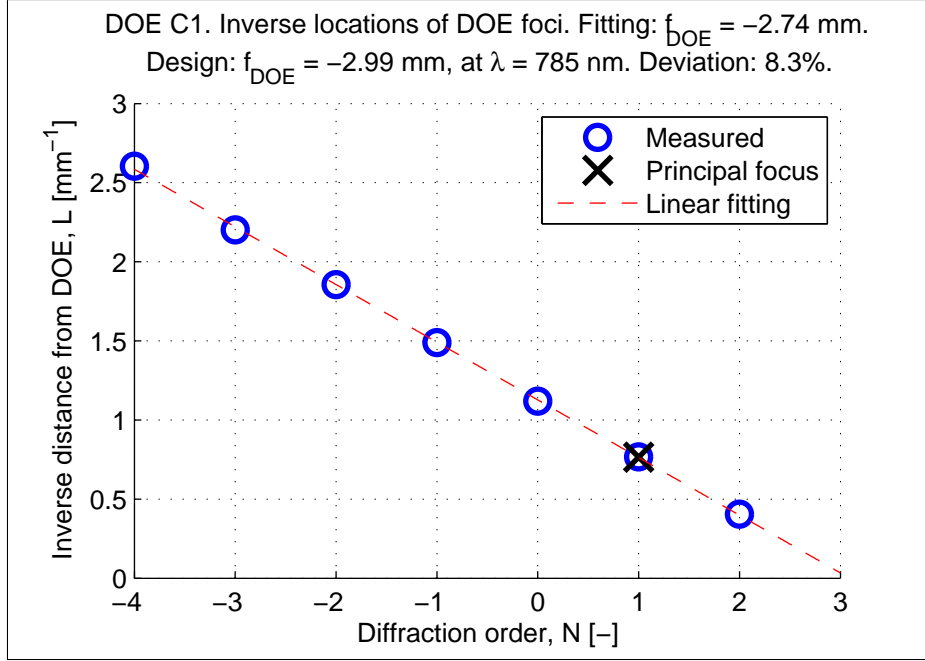


Figure 5.1.2: The figure shows the inverse values of the measured locations of the different diffraction order foci. The principal focus is found at $N = 1$. A linear function is fitted to the data, and equation (5.1.1) is used to extract the DOE focal length f_{DOE} from the fitting function. The resulting focal length differs by 8.3% from the design focal length for this DOE.

The measured data points are clearly following a linear function, in remarkably good accordance with the simple paraxial theory of equation (5.1.1). In figure 5.1.2, a linear fitting function is also shown. Hence, the focal length of each DOE is determined from the linear fitting. In table 5.1, the design values and the measured values of all four DOE focal lengths are shown, together with the relative differences. Also, normalized values (using the focal length of DOE C1 as reference) are given.

Table 5.1: Design values and measured values of the DOE focal lengths, and the corresponding relative difference. All values are given for the wavelength $\lambda = 785$ nm. Also, normalized focal lengths from design and measurements, respectively, are given.

DOE no.	Designed focal length [mm]	Measured focal length [mm]	Relative difference	Designed focal length, normalized	Measured focal length, normalized
C1	-2.99	-2.74	8.3%	f_{C1}	$f_{C1,meas}$
C2	-1.98	-1.83	7.6%	$0.66f_{C1}$	$0.67f_{C1,meas}$
C3	-1.70	-1.57	7.4%	$0.57f_{C1}$	$0.57f_{C1,meas}$
C4	-1.62	-1.47	9.3%	$0.54f_{C1}$	$0.54f_{C1,meas}$

It can be seen in table 5.1 that the measured focal lengths differ from the design values by about 7-10%. However, the *relative* focal lengths found by the measurements are in very good agreement with the design. The ideal focal lengths at $\lambda = 785$ nm have been calculated from the values specified at the design wavelength $\lambda_0 = 770$ nm, through a simple scaling with the factor (λ_0/λ) . This is justified by the paraxial model of the DOE outlined in appendix A.2; equation (A.2.15) shows that the product λf_{DOE} is constant, so that:

$$f_{DOE}(\lambda) = \frac{rd}{\lambda} = \left(\frac{\lambda_0}{\lambda}\right) f_0, \quad (5.1.2)$$

where $f_{DOE}(\lambda)$ is the focal length at wavelength λ , and f_0 is the focal length at the design wavelength λ_0 .

5.1.3 Discussion and summary

The deviation in the DOE focal length from the design value is not easily explained. One possible reason might be the difficulty of defining the focal length of the DOE in the first place. As the DOE is designed to operate in a convergent optical field, whereas focal length is always defined for a collimated light field, the DOE does not necessarily behave as an ideal thin lens. The DOE is also aberration compensated for the case of convergent light, and this compensation does not work properly for collimated light. Associating a focal length with a DOE intended for use in convergent light is simply not a precise business. A more robust simulation of the cavity would probably give somewhat different results.

Furthermore, the paraxial approximation may not hold at all points in the calculations, which may of course also affect the calculated focal lengths. Also, if the light field incident on the DOE is propagating at an angle with respect to the optical axis, the distribution of focal points will be stretched out. In the fitting algorithm, this will be interpreted as the DOE having a stronger diffractive power than is actually the case. So, at least some fraction of the discrepancy might be due to such an effect.

A problem associated with the measurement procedure itself is the difficulty to correctly identify the position of each focus. The manual translation stage may introduce errors. Moreover, the focal points were located from simple ocular inspections of a CCD image in real-time. This adds additional uncertainties to the measured data. The method could be improved by using a motorized stage, recording the intensity distribution with high resolution in the direction of propagation, and extracting the peak intensity on the optical axis from these images by means of an automated computer algorithm.

Finally, the DOE was not index matched to the lens L_2 in this experiment. An extra Fresnel reflection (in addition to the Fresnel reflection from the diffractive surface) is therefore present, which may cause a disturbance to the light distribution, as the reflected field is coherently added to the diffracted light.

To sum up, the investigation reveals that the measured DOE focal lengths differ only a few percent from the design values, and it can be believed that this discrepancy is due to the approximations used in the theoretical model and/or poor alignment of the cavity elements, together with possible disturbances from reflected light.

It should be mentioned here that the question of the DOE focal length is addressed also in section 5.3.7, where a robust model of the DOE has been used. The results from the simulations described there indicate that the focal length of the first DOE (C1) is indeed very close to the design value. Combined with the fact that the *relative* focal lengths measured with the method outlined here are in remarkably good agreement with the normalized design values, it can be believed that the DOEs do most likely work as intended as far as their focal lengths are concerned. Probably, some systematic error in the measurement method introduced in this section is responsible for the detected discrepancies.

5.2 DOE efficiency, direct measurement

We have now quantified the DOE focal lengths, and the remaining important question to be investigated is the DOE efficiency. The intra-cavity lenses are anti-reflection coated, so that the reflection loss per surface is very low (specified to $< 0.4\%$). For one cavity round trip, each lens surface is traversed twice, and there are 3 glass/air boundaries (the DOE is index matched to the second lens). Thus, the total loss due to the lens Fresnel reflections is maximum $1 - 0.99^6 \approx 6\%$.

The external mirror has been seen to have an effective loss of about 13%, but is only traversed once per roundtrip. The DOE, on the other hand, is assumed to have an efficiency in the range 70-90% (very good diffractive elements may reach 95% or so), and is traversed twice per roundtrip. The DOE loss may then be as high as 20-50% per roundtrip, and is probably the dominant cavity loss factor. It is therefore of great importance to determine the DOE efficiency. If the DOE efficiency turns out to be too low, the DOE design and manufacturing process must be investigated, or ultimately the cavity design may need to be changed.

5.2.1 Measurement setup

The most straight-forward approach to determine the efficiency is to measure the power in the principal diffraction order and compare with the total power transmitted through the DOE. This method was implemented and tested, and the procedure is presented in the following.

A sketch of a setup for a direct measurement of the DOE efficiency is shown in figure 5.2.1. It is necessary to use essentially the entire ECL cavity, because the DOE is designed to work in a convergent light field. The detector BPW34 is reverse biased 5.18 V, and connected in series with a 10 k Ω resistor. The detector signal is given by the voltage drop over the resistor. The dark signal is 0.06 V, which is negligible. The translation stages are motorized and are driven by a Labview program, which also samples the detector signal. A 900 μ m aperture is mounted just above the DOE to make sure that the detector will not be overfilled.

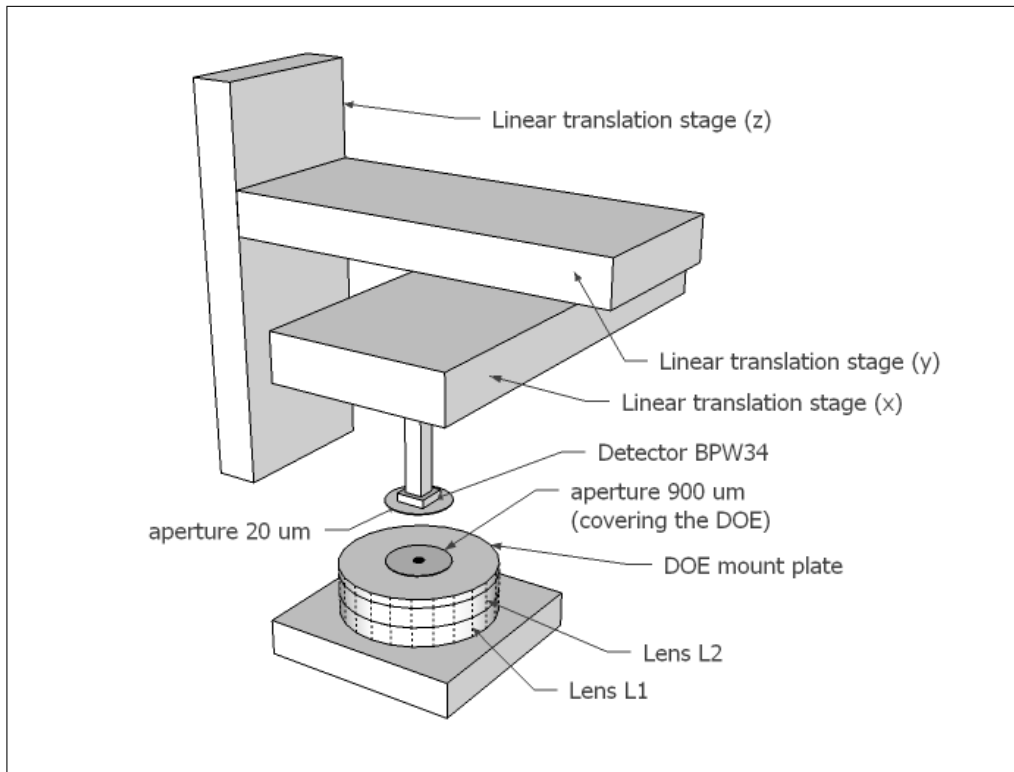


Figure 5.2.1: The setup used for the direct DOE efficiency measurements.

The Hitachi HL7851G laser diode was used as light source, and the laser was run just above the threshold in order not to saturate the detector or the voltage meter. The output laser power depends heavily on temperature and other parameters, and it was therefore necessary to use the monitor detector included in the laser package and a feedback circuit to regulate the drive current for constant output power.

It was soon observed that the detector itself causes strong backward reflections, causing resonant phenomena. In addition, the aperture film also gives rise to stray light reflections going back into the laser and onto the monitoring detector. This makes the laser power control rather unreliable, and the momentary drive current was therefore measured during each measurement.

The momentary drive current was used to re-scale the measured data by means of the $P-I$ characteristic of the laser (measured separately), but again, its correlation with the output power is temperature sensitive, and the scaling is then unreliable in itself. In addition, these drive current measurements had to be taken manually, and it was therefore difficult to read off the correct value at the exact moment when the detector signal was maximum. This puts the ultimate limit to the reliability of the measurement. In the following graphs, all data have been re-scaled according to the laser current changes.

5.2.2 Total power at DOE

The total power at the DOE surface was measured by positioning the detector, with the $20\ \mu\text{m}$ aperture removed, very close to the $900\ \mu\text{m}$ aperture, and then the signal was sampled in a square grid. The result is shown in figure 5.2.2, and a histogram displaying the distribution of the measured data is found in figure 5.2.3.

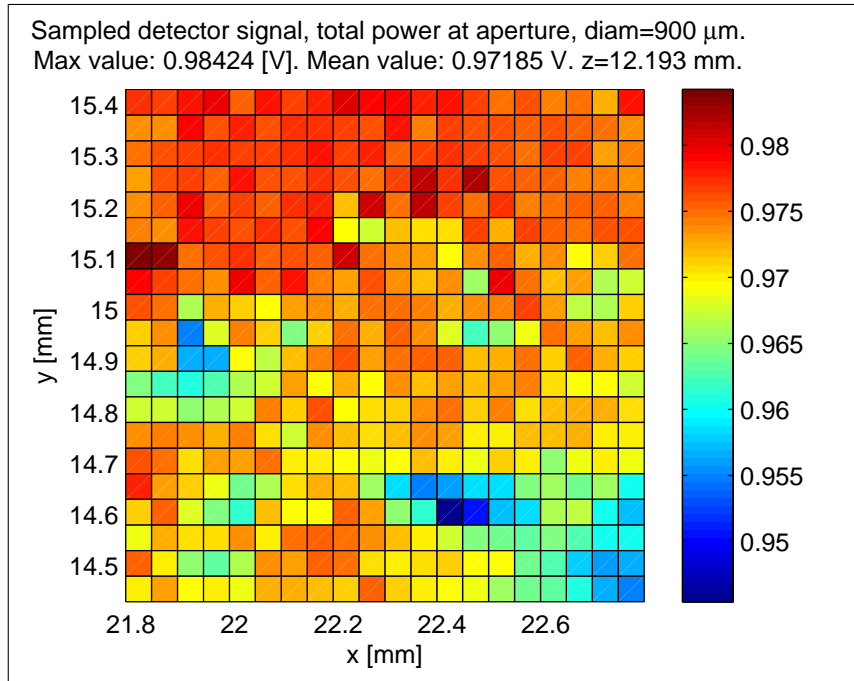


Figure 5.2.2: The reference signal measured with the detector (with the $20\ \mu\text{m}$ aperture removed) close to the DOE.

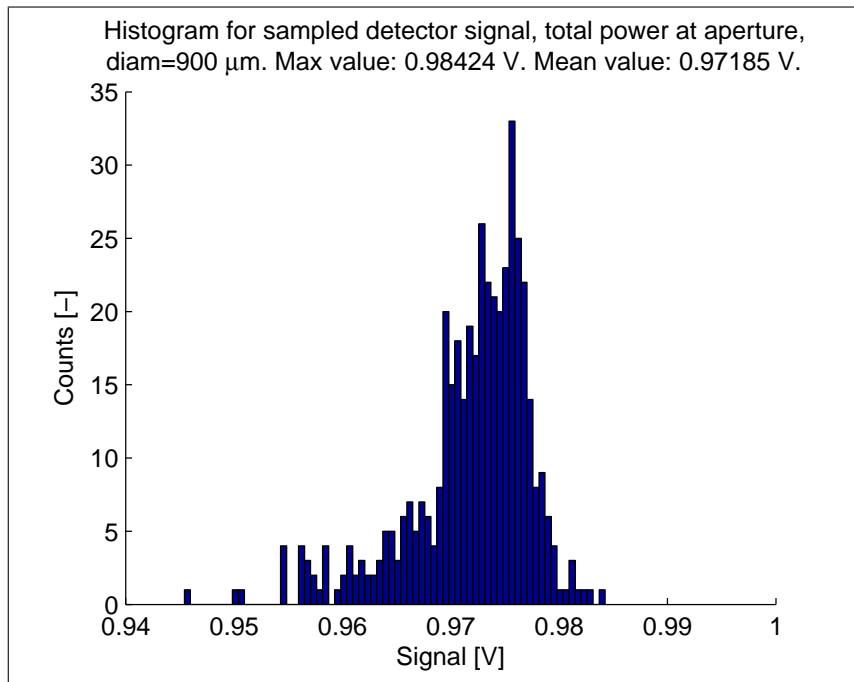


Figure 5.2.3: Histogram for the reference signal measured (with the $20\ \mu\text{m}$ aperture removed) close to the DOE. The mean value is 0.97 V, and 92% of the samples lie within $\pm 1\%$ from the mean value.

The variations seen in figure 5.2.2 are due to the backscattering of light onto the monitor detector (and probably resonant effects), and the drive current varies accordingly. 92% of the samples lie within $\pm 1\%$ from the mean value. The mean value $U_{ref} = 0.97$ V is therefore used as reference.

5.2.3 Power in the diffraction orders

A $20\ \mu\text{m}$ aperture was glued to the detector, with a $200\ \mu\text{m}$ shim in between, in order to suppress reflections from the detector surface going back into the laser. This effect is otherwise very strong, as the detector is positioned in a focus, which is an image of the laser output facet. The detector will then play the role of an external mirror.

The detector with aperture was scanned in a volume around the first diffraction order with increasingly fine grid, until a maximum signal was found. The transverse scan (at constant z value, see figure 5.2.1 for coordinate directions) containing the maximum signal is shown in figure 5.2.4. The maximum signal is seen to be 0.77 V.

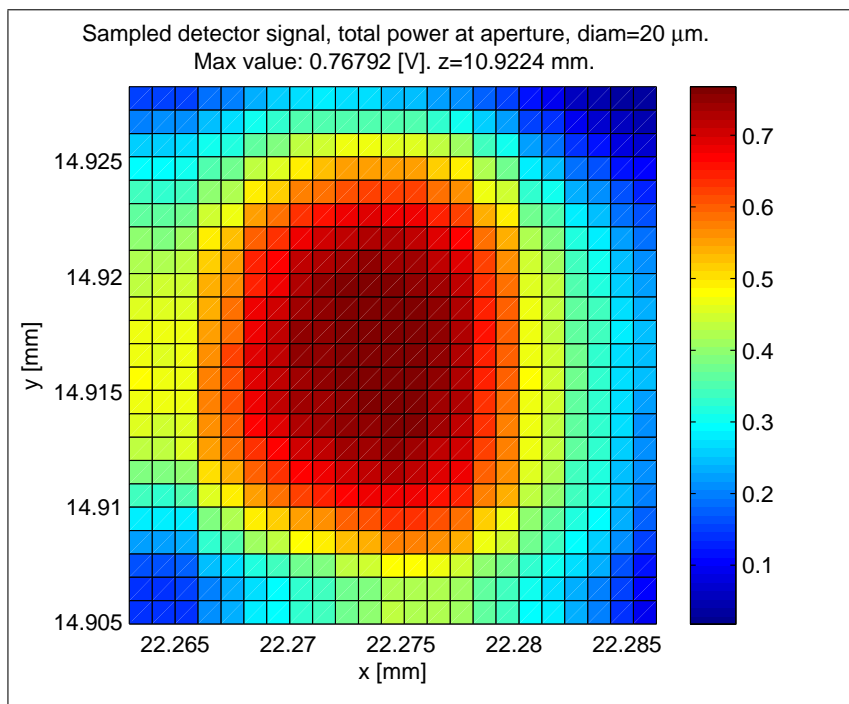


Figure 5.2.4: Transverse scan through the first diffraction order focus with a $20\ \mu\text{m}$ aperture.

Identical scans were made in adjacent z planes, and the maximum detector signal for each plane is plotted in figure 5.2.5.

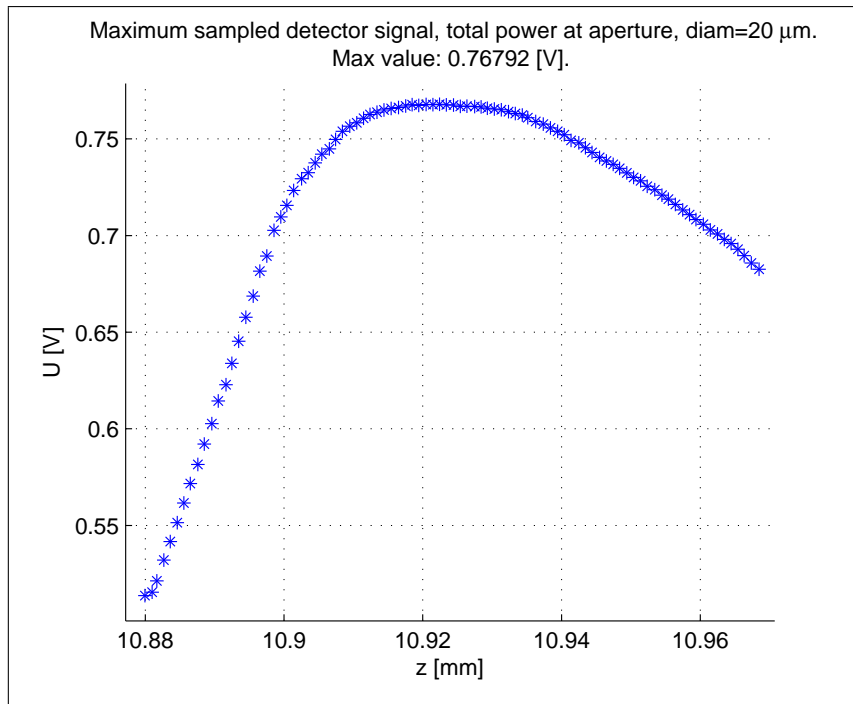


Figure 5.2.5: Maximum signal as function of z , measured around the first diffraction order focus with a 20 μm aperture.

It can be observed that the detector signal is essentially constant over a few samples around the maximum signal, indicating that the aperture used is wide enough not to disturb the field when correctly positioned at the focus.

It was possible to reach also the zeroth order focus (closer to the DOE than the first order), and the results are shown in figures 5.2.6 and 5.2.7, respectively.

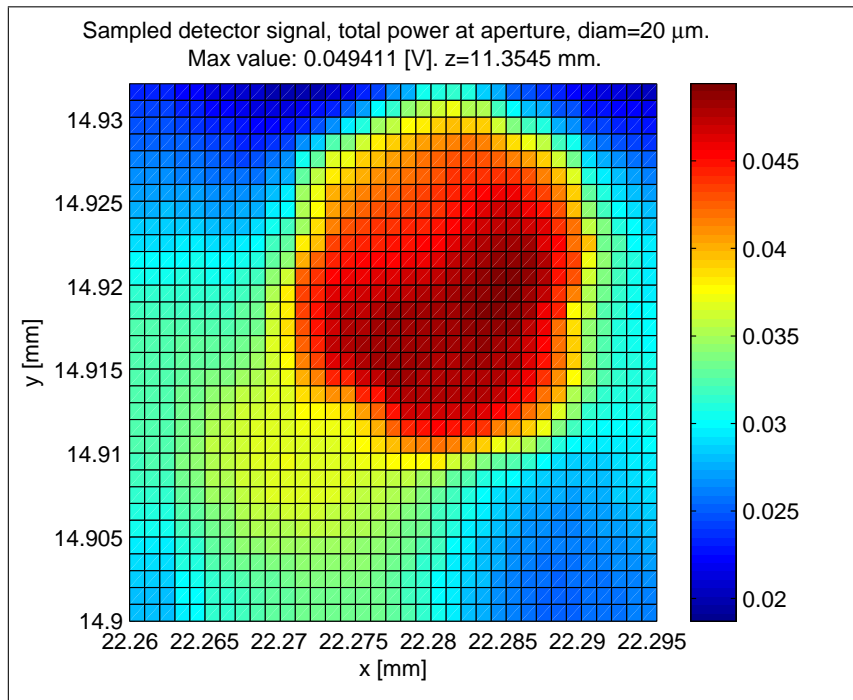


Figure 5.2.6: Transverse scan through the zeroth diffraction order focus with a 20 μm aperture.

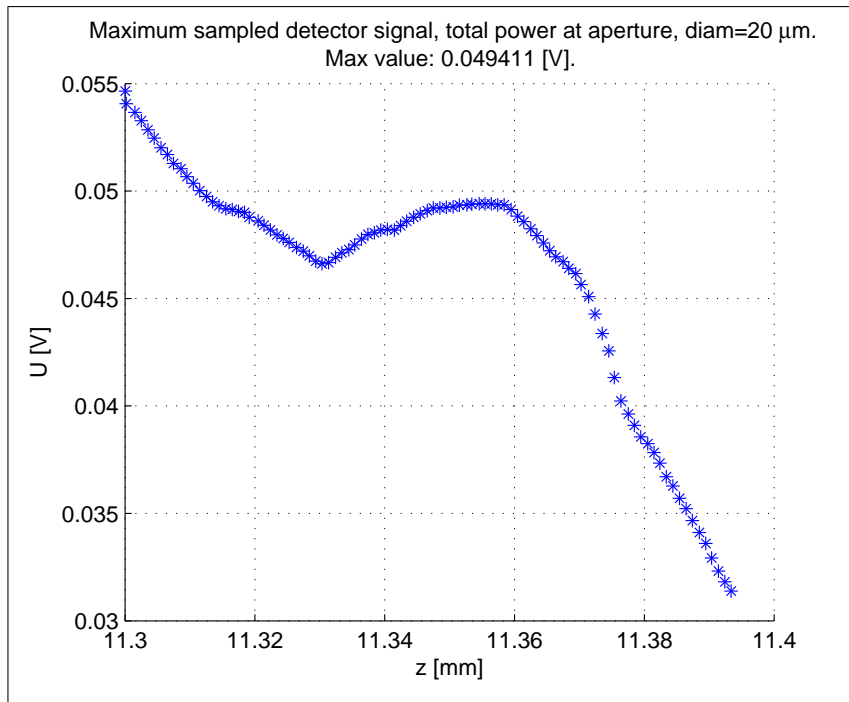


Figure 5.2.7: Maximum signal as function of z , measured around the zeroth diffraction order focus with a $20\ \mu\text{m}$ aperture.

The maximum signal in the zeroth order focus is seen to be $0.049\ \text{V}$. Now, in order to compare these results to the situation without the DOE, similar measurements were carried out with the DOE removed.

5.2.4 Measurement without DOE

A reference signal was taken close to the lens L_2 (without the $900\ \mu\text{m}$ aperture, as it appeared to block some light). A volume scan with the $20\ \mu\text{m}$ aperture was captured around the focus. The reference scan was very similar to the ones showed earlier, and only the mean value is given here: $U_{ref,noDOE} = 0.99\ \text{V}$. The scan through the focus is displayed in figure 5.2.8 (xy scan) and in figure 5.2.9 (z scan), respectively.

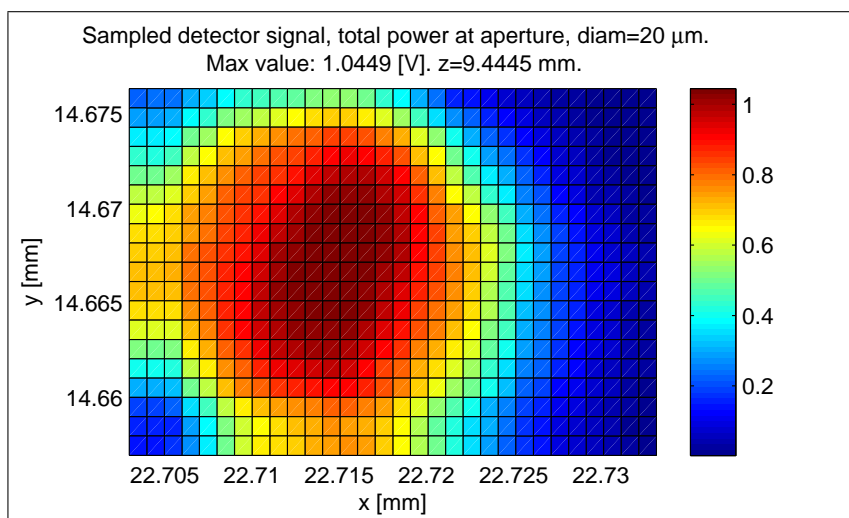


Figure 5.2.8: Transverse scan through the focus with a $20\ \mu\text{m}$ aperture, when the DOE has been removed.

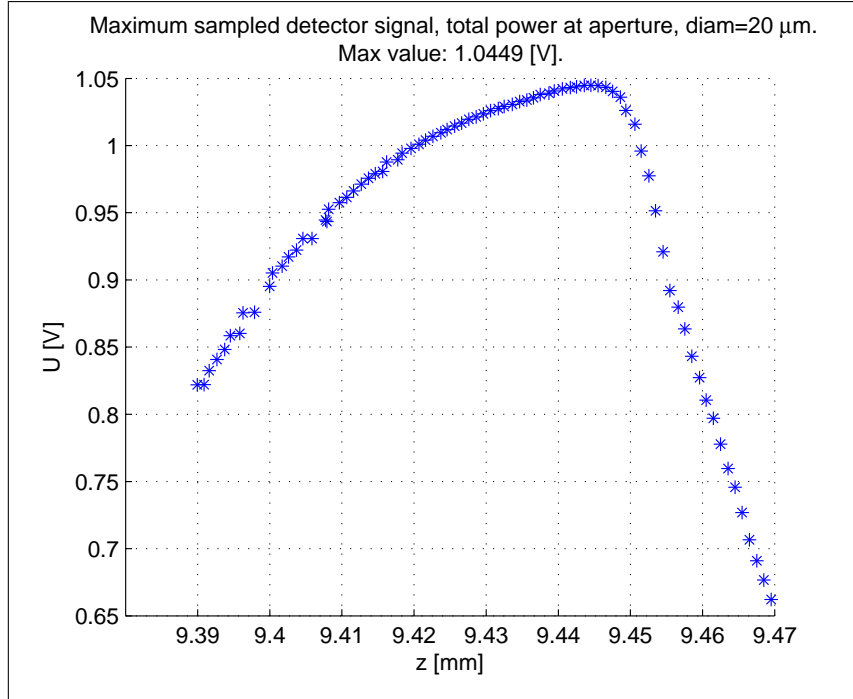


Figure 5.2.9: Maximum signal as function of z , measured around the focus with a $20\ \mu\text{m}$ aperture, when the DOE has been removed.

5.2.5 Summary and conclusions

All results are gathered in table 5.2. The measurement at the lens L_2 without DOE is used as the reference for normalization. The two measurements without the DOE do not agree perfectly, but the difference is within the resolution limit in the laser current, which was used to compensate for the optical feedback effects, as explained earlier.

Table 5.2: Summary of results from the DOE efficiency measurements. The normalized signals use the measurement at the lens without DOE as reference. The discrepancy between the two measurements without the DOE is within the resolution limit for the drive current.

Measurement	Detector signal [V]	Normalized signal [%]
At lens, without DOE	0.99	100
Focus, without DOE	1.04	105
At DOE	0.97	98
Order 1	0.77	77
Order 0	0.049	5

In table 5.2, we note that the total power at the DOE surface is slightly lower compared to the case without the DOE. This is expected, as a 4.5% reflection will occur at the DOE/air boundary. The first and zeroth orders contain 82% of the total power. Assuming that a few percent will be found in the remaining convergent diffraction orders, 85-90% of the incident power is accounted for. The remainder is expected to be found in the divergent orders, and some amount is probably lost through diffusive spread, dust, contaminations etc.

Given the uncertainties introduced by the resonant effects and reflections onto the monitor diode, the total DOE efficiency can be estimated to be somewhere in the range $77 \pm 5\%$, including the Fresnel reflection. The rather large uncertainty in the measured diffraction efficiency calls for a more robust way to determine this entity. In the following section, a different approach to the efficiency problem is presented.

A final remark regards the wavelength; the DOE is designed for 770 nm, whereas the laser HL7851G operates at 785 nm. The difference is only about 2%, and the expected efficiency reduction is less than 0.2% (see figure 5.3.19 in section 5.3.8). Hence, the diffraction efficiency measured with this laser is essentially the same as for the design wavelength 770 nm.

5.3 DOE efficiency, interferometric measurement

As described above, the direct measurement method used to determine the DOE efficiency turned out to be rather uncertain. The laser source used was easily disturbed by backward reflections from the detector, causing resonant effects. Also, reflections onto the monitor detector behind the laser, used to stabilize the optical output power, made the results unreliable. Due to mechanical limitations, it was only possible to reach 2 diffraction order foci.

As the DOE is such an important component in the laser cavity, these shortcomings call for a better measurement method. In particular, the insertion of a detector just at the focus is troublesome. The detector acts just as an external mirror, so that the system will behave as a resonant cavity. Therefore, a method that avoids the need of placing the measurement plane in the vicinity of the focal points is necessary.

In this context, the idea of measuring the diffraction pattern caused by the interference of the different diffraction orders was born. If a suitable model of the DOE is at hand, the parameters of the model can be adjusted until the model reproduces the diffraction pattern measured in the lab. Then, the micro-scale shape of the DOE can be determined, and the diffraction efficiency calculated.

5.3.1 Measurement setup

The measurement setup used is shown in figure 5.3.1. A HeNe-laser was used as light source, partly due to its high quality beam, and the fact that a visible light source simplifies alignment. A more important aspect is that the wavelength (632 nm) differs 18% from the DOE design wavelength (770 nm), which implies that the optical power will be more evenly distributed among the orders. This means increased visibility of the interference pattern.

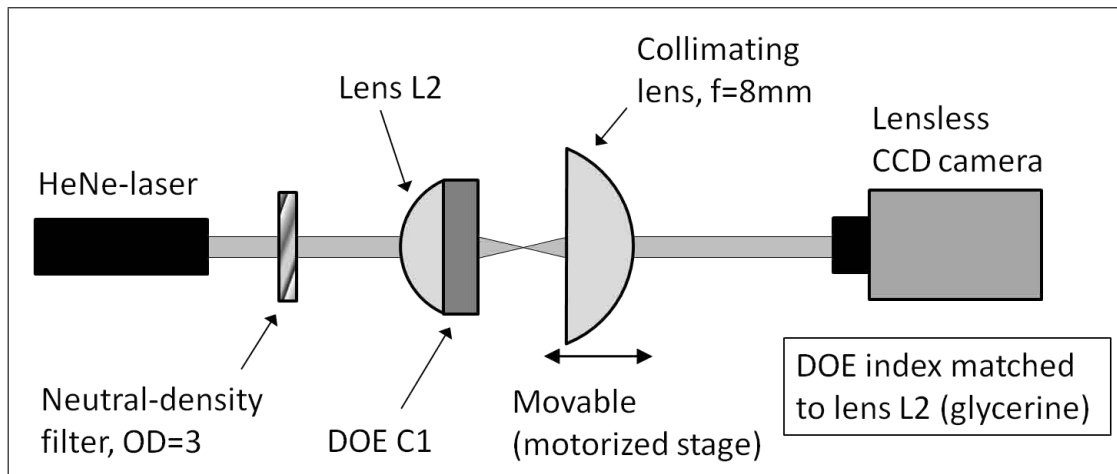


Figure 5.3.1: Sketch of the measurement setup used for DOE efficiency measurements utilizing the interferometric measurement method. The DOE is index matched to the lens L_2 with glycerine. The collimating lens is mounted on a motorized precision stage.

As shown in figure 5.3.1, the lens L_1 has been removed, as the laser beam is already collimated. This simplifies the setup, and a few extra surfaces are avoided. The lens L_2 and the DOE were aligned to each other using a red LED as light source, a collimating lens and a CCD camera. First, the lens was mounted relative to the LED, so that a focus was created. The focus was imaged onto the CCD camera (with the lens removed).

A small droplet of glycerine was deposited on the planar surface of lens L_2 , and the DOE was then put in place. The imaging lens was adjusted so that the DOE surface was imaged onto the CCD. The DOE was finally adjusted in the transverse plane until the CCD image appeared as symmetric as possible. All diffraction rings were then concentric. When the result was satisfactory, the DOE was fixated in the current position (using two screws).

The red LED could now be removed, and the DOE plus lens L_2 was mounted as shown in figure 5.3.1. A pair of imaging lenses was used extensively during the setup alignment procedure. First, the HeNe-laser was set up, generating a spot on a screen. The lens pair was inserted and adjusted until the spot was back in its initial position. Then, the DOE-lens subsystem was mounted, so that a circular diffraction pattern could be seen on the screen.

The DOE-lens system was adjusted until the centroid of the diffraction pattern coincided with the original spot position. Finally, the imaging lens pair was removed. A single lens was mounted on a motorized stage, and then aligned to the entire system so that the interferogram was once more in the correct position on the screen. The CCD camera was positioned in place of the screen. When the setup had been tested and found to be stable, interferograms were recorded for different lens positions, with a stage resolution of 0.01 mm.

Now, the system described is much less sensitive to resonant effects than the direct method presented earlier. This is because the interferograms are recorded when the system is *unfocused*, and therefore only a very small amount of the reflections from the CCD will be imaged back into the laser. Furthermore, it is actually not important any longer that the laser power stays constant. The interferograms contain the information of the relative magnitudes of the diffraction orders, and can therefore be normalized. The crucial entity to measure is the *shape* of the interference pattern, not its absolute intensity.

5.3.2 Model of the DOE

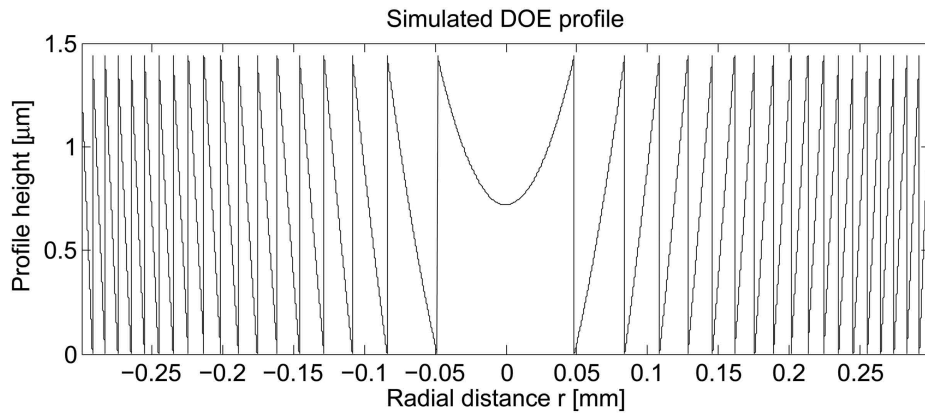
A very simple model of the physical DOE can be created by taking the ideal DOE shape (available from design parameters), and convolving this shape with a Gaussian function having an $1/e$ width σ (unit [μm]):

$$H(r) = A \exp \left\{ - \left(\frac{r}{\sigma} \right)^2 \right\} \quad (5.3.1)$$

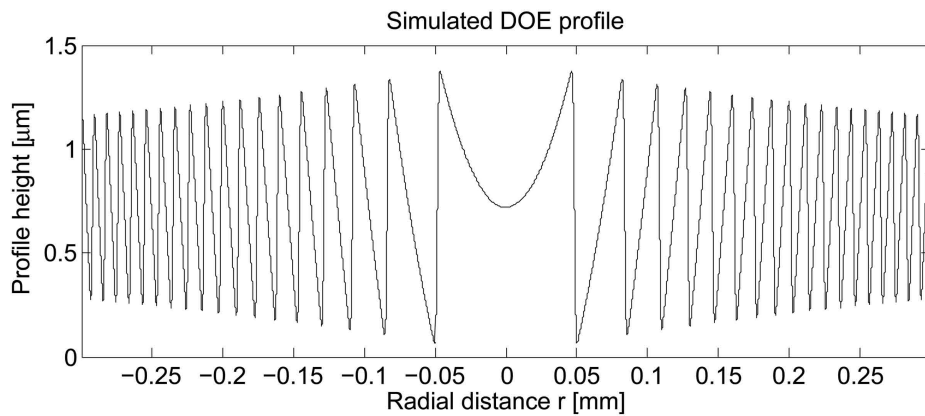
where r is the radial distance and has the same unit as σ (μm). In the frequency domain, the convolution is transformed into a multiplication with a function which is still Gaussian, and its $1/e$ width is then given by $\sigma_f = 1/(\pi\sigma)$. The constant A in equation (5.3.1) is chosen so that the Gaussian function in the frequency domain is normalized to 1, when using the Matlab fast Fourier transform on the convolution function.

Convolving the DOE profile with the function in equation (5.3.1) will result in corner rounding at all sharp edges of the structure, which in turn causes the depth of the structure to decrease when the period of the DOE gets smaller. This is a one-parameter model describing the proximity effects in the manufacturing process. Hence, the larger the value of σ , the worse the corner rounding and the shallower the DOE profile far away from the center.

In figure 5.3.2(a), a line scan of the ideal DOE profile is shown, and in figure 5.3.2(b), the same profile convolved with a Gaussian function of $1/e$ width $\sigma = 1.06 \mu\text{m}$ is given. The profile depth decrease with the radial distance is clear from figure 5.3.2(b).



(a) The ideal DOE, overview.

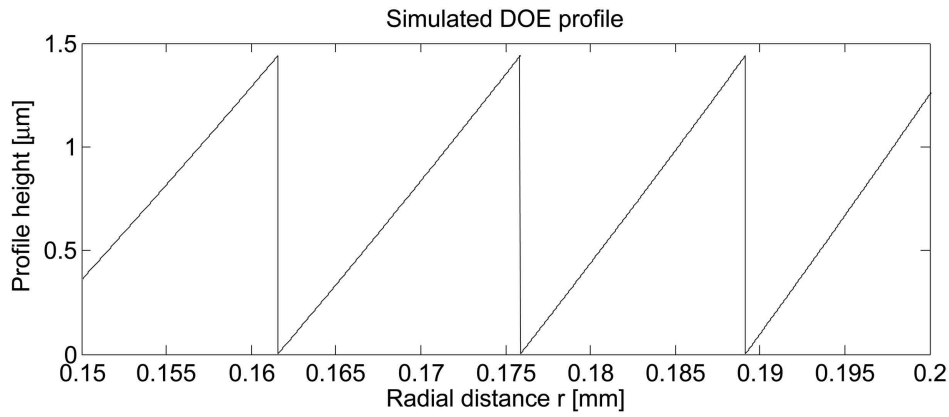


(b) The DOE convolved with a Gaussian function of $1/e$ width $\sigma = 1.06 \mu\text{m}$.

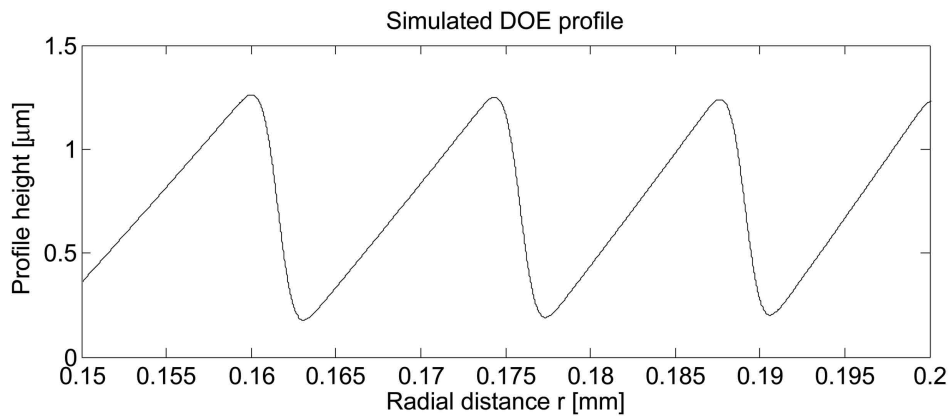
Figure 5.3.2: The ideal DOE compared to a non-ideal DOE, generated through convolution with a Gaussian function.

Comparing figures 5.3.2(a) and (b), it is also obvious that the maximum profile depth becomes smaller due to the proximity effects. This error can be compensated for by manufacturing a slightly deeper profile. We will discuss this matter further in section 5.3.8.

The corner rounding effect is not visible in the previous figures. In figure 5.3.3(a), a zoom-in on a fraction of the ideal DOE profile is displayed, and the corresponding profile convolved with the Gaussian function is shown in figure 5.3.3(b). The corner rounding is very obvious in figure 5.3.3(b).



(a) The ideal DOE, zoom-in.



(b) The DOE convolved with a Gaussian function of $1/e$ width $\sigma = 1.06 \mu\text{m}$, zoom-in.

Figure 5.3.3: The ideal DOE compared to a non-ideal DOE, generated through convolution with a Gaussian function. Zoom-in on the profile shape.

5.3.3 Model of the measurement setup

The theoretical model of the entire measurement setup relies on propagation of the starting field distribution at the DOE through the collimating lens to the CCD, by means of the "two-step method" [41]. The two-step method, developed by C. Rydberg and J. Bengtsson, is a simple but powerful tool to calculate the field in an arbitrary plane with an arbitrary sampling distance, by means of two subsequent propagations with the Huygens-Fresnel integral.

The idea of the the simulation model for the measurement setup is explained in figure 5.3.4. The two-step method is utilized in each propagation step shown in the figure, *i. e.* step 1, 3, 5 and 7.

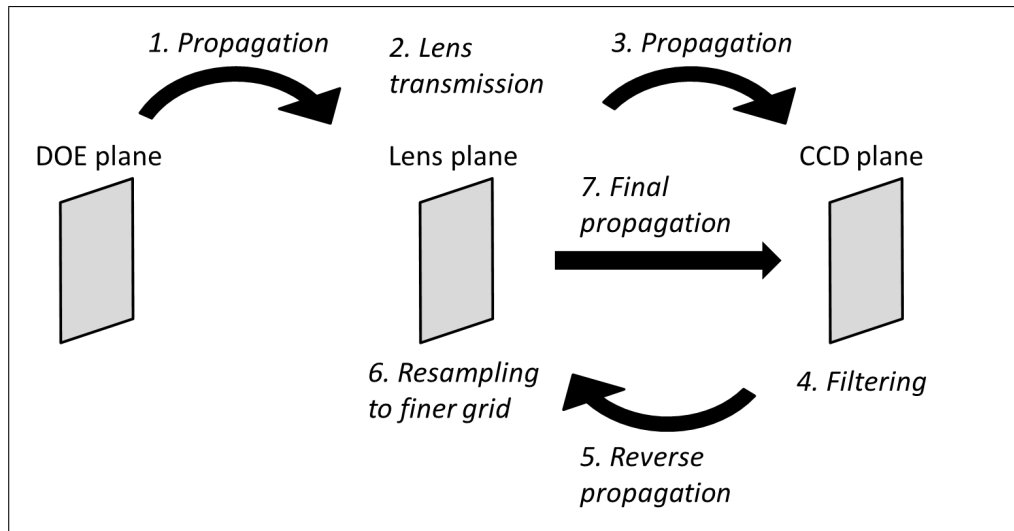


Figure 5.3.4: A sketch of the numerical model of the measurement system. The field at the DOE is propagated to the lens, where the lens phase factor is added to the field. The field is propagated to the CCD plane, where it is set to zero outside a certain radius. Then, this filtered field is propagated back to the lens plane, resampled, and finally propagated to the CCD again, but now at significantly better resolution. The two-step method is applied in step 1, 3, 5 and 7.

A field distribution at the DOE is propagated to the lens plane, where the phase front is modulated by the lens. The resulting field is propagated to the CCD plane. As a fraction of the power is propagating at quite large angles, the sampling distance in the CCD plane must be large in order to avoid overfilling of the calculation window, causing disturbances. However, we are only interested in the field in a very limited area in the center of the calculation window. Therefore, the field in the CCD plane is set to zero outside a certain radius.

This "filtered" field is reverse propagated back to the lens plane, where it is resampled in a denser grid (interpolation is required). Finally, this resampled field is once again propagated to the CCD, but this time, a much smaller calculation window can be chosen at the CCD, thus giving an interferogram having adequate resolution.

The physical distances between the different planes, as well as the width of the beam incident on the DOE, were measured roughly in the measurement setup. The phase curvature of the beam at the DOE plane was estimated from the distance between the laser and the DOE. These values were then calibrated in the model until the simulations reproduced, for instance, the distance between the DOE and the first-order focus, and the intensity profile at the DOE plane.

The DOE is specified to be 0.5 ± 0.25 mm thick, and when measured with callipers, the true value was found to be 0.52 mm. The thickness used in the simulations is 0.56 mm, for best agreement with the measurements. The discrepancy is probably explained by the fact that the index matching of the DOE to the lens L_2 with glycerine gives an extra distance between the components.

5.3.4 Interferogram examples

An example of an interferogram measured in the setup is shown in figure 5.3.5. The quality of the measured data is rather good; the system is well aligned so that the diffraction rings are concentric. In order to suppress noise and irregularities in the interference pattern, we take advantage of the circular symmetry of the pattern, averaging the measured signal in ring-shaped segments centered at the interferogram center, thus ending up with a one-dimensional radial scan of the measured signal. This scan will then be used for comparing the measured data to the simulated intensity pattern.

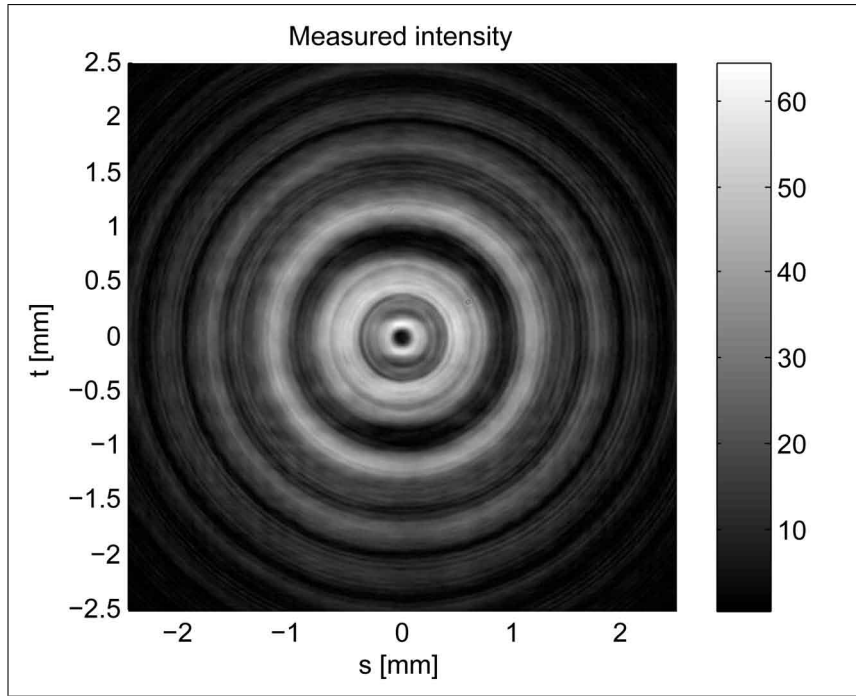


Figure 5.3.5: An example of an interferogram measured in the setup.

In figure 5.3.6, a corresponding simulation for some arbitrarily chosen value of the Gaussian convolution function width σ is shown. The agreement between the simulation and the measured image in figure 5.3.5 is remarkably good. It can be seen in the simulated interferogram that there is some kind of disturbance present close to the center of the image. The reason for this has not been found, but the effect is present regardless of the shape of the interferogram, though more or less pronounced in different planes. A possible explanation is the fact that a circularly symmetric field pattern has been sampled in square pixels. The disturbance in figure 5.3.6 can be seen to have a square symmetry.

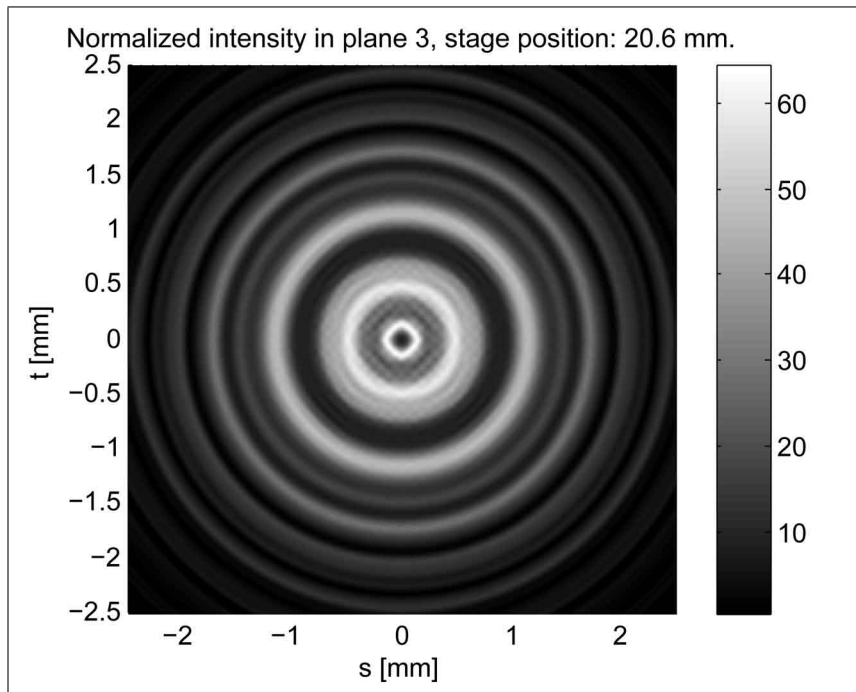


Figure 5.3.6: The simulated interferogram (for some arbitrary value of σ), corresponding to the measurement in figure 5.3.5.

Figure of merit

Six good interferograms were chosen from the measurements to be used for the fitting procedure. The corresponding theoretical intensity distributions were calculated for a sequence of values of the Gaussian convolution function width σ . As the interferograms show circular symmetry, only radial scans need to be studied. This saves computation time when comparing the simulated and measured data, and the noise of the measured interferograms can be suppressed by calculating the radial scan by averaging the intensity in annular rings around the center of each picture. For a certain value of sigma, the figure of merit f_i of the fitting for the interferogram in plane i was defined as

$$f_i = \sqrt{\sum_{m=1}^M [I_{meas,i}(r_m) - I_{simulated,i}(r_m)]^2}. \quad (5.3.2)$$

$I_{meas,i}(r_m)$ is the measured intensity at point (r_m) in plane i (i. e., at the radial distance r_m), and $I_{simulated,i}(r_m)$ is the corresponding simulated intensity. A total figure of merit F , using the information from all the 6 interferograms, was calculated as:

$$F = \sqrt{\sum_{i=1}^6 f_i^2}, \quad (5.3.3)$$

and the best fitting is found for the value of σ for which F is minimized. Of course, a similar merit function can be defined in the two-dimensional case.

5.3.5 Results

In figure 5.3.7, an example of a measured and a simulated radial intensity scan is provided. Due to the problem with numerical disturbances at the center of the interferogram described earlier, the central parts of the interferograms have been removed in the fitting algorithm. The interferograms have been normalized to the peak closest to the origin, after the removal of the central region.

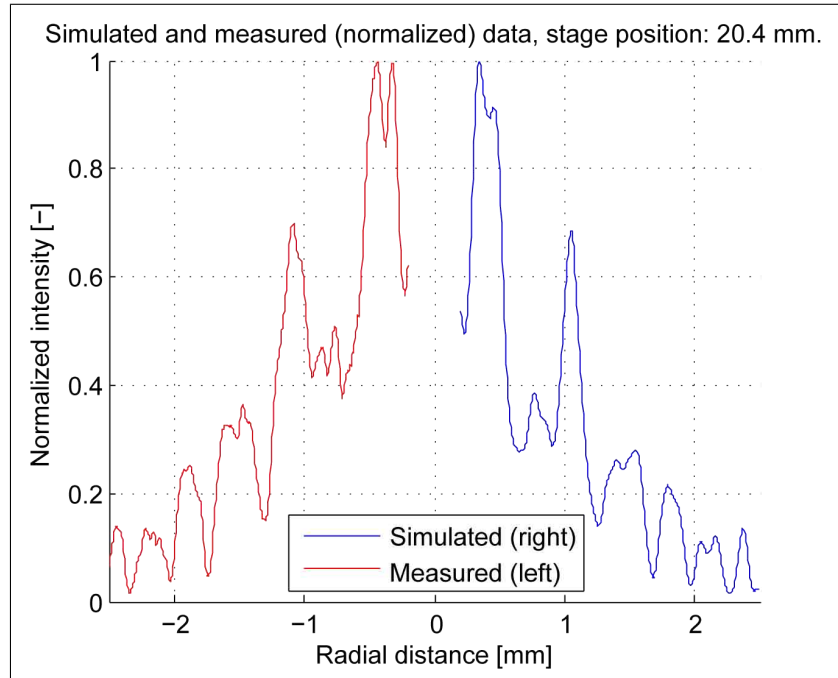


Figure 5.3.7: Example of radial intensity scans, measured (left) and simulated (right). The central parts of the interferograms have been removed due to the numerical noise in this region, making the data unreliable. The data are normalized to the value of the peak closest to radius $r = 0$ after the removal of the central region.

In figure 5.3.7 it can be seen that the simulation matches the measurement very well. The locations of the peaks in the measurement and in the simulation are identical. The relative height of the peaks agree fairly well. The simulation is not capable of resolving all high-frequency variations found in the measurement, due to sampling limitations.

We now vary the Gaussian convolution function width σ , and calculate the figure of merit function F (see equation (5.3.3)) for each value of σ . The resulting value of F as function of σ is found in figure 5.3.8.

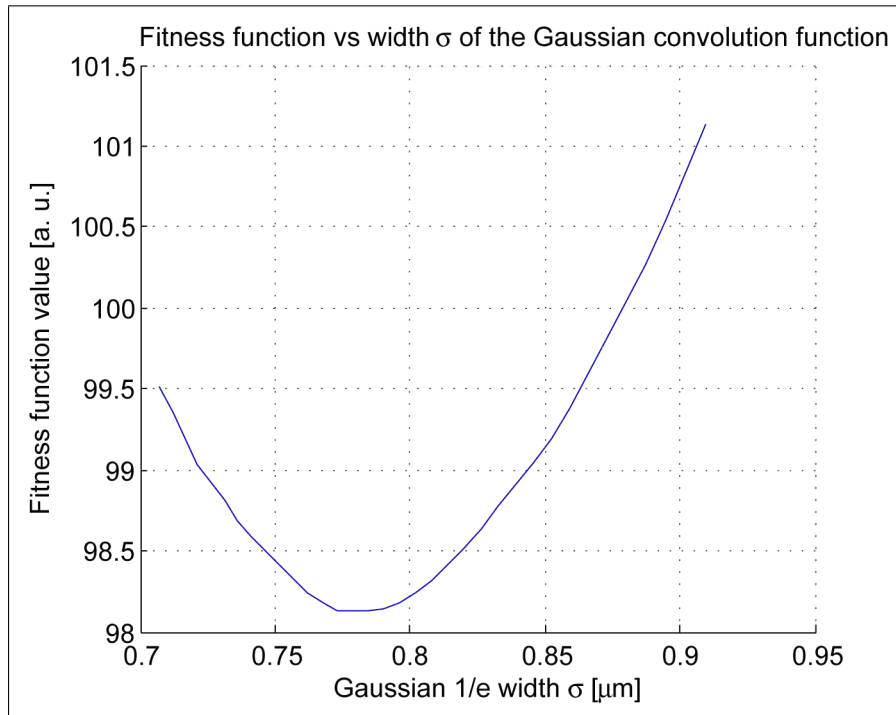


Figure 5.3.8: The fitness measure F as function of the Gaussian convolution function width σ . Result from simulation. The minimum is found for $\sigma = 0.78 \mu\text{m}$.

We observe that the minimum value of F is found for $\sigma = 0.78 \mu\text{m}$. Now, the DOE profile corresponding to this value of σ can be characterized as the profile depth as function of the period of the DOE structure. In figure 5.3.9, such a description of the DOE is presented, together with an AFM measurement performed by Dr. Johan Backlund [40].

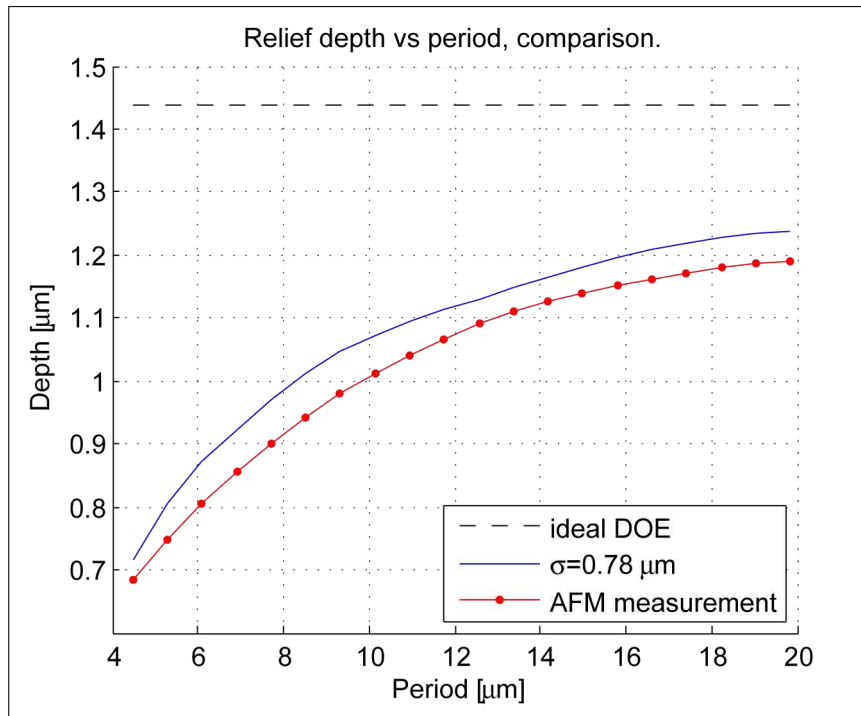


Figure 5.3.9: The depth of the DOE profile as function of the period of the structure. The simulated profile for $\sigma = 0.78 \mu\text{m}$ is compared to an AFM measurement conducted by Dr. Johan Backlund [40]. Note that the AFM line is actually a fitting, the small point do not represent measurement points.

In figure 5.3.9, it can be seen that the general behavior of the simulated DOE is very similar to the results from the AFM measurement. Hence, it can be concluded that the simple one-parameter model, describing the physical DOE as the ideal profile convolved with a Gaussian function is actually very good. We also observe that the simulation gives a profile that is 5-10% deeper (and therefore indicates better optical performance of the DOE) than the AFM measurement result.

There may be many reasons for the small discrepancy between the AFM and the optical measurements; on the one hand, the probe of the AFM has a certain width, meaning that the measured data will be a convolution of the true profile with the shape of the probe. When measuring on the deep profile of the DOE, the depth of the valleys may therefore be underestimated. The AFM measurement was actually performed close to the limit of maximum measurable profile depth.

On the other hand, there may also be errors in the simulations presented here; the numerical disturbances have already been mentioned, the filtering and resampling method may introduce small errors, and the problem with poor sampling also adds uncertainties. In addition, the Fresnel condition for the validity of the approximations used in the propagations, is not strictly fulfilled at all points, which is probably not a large problem, but still may cause some errors.

Now, in figure 5.3.10, the line for $\sigma = 0.91 \mu\text{m}$ has been added to the graph in figure 5.3.9, as well as the true measurement points from the AFM measurement. This value of $\sigma = 0.91 \mu\text{m}$ was chosen to match the AFM measurement as well as possible.

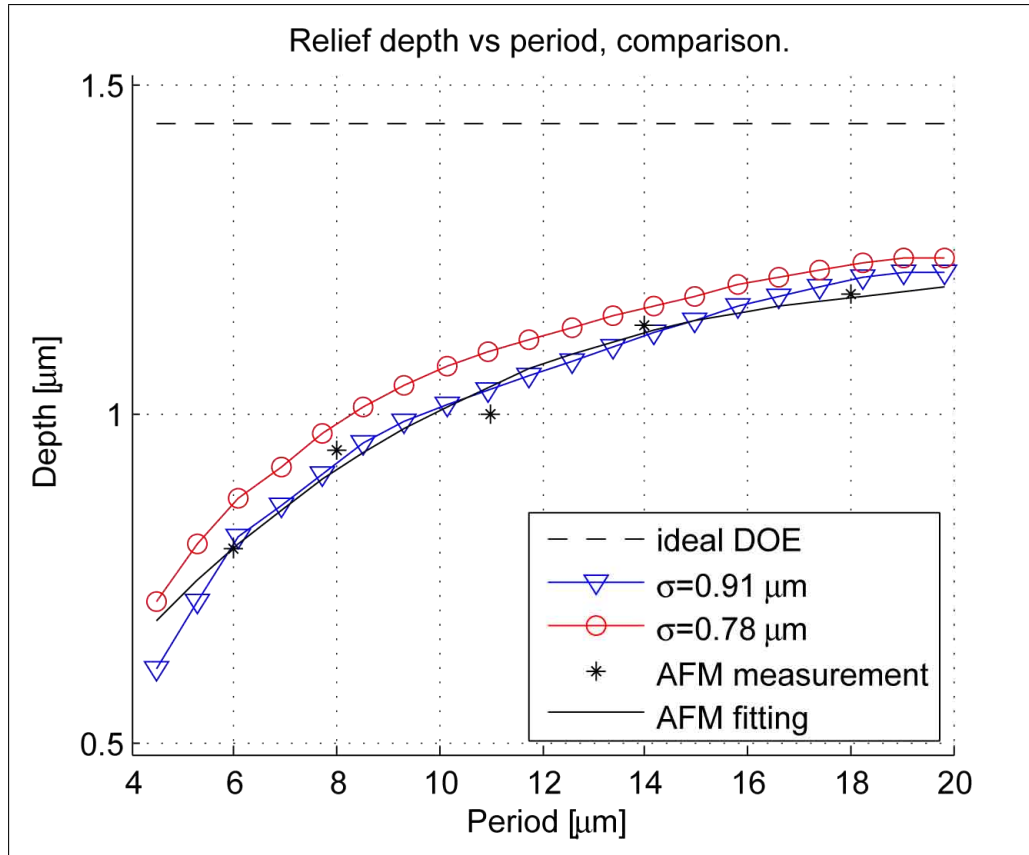


Figure 5.3.10: The depth of the DOE profile as function of the period of the structure. The simulated profile for $\sigma = 0.78 \mu\text{m}$ and $\sigma = 0.91 \mu\text{m}$ is compared to an AFM measurement conducted by Dr. Johan Backlund [40]. The stars represent the true measurement points from the AFM.

Here, it can be seen that the AFM data have some noise, but still, there is a systematic difference between the AFM measurement and the present simulations.

5.3.6 DOE efficiency at $\lambda_0 = 770 \text{ nm}$

The DOE profile has been determined through measurements at $\lambda = 632 \text{ nm}$, and the fitting algorithm gave the value of $\sigma = 0.78 \mu\text{m}$. The DOE can now be simulated at its design wavelength $\lambda_0 = 770 \text{ nm}$. We then want to calculate the efficiency, *i. e.*, the power found in the first diffraction order compared to the total power incident on the DOE.

The incident power is found through simple integration of the intensity at the DOE plane. The power in the first diffraction order is found by integrating the intensity in the central bright spot at the plane where the intensity is strongest. This results in a pure diffraction efficiency of 86.2%.

Fresnel reflections and other sources of loss are not included in the value 86.2%; the index matching between lens L_2 and the DOE will suppress reflections at this boundary to a minimum, but a 4.5% reflection will still occur at the diffractive surface itself at the DOE/air interface. Also, diffusive spread in the DOE substrate has not been quantified, which will lower the efficiency further. It has also been observed that there are some dust particles present on the DOE surface, which means somewhat lower efficiency still. All possible loss contributions to the overall DOE efficiency are listed in table 5.3, where some of the factors have been given estimations, indicated by “~” or “?”.

Table 5.3: Summary of the contributions to the overall DOE efficiency at the design wavelength $\lambda_0 = 770$ nm. The diffraction efficiency is due to the corner rounding, with resulting profile depth error. The total efficiency is estimated to be 81%

	Loss factor	Efficiency factor	Overall efficiency
Incident power	—	—	100%
Truncation	$\sim 0\%$	$\sim 100\%$	100%
Fresnel reflection	4.5%	95.5%	95.5%
Diffraction efficiency	13.8%	86.2%	82.3%
Absorption	$\sim 0\%$	$\sim 100\%$	82.3%
Diffusive spread	$\sim 0\%$	$\sim 100\%$	82.3%
Dust/contaminations	$< 0.5\%?$	$> 99.5\%?$	$> 81.9\%$
Index mismatches	$< 0.3\%$	$> 99.7\%$	$> 81.7\%$
Non-ideal lens AR coating	$< 0.4\%$	$> 99.6\%$	$> 81.3\%$
TOTAL	19%	81%	81%

The overall efficiency, with all loss sources included, can be estimated to be 81%, as seen in table 5.3. This value can be increased if some of the loss contributions can be suppressed. This will be discussed later. For the moment, we conclude that the diffraction efficiency is high, and that the overall efficiency of the element is quite high.

As the DOE is traversed twice per cavity roundtrip, the loss per roundtrip provided by the DOE is therefore $1 - 0.81^2 = 34\%$, which will probably dominate the cavity loss. Hence, any improvement in the diffraction efficiency will strongly improve the cavity performance.

The diffraction efficiency with respect to the principal diffraction order was found to be 86.2%, so the remaining power must be found in the other diffraction orders. The power in (a few of) the *convergent* diffraction orders has been calculated, with the result shown in figure 5.3.11. Summing up the powers in these orders, they contain 6.3% of the total incident power. The power not accounted for, $100 - 86.2 - 6.3 = 7.5\%$ is expected to be found in the remaining convergent orders and in the divergent orders. It is a reasonable assumption that the power contained in the convergent orders will be roughly equal to the power contained in the divergent orders, which also seems to be the case in the simulation.

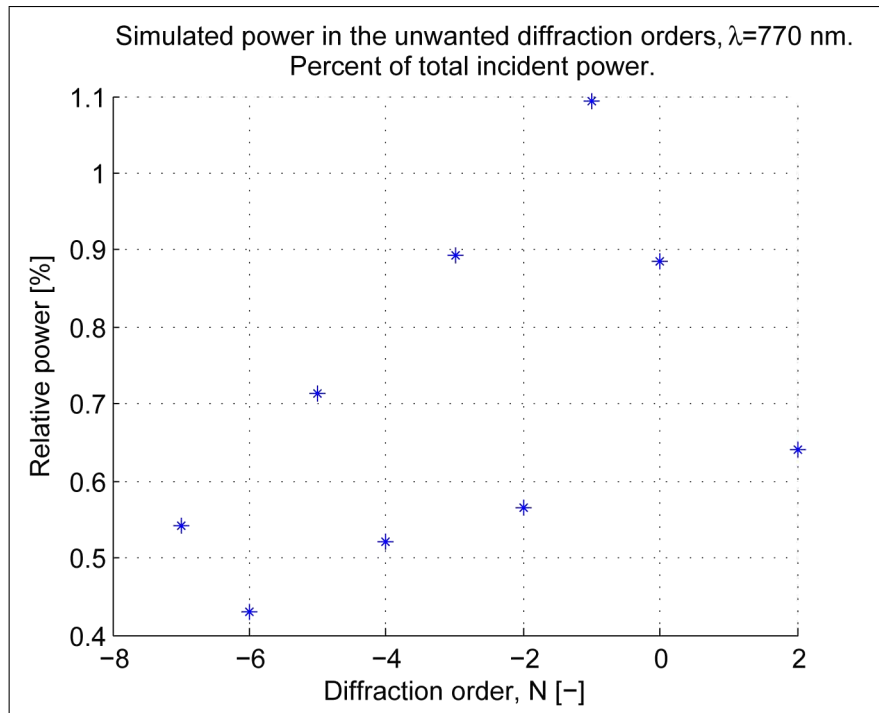


Figure 5.3.11: The simulated relative powers in a few of the convergent diffraction orders, at $\lambda = 770$ nm. The sum of these powers represents 6.3% of the total incident power.

Finally, we want to investigate how sensitive the calculated diffraction efficiency will be to small variations in σ . For that reason, the diffraction efficiency (Fresnel reflections not included) as function of σ has been simulated. The result is presented in figure 5.3.12.

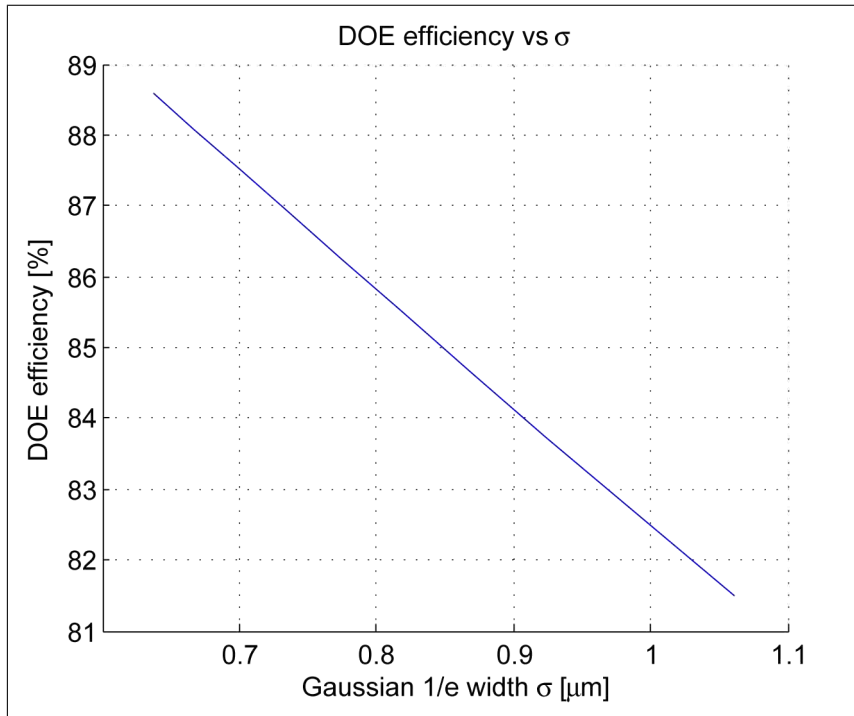


Figure 5.3.12: The simulated DOE diffraction efficiency as function of the Gaussian convolution function width σ . For instance, the diffraction efficiency for $\sigma = 0.91 \mu\text{m}$ (which appeared to match the AFM measurement in figure 5.3.10) is 84%. Hence, the efficiency does not change drastically with small changes in σ .

At $\sigma = 0.91 \mu\text{m}$, the value that lies close to the AFM measurement in figure 5.3.10, the diffraction efficiency is seen to be about 84% in figure 5.3.12; *i. e.*, 2 percentage points (or 2.3%) lower than the efficiency 86% calculated for $\sigma = 0.78 \mu\text{m}$. Thus, the diffraction efficiency is not extremely sensitive to small changes in σ . An estimation of the accuracy of the calculated diffraction efficiency is therefore about $\pm 2\%$.

From the discussion above and table 5.3, the *total DOE efficiency* can be estimated to be $81 \pm 2\%$, including all loss factors. The *pure diffraction efficiency* is $86 \pm 2\%$. This is actually a very good value for a DOE. The (total) efficiency found from the direct measurement method was 77% (see table 5.2), but the figure 77% was of course very uncertain in the first place, so the estimation was $77 \pm 5\%$. Not all the factors in table 5.3 were included in the value 77% (for instance the non-ideal lens AR coating), but these contributions are assumed to very small. Thus, the results from the two methods can actually be considered to agree.

It should be stressed that the diffraction efficiency calculated depends on the width of the incident beam. The wider the beam, the more power will be transmitted through the peripheral regions of the DOE, where the diffraction efficiency is lower.

The width used in the simulations is 0.17 mm $1/e$ half-width of the incident field (or $1/e^2$ half-width of the incident intensity). This value resembles the intensity profile measured at the DOE. In the real laser cavity, the field may be somewhat wider (at least perpendicular to the epitaxy of the SOA), giving slightly lower diffraction efficiency.

DOE "good area"

A good way to visualize the diffraction efficiency is to consider the "effective" area of the DOE having the "correct" shape. The corner rounding of the DOE profile causes the ideal vertical edges to become more sloped. The regions of the DOE that are sloped even in the ideal case are not affected very much by the corner rounding. We may therefore compare the slope of the profile found from the preceding measurements with the ideal shape, and identify the regions where the true slope deviates from the ideal one by less than some given figure q [nm/ μ m].

The summed (projected, planar) area of the "good" regions of the DOE will provide the diffraction of optical power into the desired principal order. For lack of a better word, the term *good area* will be used for this area (after multiplication by a weighting function; see next paragraph). The "bad" regions will send power into all other diffraction orders.

The good regions become smaller when we approach the outer edge of the DOE, due to the short period of the profile. On the other hand, the major part of the incident optical power is found close to the center of the DOE, where its quality is better. We therefore use the Gaussian intensity profile used in the previous simulations (which had a 0.17 mm $1/e^2$ intensity half-width) as a weighting function for all DOE area measures.

We adjust the limit q until the "good" DOE area corresponds to about 86% of the total (geometric) DOE area, thus matching the diffraction efficiency found in the simulations (see table 5.3). The "good regions" of the DOE are represented by small stars in figures 5.3.13 and 5.3.14 below. The graphs are calculated for a good DOE area of 86%.

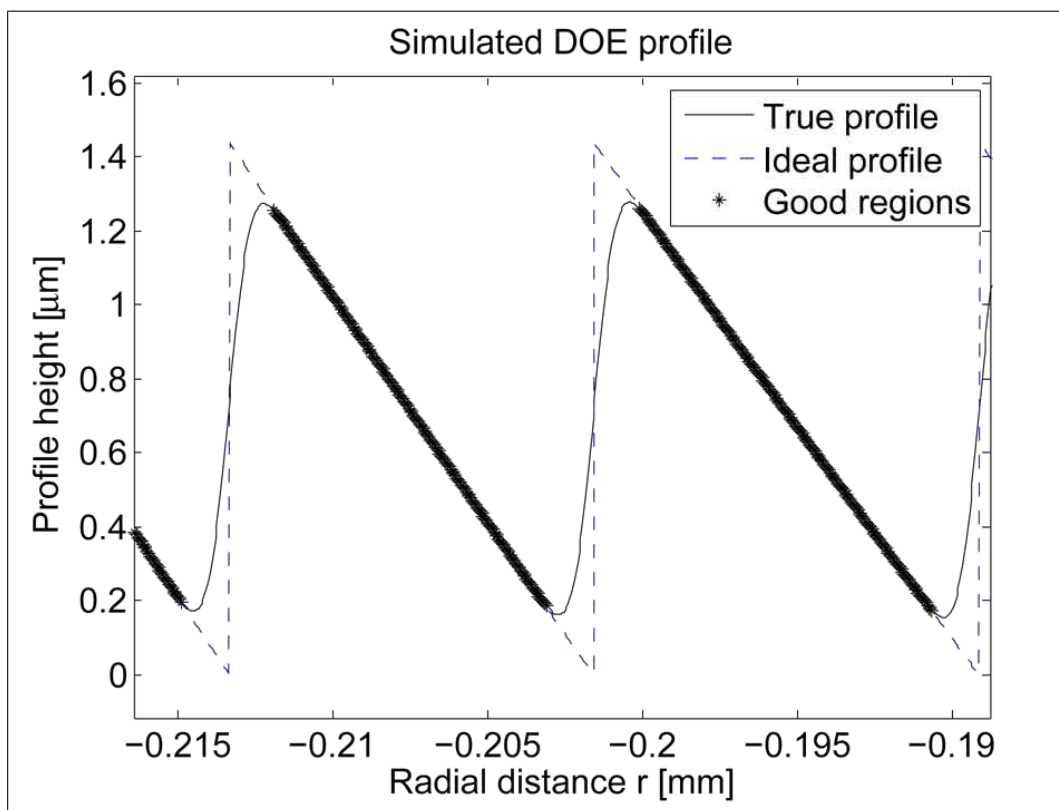


Figure 5.3.13: The picture shows the ideal DOE profile and the true profile close to the center of the DOE. The stars indicate the regions where the slope of the true profile does not deviate more than 20 nm/ μ m from the slope of the ideal profile. Then, the effective good area of the DOE is 86% of the total DOE area, *i. e.*, matching the diffraction efficiency from the simulations.

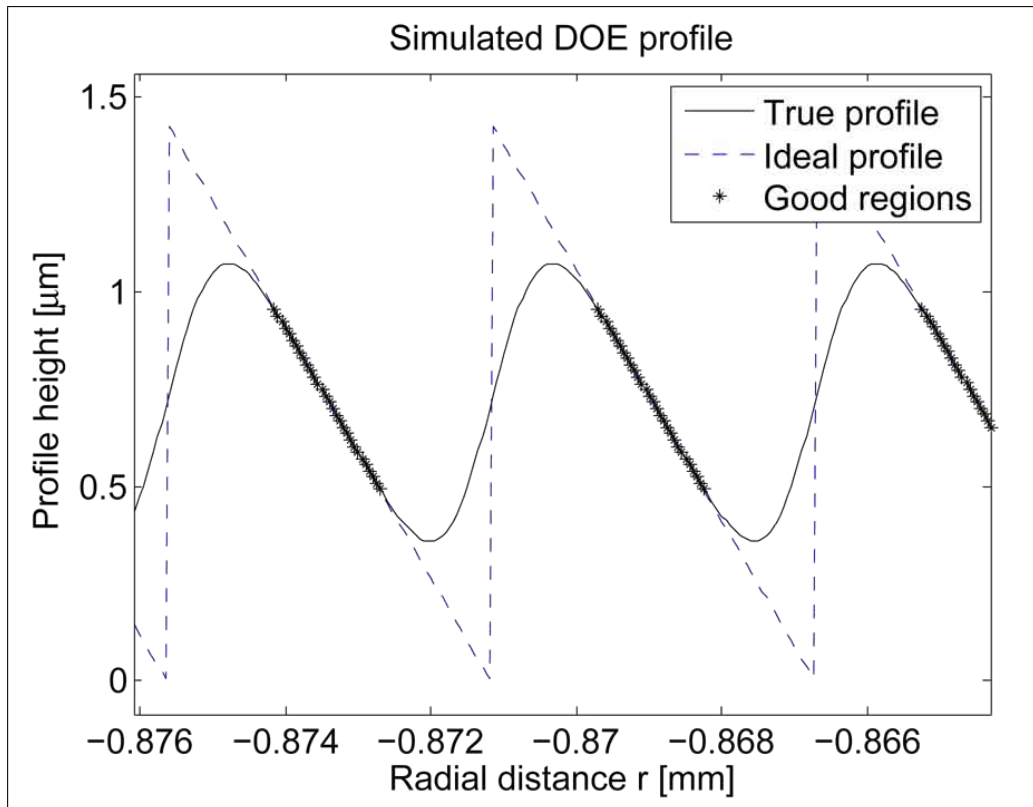
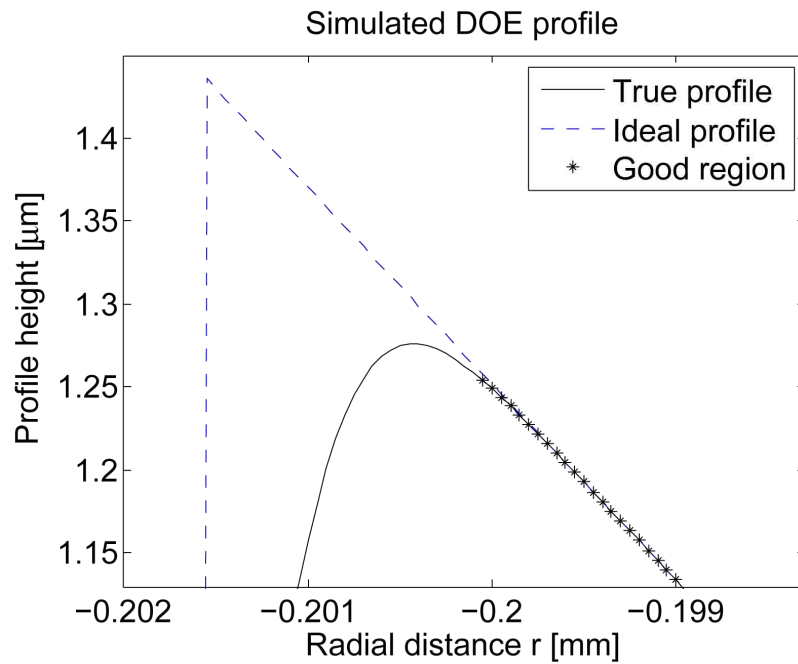


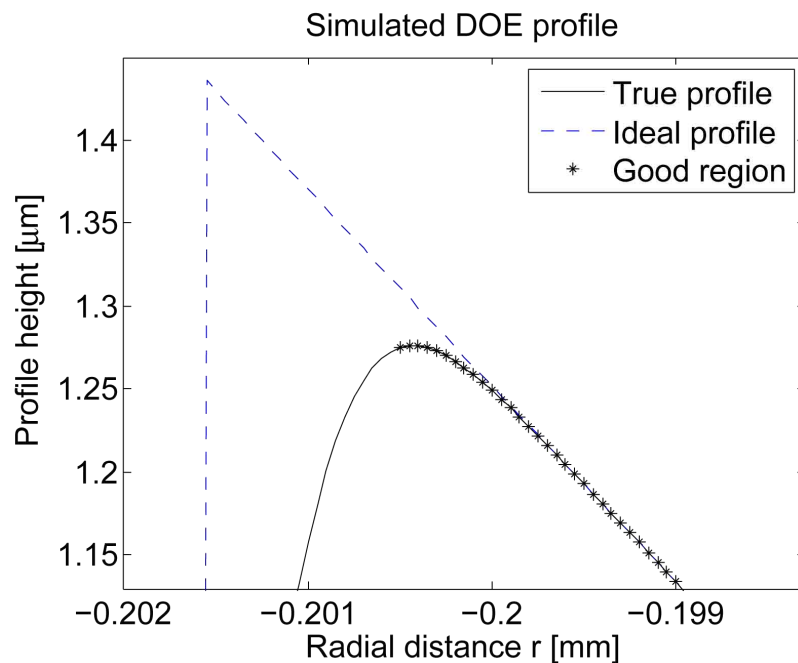
Figure 5.3.14: The picture shows the ideal DOE profile and the true profile close to the outer edge of the DOE. The stars indicate the regions where the slope of the true profile does not deviate more than $20 \text{ nm}/\mu\text{m}$ from the slope of the ideal profile. Then, the effective good area of the DOE is 86% of the total DOE area, *i. e.*, matching the diffraction efficiency from the simulations.

In figures 5.3.13 and 5.3.14 we observe that the regions defined as "good" (by the requirement that the good area divided by the total area equals the diffraction efficiency) are simply what one would have guessed without prior knowledge. The good area of the DOE is therefore a rather intuitive measure of the diffraction efficiency. The DOE efficiency can easily be estimated from the simple principle that the power found in the principal diffraction order equals the power impinging on "good" areas of the DOE.

Finally, it is instructive to compare the good area of 86% with an area of, say, 90%, in order to see if there is any observable difference on the microscopic level. In figure 5.3.15, a zoom-in on one of the DOE teeth is shown for the 86% and the 90% good area case, respectively.



(a) Good area of 86%.



(b) Good area of 90%.

Figure 5.3.15: A comparison of the "good regions" of the DOE profile giving a total good area of 86% and 90%, respectively. In the 90% case, the good region of the profile appears to be overestimated. The 86% case seems to be a proper estimation of the good regions, just from intuition. Thus, the method is rather sensitive, so that the diffraction efficiency can be estimated from the profile shape, probably with only a few percent error. The idea of "good area" is a simple way to illustrate how the diffraction efficiency is related to the shape of the profile.

As can be seen in the figure, the 86% case seems to match what one would intuitively count as the good region of the profile, whereas in the 90% case, the region defined as good appears to be too wide. Hence, the method of "good area" is quite sensitive, and may be used to estimate the DOE efficiency with rather high precision, and to provide a simple model of how a non-ideal shape of the DOE gives rise to a certain diffraction efficiency.

5.3.7 Renewed investigation of DOE focal length

In section 5.1.3, the focal lengths of the four different DOEs were measured. The results indicated that the *relative* focal lengths are very close to the design values, but a deviation of 7-10% from the *absolute* design values were observed. Therefore, it is interesting to extract the same information from the interferograms taken at the wavelength $\lambda = 632$ nm, and compare to simulations with the model described in sections 5.3.2 and 5.3.3.

In figure 5.3.16, the result from a simulation of the locations of the DOE focal points is shown, using the DOE profile found through the fitting algorithm for σ explained in the preceding sections. The linear fitting shown in the figure gives a focal length of -3.84 mm. The expected focal length is -3.72 mm, calculated as a scaling of the design focal length at 770 nm, using the paraxial formula from equation (5.1.2). So, the (absolute value of the) focal length is underestimated by 3.2% by the paraxial model of the DOE, compared to the more robust simulation.

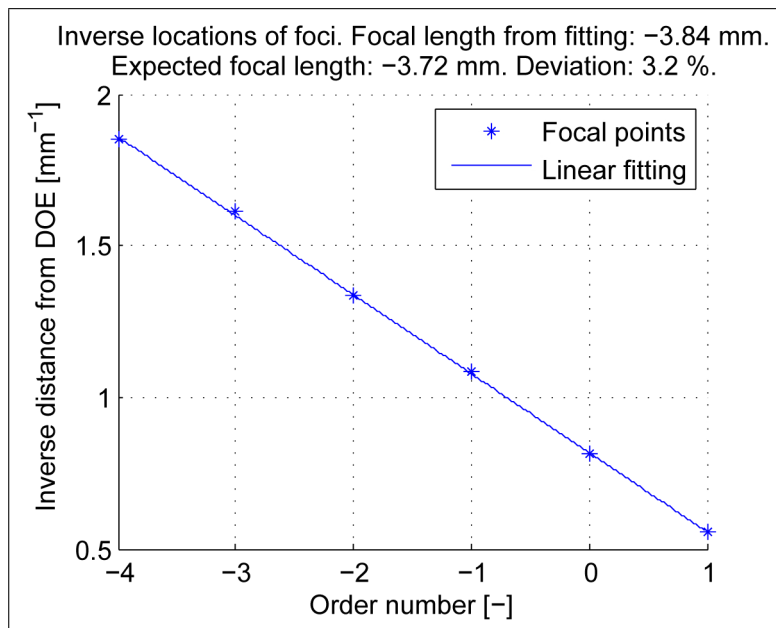


Figure 5.3.16: The picture shows the simulated locations of the DOE foci at $\lambda = 632$ nm. The slope of the linear fitting curve corresponds to a focal length of -3.84 mm.

In figure 5.3.17, the measured locations (captured from the interferograms) of the foci for DOE C1 is displayed. In this case, the linear fitting gives a focal length of -3.81 mm. When compared to the expected value of -3.72 mm, the deviation is now 2.5%.

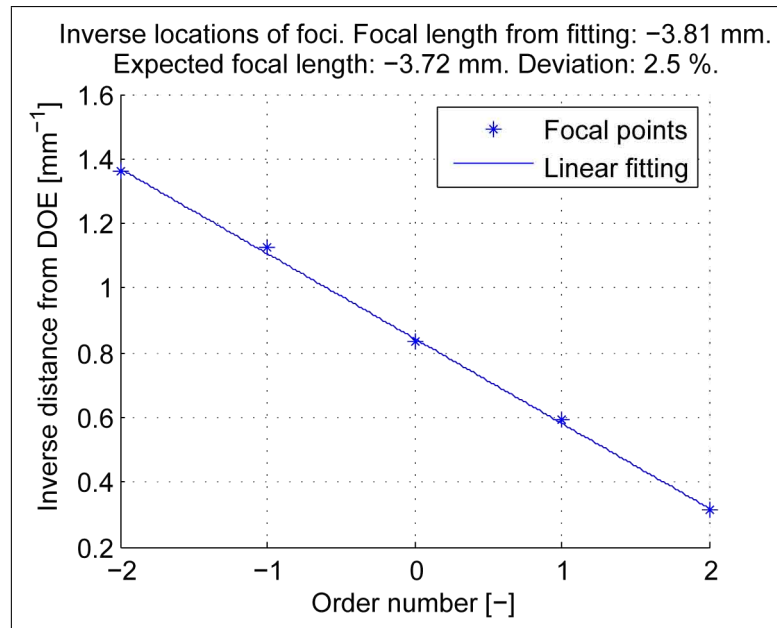


Figure 5.3.17: The picture shows the measured locations of the DOE C1 foci at $\lambda = 632$ nm. The slope of the linear fitting curve corresponds to a focal length of -3.81 mm.

As the slopes of the curves in figure 5.3.16 and 5.3.17 are very similar (they deviate by only 0.8%), we conclude that the focal length of the fabricated DOE is very close to the design value. The measured locations of the foci are found very close to the points in the simulation.

To sum up, this investigation clearly confirms that the focal length of the first DOE (C1) is very close to the design value. The measurement presented in section 5.1 showed a systematic error of 7-10% in the detected focal lengths, but when normalized to the measured focal length of DOE C1, all four focal lengths of DOEs C1-C4 were essentially correct, compared to the normalized design values. Thus, the combined results of these two experiments strongly support the conclusion that the focal lengths of all four physical DOEs are very close to the intended design values.

The simple paraxial model has been seen to underestimate the focal lengths by a few percent (at $\lambda = 632$ nm). This may partly explain the observed errors of 7-10% in section 5.1, but measurement errors were probably also contributing to the deviations, as discussed earlier.

5.3.8 DOE profile depth

The results from both the AFM measurement and the simulations presented in figure 5.3.10 suggest that the diffraction efficiency may be increased if the DOE profile can be made deeper. A simulation of the diffraction efficiency as function of the maximum DOE depth is shown in figure 5.3.18. The DOE model has been modified so that its ideal depth is increased by some factor before the convolution with the Gaussian function is carried out. Hence, the curvature of the DOE has not been changed.

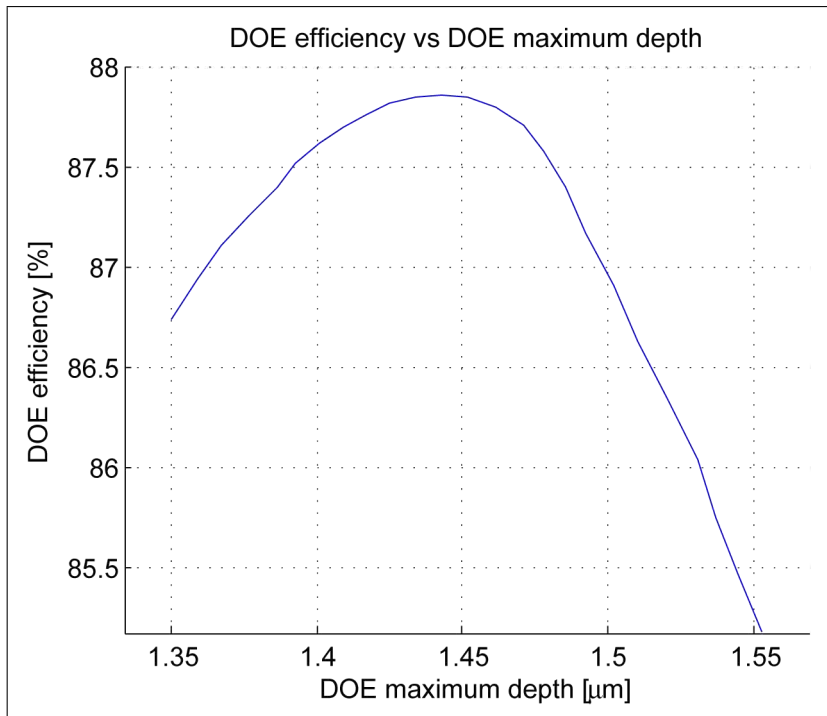


Figure 5.3.18: The DOE diffraction efficiency vs the maximum depth of the physical DOE. The present DOE has a maximum depth of $1.34 \mu\text{m}$. It is seen that the efficiency could be increased to about 87.9% (*i. e.*, 1.7 percentage points) if the maximum depth is increased to $1.442 \mu\text{m}$, which is essentially equal to the ideal DOE depth $1.439 \mu\text{m}$.

The DOE has a maximum depth of $1.34 \mu\text{m}$ in the simulations. In figure 5.3.18, we observe that the efficiency is increased to about 87.9% (*i. e.*, 1.7 percentage points or 2%) if we change the maximum depth of the DOE to $1.442 \mu\text{m}$ (*i. e.*, 7.6%). This depth is close to the ideal profile depth, which is $1.439 \mu\text{m}$. The improvement in efficiency is not huge, but could be crucial in a laser cavity where all loss factors must be minimized (also, the DOE is traversed twice in one cavity round trip, so the improvement is twice as large as far as cavity loss is concerned).

The efficiency cannot reach 100% because the maximum depth is not the only deviation from the ideal shape – the depth still varies with the radial distance, and the rounding of all sharp edges also diffracts power into unwanted orders. In figure 5.3.19, a theoretical simulation of the relative powers in the diffraction orders as function of wavelength for the *ideal* DOE is shown. The simulation was carried out by Dr. Johan Backlund at Alfa Exx.

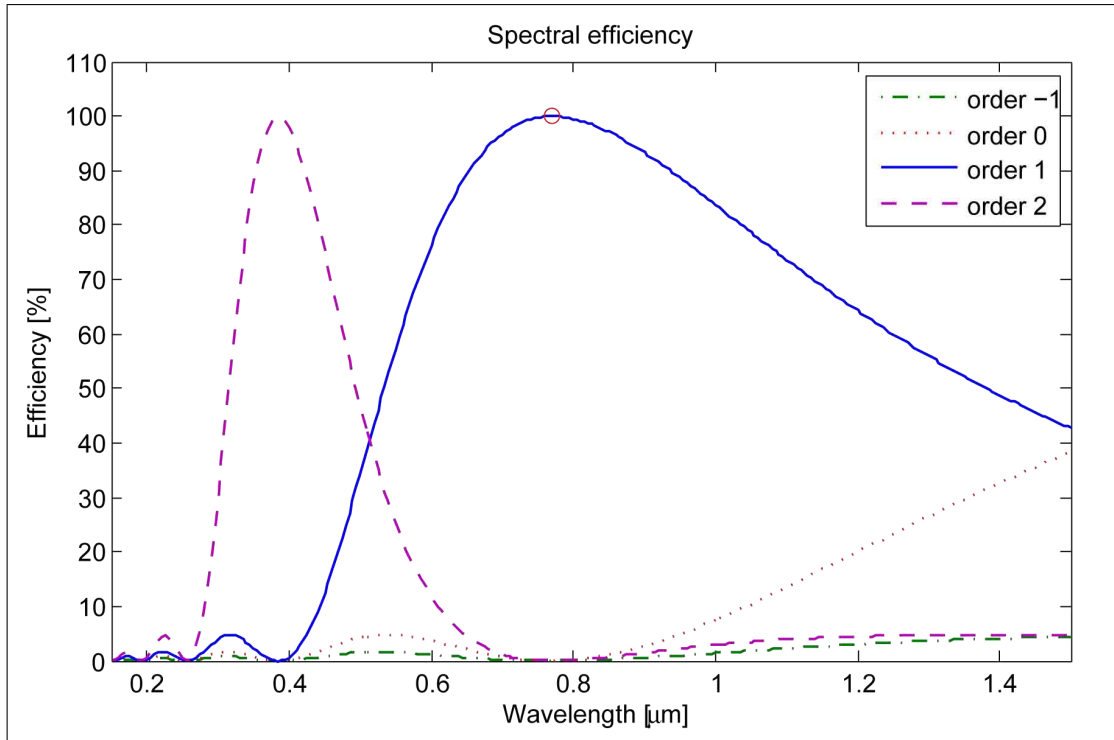


Figure 5.3.19: A simulation of the relative powers in the diffraction orders of an ideal DOE, designed for $\lambda_0 = 770$ nm. The simulation was performed by Dr. Johan Backlund in 2006.

The maximum depth of the simulated DOE is about 7.6% smaller than the ideal depth. This error can equally well be interpreted as a "wavelength error", and as the DOE then appears to be too shallow for the 770 nm light, the synonymous situation is a DOE with correct depth but a 7.6% longer wavelength, *i. e.*, 829 nm. Figure 5.3.19 then predicts that the diffraction efficiency should be reduced by 1.7% compared to the case at 770 nm. This is not far away from the simulated improvement of 2% when the DOE profile is made 7.6% deeper.

5.3.9 Discussion and summary

It can be concluded that a robust interferometric measurement method for the DOE efficiency has been developed, and that the investigated DOE has a diffraction efficiency of about 86% (without Fresnel reflections). This efficiency value is very good, and if the DOE is used in the ECL cavity, an operational laser can most likely be built. The efficiency can probably be increased by 1 percentage point if the DOE profile depth is adjusted. The simulated improvement is in good agreement with the prediction from a theoretical model of the diffraction efficiency as function of wavelength.

The method for measuring the efficiency of a diffractive optical element through self-interference described here, can be generalized to virtually any kind of structure, as long as the different orders overlap to form an interference pattern. The model may then be governed by more than one parameter, and the interferograms may not have circular symmetry, but this only adds some complexity and makes the calculations more time-consuming. But the concept can still be applied as rather a general method for characterization of diffractive structures having overlapping diffraction orders.

It has also been shown that the DOE focal lengths are very close to their design values. The discrepancy found in section 5.1 can probably be explained by shortcomings of the experimental method and the paraxial model. The interferometric data measured at $\lambda = 632$ nm have been analyzed, and this reveals that the focal length of DOE C1 lies only 0.75% from the design value. Consequently, the observations made in section 5.1 strongly indicate that the focal lengths of all four DOEs are correct, due to the fact that the focal lengths normalized to that of DOE C1 are very close to design values.

Chapter 6

Discussion

The various results and the advantages and shortcomings of the different measurement and evaluation methods, as well as the theoretical models, have been discussed extensively in each section of this report. Here, the results will be discussed on a more general level, and a few of the important results will be commented upon.

Lateral shear interferometer

The lateral shear interferometer designed for beam characterization has been tested on a known laser source, and the results indicate that the interferometer works properly. In the initial measurements, the beam divergence was measured at zero shear, whereas the wavefront radius of curvature was of course measured at some shear angle. However, the beam is strictly not unaffected by the shearing. Hence, a better way to determine the beam divergence is to block one of the two beams at some convenient position in the interferometer, but keeping the shear angle constant. This method was applied during the measurement on the known laser source in section 3.4.2.

Furthermore, the lateral shear was calculated from the shear angle of the shear plate in the first measurements. It turned out that this did not yield entirely correct results; a more robust way is to block each of the two beams in turn, and extracting their respective centroids from the CCD image. The distance between the centroids is the lateral shear. This methodology was used only in the experiments on the known laser source. The observation that the test measurement on a positive lens gave an error of 21% in the lens focal length may be explained by the fact that the two problematic procedures mentioned above were used.

DOE focal lengths

The experimental method for the DOE focal lengths was shown to work well, but some improvements have already been proposed. Most important is to align the components as well as possible. The DOE should also be index matched to the lens in order to avoid unnecessary Fresnel reflections. Further, the detection system should be automated by using a motorized translation stage, and perform computer analysis on the captured images. The fact that a laser with elliptical output beam was used as light source makes the foci less distinct, and it can be anticipated that better results can be achieved if a more uniform light source can be used.

DOE efficiency, direct measurement

The DOE efficiency has been measured by means of two different methods. The direct measurement technique had several drawbacks, especially the problem with reflections onto the monitor detector used for output power control, and the fact that the detector plays the role of an external mirror when inserted into the focus of the beam.

The errors introduced through the former phenomenon could be compensated to some extent by normalizing the measured power to the power corresponding to the momentary drive current via the *PI*-characteristics. However, the laser was operated just above the threshold in order not to saturate the detector, meaning that a small variation in drive current yields large variations in output power. If a laser having a lower threshold could be used, the compensation would probably be more accurate.

The latter problem was reduced when the aperture was mounted at a small distance from the detector surface, so that the reflected light was strongly truncated on its way back through the cavity. Nonetheless, the need for a detector at the focus, and requiring the output power to be held constant, makes the method cumbersome and unreliable. At the best, an estimation of the DOE efficiency can be made, but with an uncertainty of at least ± 5 percentage points.

DOE efficiency, interferometric measurement

The shortcomings of the direct measurement led to the development of an indirect method, which avoids both the need for constant power and the undesirable detector at the focus. The indirect measurement method – which is the second method for DOE efficiency determination developed in this project – is the self-interferometric technique described in section 5.3.

The self-interferometric measurement method has proven to be a powerful tool to study a diffractive structure having circular symmetry. However, as mentioned before, the concept is not limited to this special case; the only requirement is that the diffraction orders overlap spatially, so that an interference pattern will be formed (for instance, an ordinary diffraction grating cannot be examined this way). If the algorithms are adjusted at some points, the result may be a very general tool for optical characterization of diffractive optical elements.

The propagation method utilizes a two-dimensional description of the interference pattern, but when the comparison to measured data is made, the interferograms are given a one-dimensional representation, in order to save calculation time. By generalizing the fitting algorithm so that two-dimensional data can be handled, the method is ready to be applied to many kinds of diffractive structures. The description of the diffractive surface itself must of course be tailored for the specific element used, and may contain multiple variables.

There are still problems with the evaluation algorithm that may be studied. The sampling problem is always present and is difficult to get rid of, and the cause of the numerical disturbances observed in the simulations has not been found. Perhaps the filtering procedures can be improved in different ways.

Chapter 7

Conclusions

This master thesis has focused on developing measurement and analysis techniques for the characterization of the cavity components of the ECL prototype at Alfa Exx. The external mirror, the semiconductor optical amplifier and the diffractive optical element have been the subject for investigation. The conclusions from measurements and simulations are briefly presented in this chapter.

7.1 ECL concept and functional prototype

A literature survey has been conducted in order to search for ECL designs similar to the patent [1]. No concept relying on longitudinal cavity dispersion provided by a diffractive optical element has been found in research publications. Of course, the survey has not been very extensive, and company R&D results are seldom published, but to the author's knowledge, the concept [1] is still unique.

A functional prototype of the laser was built in 2007. In the thesis work at Alfa Exx, a new test setup for increased stability and functionality has been designed, and necessary parts have been ordered or fabricated. The new setup has not been tested so far, but the parts are available and the setup is ready to be assembled. It is believed that the more robust setup will make the wavelength tuning more stable and repeatable, and it is not unlikely that the laser then will show better performance.

7.2 Spectrometer and external mirror

The sensitivity of a spectrometer intended for spectral measurement on the ECL has been measured, and a calibration function has been calculated. A fiber with angled end facets, for reduced backward reflections into the laser, was used to couple light into the spectrometer.

The external mirror has been spectrally examined, and has been proven to fulfil its specifications, having a reflectance $\geq 87\%$ in the relevant wavelength region around 770 nm. However, it has also been suggested that the laser performance may be improved by choosing a mirror of slightly higher reflectance.

7.3 Characterization of SOA

In order to quantify the beam characteristics of the semiconductor optical amplifier (SOA) used as gain medium in the ECL, a white-light compensated lateral shear interferometer of a modified Jamin type has been designed, assembled and tested on a known laser source. Evaluation algorithms for interpretation of interferograms and intensity measurements have been developed.

The Gabor transform is utilized to identify the spatial frequency of the interference pattern, and a Gaussian beam description was employed to calculate the beam characteristics of the source. The beam parameters of

the reference laser were measured with the interferometer and compared to specifications and direct measurements of beam divergence, and the interferometer was shown to extract the unknown entities correctly.

The interferometer is intended to be used for characterization of the ECL output beam under lasing conditions. It has not been possible to conduct this experiment in the master thesis project, but it is a necessary step to take in order to be able to compensate for expected astigmatism and non-uniform beam divergence of the SOA.

7.4 Characterization of DOE

In this project, much attention has been given to the diffractive optical element (DOE) used to provide the cavity dispersion in the ECL. Four different DOE designs were developed and fabricated at the clean-room facility at MC2 a few years ago, and it has been desirable to verify that the **focal lengths** of the DOEs match the intended design focal lengths. Even more important, the DOE **diffraction efficiency** is a crucial parameter of the ECL, as it probably represents the major source of cavity loss, and it has therefore been extensively investigated.

7.4.1 DOE focal lengths

A paraxial model of the DOE was set up, giving the locations of the different diffraction order foci on the optical axis for a DOE of a certain design focal length f_0 . The focal points were experimentally measured by means of a rather simple setup, and the captured data were compared to the model, resulting in focal length estimations that were 7-10% smaller than the design values.

When using normalized focal lengths (normalizing to the measured and design value of the DOE of largest focal length (C1), respectively), the agreement between experiment and design data was almost total. The deviations in absolute focal lengths can probably be explained from systematic errors in the measurement setup (misalignments, lack of index matching of the DOE, etc.), and difficulties in detecting the focal points correctly. It has also been shown that the paraxial model may introduce small errors.

7.4.2 DOE efficiency

Direct measurement method

Two different methods for quantification of the DOE efficiency have been developed and evaluated. The first relies on a direct measurement of the absolute power at the DOE surface and in the first diffraction order focus, by means of an integrating detector, and using an ordinary edge-emitting laser as light source. The results indicate an efficiency in the range 75-80%, but this figure contains large uncertainties.

One shortcoming of the method is the unavoidable backward reflection from the detector surface, which will reach the monitor detector used for active control of the laser output power. Another – perhaps even more severe – issue is the fact that the detector itself will act as an external mirror when placed at the focal point. The measured output power will vary unpredictably due to resonant effects in the coupled cavity (external cavity plus the internal laser cavity itself).

Self-interferometric method

The unreliability of the first estimation of the DOE efficiency led to the conclusion that a more robust measurement method must be found. Consequently, the largest task of this project has been to develop an indirect measurement method relying on the self-interference between the diffraction orders of the DOE. The technique eliminates the need for keeping the laser power constant, and avoids the unpleasant demand that detection equipment be positioned at the main focal point.

A theoretical model of the physical DOE was constructed, approximating the true DOE profile as the ideal profile convolved with a Gaussian function of width σ . Hence, the DOE shape is governed by only one

parameter, a model that proved to be in good agreement with the general behavior of the DOE depth as function of radial distance from the center, found from earlier AFM measurements. Further, a measurement setup was designed and assembled, and then the "two-step method" [41] was used to simulate the propagation of light from the DOE through the entire system to a CCD camera.

Interferograms were recorded, and the simulation algorithms were utilized to generate synthetic interferograms corresponding to the measurements. The parameter σ determining the DOE shape was adjusted until the best fitting of the model to the measured data was found.

As the experiment was conducted at $\lambda = 632$ nm, the situation at the design wavelength $\lambda_0 = 770$ nm was simulated, resulting in a diffraction efficiency of 86%. The different contributions to the total efficiency were summarized in table 5.3 and are repeated here in table 7.1 for convenience.

Table 7.1: Summary of the contributions to the overall DOE efficiency at the design wavelength $\lambda_0 = 770$ nm. The diffraction efficiency is due to the corner rounding, with resulting profile depth error. The total efficiency is estimated to be 81%

	Loss factor	Efficiency factor	Overall efficiency
Incident power	–	–	100%
Truncation	$\sim 0\%$	$\sim 100\%$	100%
Fresnel reflection	4.5%	95.5%	95.5%
Diffraction efficiency	13.8%	86.2%	82.3%
Absorption	$\sim 0\%$	$\sim 100\%$	82.3%
Diffusive spread	$\sim 0\%$	$\sim 100\%$	82.3%
Dust/contaminations	$< 0.5\%?$	$> 99.5\%?$	$> 81.9\%$
Index mismatches	$< 0.3\%$	$> 99.7\%$	$> 81.7\%$
Non-ideal lens AR coating	$< 0.4\%$	$> 99.6\%$	$> 81.3\%$
TOTAL	19%	81%	81%

The estimated *overall DOE efficiency* is $81 \pm 2\%$, with all loss factors included. This value was found for the case of an incident Gaussian intensity distribution, with an $1/e^2$ half-width of 0.17 mm. The efficiency becomes lower if the incident intensity distribution is wider, due to the fact that more power is transmitted through the outer region of the DOE, where the corner rounding has a more severe effect. The direct measurement method resulted in an efficiency $77 \pm 5\%$ (see table 5.2). The two methods therefore give overlapping results.

The DOE profile obtained from the model is only 5-10% away from the profile obtained in the AFM measurement performed by Dr. Johan Backlund [40]. Hence, the DOE has been shown to have a high diffraction efficiency (the pure diffraction efficiency is about 86% as mentioned earlier), and the experimental method developed can be generalized to work for other kinds of diffractive elements as well. It can definitely be expected that a functional ECL can be built with this DOE as dispersive element.

The diffraction efficiency can be slightly improved by making the DOE profile $\sim 8\%$ deeper. Addition of an anti-reflection coating to the diffractive structure will strongly suppress the 4.5% Fresnel reflection, which is quite a large an improvement. In order to further approach 100% diffraction efficiency, the manufacturing process itself must be improved, to produce sharper edges, and therefore better profile depth. Perhaps other material systems may be considered, or even a different manufacturing technique, avoiding some of the shortcomings and limitations of the E-beam.

DOE good area

One way to understand the mechanisms behind the diffraction efficiency is to divide the DOE profile into "good" and "bad" regions, respectively. In the good regions, the slope of the physical DOE profile is very close to the ideal slope, and the opposite is true for the bad regions. The fraction of the total area that can be considered as "good" has been shown to be roughly the same as the diffraction efficiency.

The result can be understood by realizing that the good area will send optical power into the principal diffraction order, whereas the bad areas will scatter power into all other orders. All area measures must be weighted by the incident intensity distribution in order to account for the fact that the diffraction efficiency is actually a local figure of merit, and varies with the radial coordinate of the DOE.

DOE focal length from robust model

Finally, the more precise model of the DOE described above was compared to the paraxial model of the DOE, used to determine the effective focal lengths. It was shown that the paraxial model underestimates the focal lengths by about 3% at the wavelength 632 nm. Also, the interferometric data captured were used to calculate the focal length of DOE C1 at $\lambda = 632$ nm, from the locations of the focal points.

The observed positions of the focal points of DOE C1 in the interferometric measurement setup were found to be very close to the positions predicted by simulations with the robust DOE model and the two-step method. This result, combined with the fact that the *normalized* focal lengths found in section 5.1.2 were essentially correct, gives strong evidence for the conclusion that all four fabricated DOEs have indeed reached the desired design specifications, as far as focal length is concerned.

Chapter 8

Further research

The lateral shear interferometer designed during this project has so far not been used to quantify the astigmatism and beam parameters of the SOA. An important step to take is therefore to assemble the entire laser cavity (though perhaps without the DOE), with the SOA as light source, using the improved stable test setup. This includes a collimating lens, so that a well-behaved output beam can be formed.

The beam can be coupled into the interferometer, and the properties of the SOA can be revealed through measurements on the beam under lasing conditions, in combination with reverse calculations through the system. When the beam characteristics of the gain medium are known, modifications of the cavity can be proposed in order to compensate for any asymmetric behavior.

If the SOA investigation reveals that some compensation must be introduced, a new DOE and/or lenses need to be designed (and fabricated). Then, the diffraction efficiency can be increased by roughly 1 percentage point by increasing the DOE depth. Also, by using an anti-reflection coating on the diffractive surface, the efficiency could probably be improved by perhaps 3 percentage points, ending up with a DOE having a true efficiency of 86% in the cavity.

During the experiments conducted a few years ago, the DOE was not index matched to the lens L_2 . This implies two extra Fresnel reflections per cavity roundtrip, which of course means increased cavity loss, and the reflections may also cause disturbances to the field distribution, which may lead to unexpected behavior of the laser. Index matching the DOE is an obvious measure that must be taken, and the effect of this action should be studied.

Most of the cavity components have now been characterized, and this information may be utilized to calculate a (complex) effective coefficient of reflectivity representing the entire (passive) external cavity (the gain medium excluded). This reflectivity is a function of the transverse coordinates at the output facet of the gain chip, and the wavelength.

The behavior of the entire laser may be simulated as a semiconductor waveguide with one end facet described by a complex reflectivity. Using known information about the gain chip (and eventually measured parameters), the behavior of the entire cavity can be studied. It may turn out that the unexpected observations then can be explained, perhaps from the elliptical/astigmatic properties of the gain medium, interfering diffraction orders from the DOE or something else.

The ultimate goal is to verify mode-hop free wavelength tuning over a substantially wider wavelength range than 10 nm, and the steps outlined above are assumed to bring the laser closer to this goal. If the target is reached, the laser may be commercialized. A new design project will then be necessary to specialize the laser for some specific application. Finally, the laser must be miniaturized, and made robust enough for cheap and easy fabrication and assembly.

As mentioned earlier, the self-interferometric method for characterization of the DOE profile can be generalized to suit diffractive elements of various designs, as long as the diffraction orders overlap spatially so that an interference pattern is formed. It would therefore be of interest to develop a DOE model governed by more than one parameter, and to adjust the calculation methods so that interferograms lacking circular symmetry could be handled, *i. e.*, utilizing the information from the entire two-dimensional interferograms.

Appendix A

Theoretical derivations

A.1 Interpreting a lateral shear interferogram

The relation between the spatial period Λ of a lateral shear interferogram and the wavefront radius of curvature R is derived in the following. Assume that the wavefront is spherical. It can then be described as a function of y :

$$W(y) = \sqrt{R^2 - y^2} \quad (\text{A.1.1})$$

where R is the wavefront radius of curvature. In a lateral shear interferometer, the interference fringes are approximately given by [35]:

$$S \cdot \left. \frac{\partial W}{\partial y} \right|_{y=y_m} = m\lambda; \quad m \in \mathbb{Z} \quad (\text{A.1.2})$$

where S is the lateral shear and λ is the optical free space wavelength. This approximative formula is valid when the lateral shear $S \rightarrow 0$. From equation (A.1.1) we find that

$$\frac{\partial W}{\partial y} = \frac{y}{\sqrt{R^2 - y^2}} = \frac{y/R}{\sqrt{1 - \frac{y^2}{R^2}}} \quad (\text{A.1.3})$$

Now, in the paraxial approximation, we require that $|y| \ll |R|$, so that $y^2/R^2 \ll 1$, and equation (A.1.3) can be approximated by

$$\frac{\partial W}{\partial y} \approx \frac{y}{R}; \quad |y| \ll |R| \quad (\text{A.1.4})$$

Insertion in equation (A.1.2) gives:

$$\frac{y_m}{R} S = m\lambda \Leftrightarrow R = \frac{S}{\lambda} \cdot \frac{y_m}{m}; \quad m \in \mathbb{Z} \quad (\text{A.1.5})$$

Here, the entity y_m/m is nothing but the spatial period of the fringe pattern, Λ . Therefore, the wavefront radius of curvature in terms of the spatial period is given by:

$$R = \frac{S\Lambda}{\lambda}. \quad (\text{A.1.6})$$

A.2 Paraxial model of lens and DOE

Here, a paraxial model for the second cavity lens plus the DOE is derived. The lens is displayed in figure A.2.1, in the case of collimated light incident on the lens from the left. The physical lens is shown in the picture, but all rays are assumed to be refracted in the principal plane of the lens.

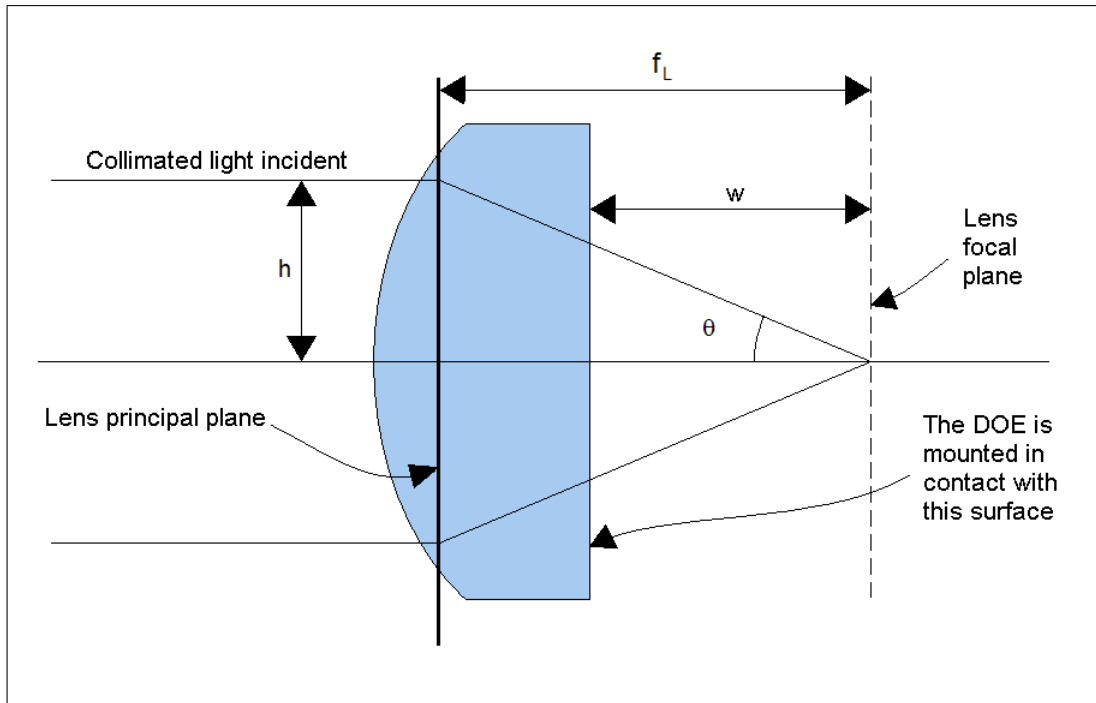


Figure A.2.1: The second cavity lens in the case of collimated light incident from the left.

In the paraxial case, we assume that all angles are sufficiently small, so that the approximation $\sin \delta \approx \tan \delta \approx \delta$ can be used. In figure A.2.1, we can therefore see that

$$\frac{h}{f_L} = \tan \theta \approx \theta. \quad (\text{A.2.1})$$

The ray emerging from the lens into air thus has an angle θ with respect to the optical axis. The DOE is then positioned in contact with the lens back surface (the plane surface of the plano-convex lens). If we assume an infinitesimally thin air gap between the lens and the DOE, the ray traveling under the angle θ is refracted to a new angle ϕ inside the DOE substrate, according to Snell's law. This situation is depicted in figure A.2.2.

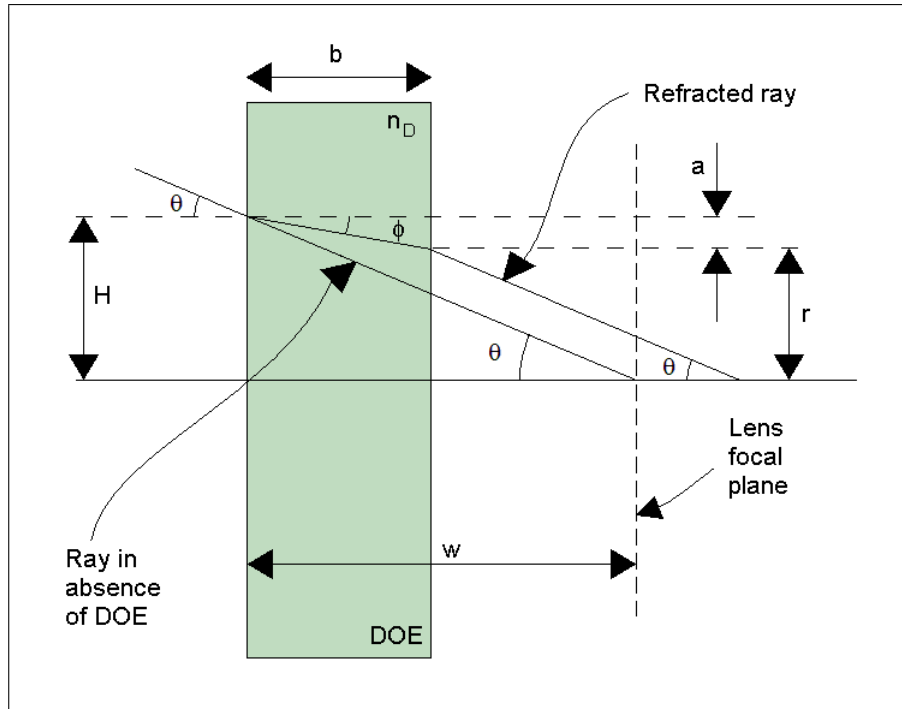


Figure A.2.2: The effect of refraction in the DOE surface, causing a change in the angular distribution of light hitting the diffractive structure on the right-hand side of the DOE.

Thus, the angle ϕ inside the DOE substrate is given by

$$\sin \theta = n_D \sin \phi \Rightarrow \theta \approx n_D \phi, \quad (\text{A.2.2})$$

again using the paraxial approximation. The effect of the DOE having a thickness b can be quantified by locating the point where the refracted ray hits the diffractive surface, *i. e.*, the distance r in figure A.2.2. Using the notations of the figure, it can be seen that

$$r = H - a = w \tan \theta - b \tan \phi \approx w \theta - b \phi = \theta \left[w - \frac{b}{n_D} \right] = \frac{h}{f_L} \left[w - \frac{b}{n_D} \right] \quad (\text{A.2.3})$$

where equations (A.2.2) and (A.2.1) were used. Now, to understand the effect of the DOE itself (the diffractive surface), consider figure A.2.3.

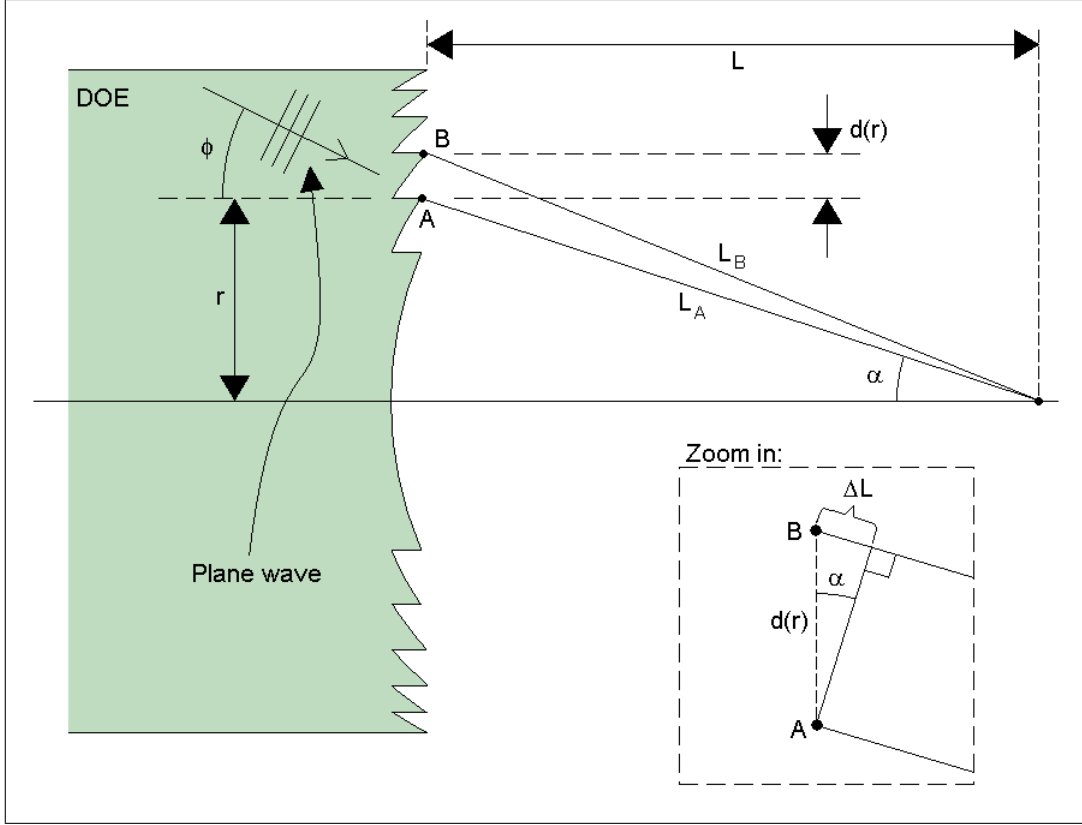


Figure A.2.3: The effect of the diffractive surface of the DOE. The point sources A and B are not in phase due to the incident wave traveling at angle ϕ . A focus is formed when the phase difference arising from the optical path difference ΔL and the initial phase difference add up to a multiple of 2π .

In figure A.2.3, $d(r)$ is the local period of the DOE at the distance r from the optical axis. We assume that $d \ll r$ and $r \ll L$, so that the two rays are approximately parallel. The zoom in picture shows the optical path difference ΔL between the rays traveling from points A and B to the point on the optical axis at distance L from the DOE surface. We find that

$$\Delta L = d \sin \alpha \approx d \alpha \quad (\text{A.2.4})$$

and

$$\frac{r}{L} \approx \tan \alpha \approx \alpha. \quad (\text{A.2.5})$$

Using equation (A.2.5) in equation (A.2.4), we arrive at

$$\Delta L \approx \frac{rd}{L}. \quad (\text{A.2.6})$$

Furthermore, we observe in figure A.2.3 that the point A will have a phase delay compared to point B , as point A will be reached by the incident wave slightly later in time compared to point B . Letting the phase of point B be $\gamma_B = 0$, the phase of point A is given by:

$$\gamma_A = n_D k_0 d \sin \phi \approx n_D k_0 d \phi = n_D k_0 d \frac{\theta}{n_D} = k_0 d \theta = \frac{h}{f_L} k_0 d \quad (\text{A.2.7})$$

where equations (A.2.2) and (A.2.1) were used once more.

We can now calculate the phase difference $\Delta\psi$ between rays A and B , when they meet on the optical axis, a distance L from the DOE surface:

$$\Delta\psi = \gamma_A - \gamma_B - k_0\Delta L = \frac{h}{f_L}k_0d - 0 - k_0\frac{rd}{L} = \frac{h}{f_L}k_0d - k_0\frac{rd}{L} \quad (\text{A.2.8})$$

and, using equation (A.2.3), to substitute h/f_L we get:

$$\Delta\psi = \frac{h}{f_L}k_0d - k_0\frac{rd}{L} = \frac{rk_0d}{w - \frac{b}{n_D}} - k_0\frac{rd}{L} = rdk_0 \left[\frac{1}{w - \frac{b}{n_D}} - \frac{1}{L} \right]. \quad (\text{A.2.9})$$

We must now relate r and d to the effective focal length of the DOE. To this end, consider figure A.2.4.

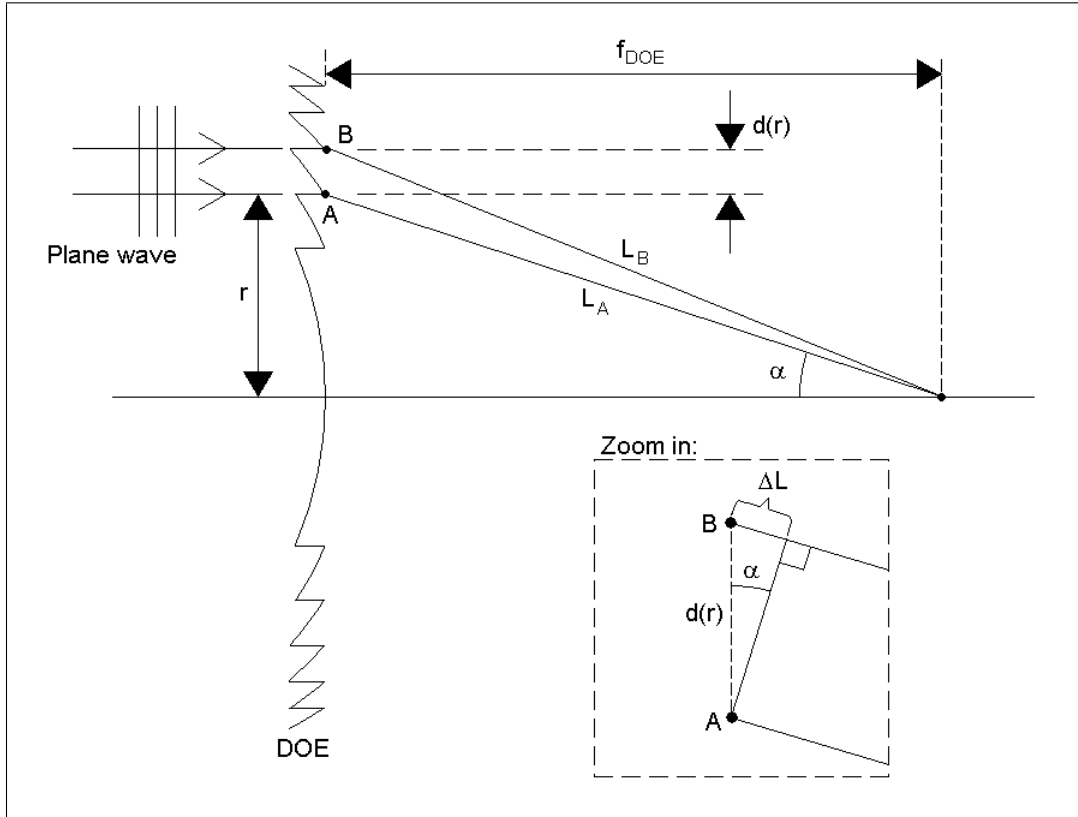


Figure A.2.4: A DOE acting as a positive lens, where the optical path difference between rays A and B is equal to one wavelength at the focal point.

The DOE in figure A.2.4 acts as a positive lens for simplicity. A DOE of negative focal length has a virtual focus to the left of the surface instead; the calculations are identical. Requiring that a plane wave incident from the left is focused a distance f_{DOE} away, the path difference between the rays must equal one wavelength. Hence,

$$\Delta L = d \sin \alpha \approx d\alpha = \lambda \quad (\text{A.2.10})$$

and

$$\frac{r}{f_{DOE}} \approx \tan \alpha \approx \alpha. \quad (\text{A.2.11})$$

Now, we use equation (A.2.11) in equation (A.2.10), which yields:

$$\lambda = d\alpha = d \frac{r}{f_{DOE}} \Leftrightarrow rd = \lambda f_{DOE}. \quad (\text{A.2.12})$$

In the case of a negative focal length, we use $-f_{DOE}$ instead in the equation above. Using this relation in equation (A.2.9), we finally arrive at:

$$\Delta\psi = -\lambda f_{DOE} k_0 \left[\frac{1}{w - \frac{b}{n_D}} - \frac{1}{L} \right] = -2\pi f_{DOE} \left[\frac{1}{w - \frac{b}{n_D}} - \frac{1}{L} \right] = N \cdot 2\pi; \quad N \in \mathbb{Z}, \quad (\text{A.2.13})$$

so that the DOE foci are found when the phase difference is a multiple of 2π . Solving for $1/L$ in equation (A.2.13), we get an expression for the (inverse of the) locations of the DOE foci:

$$\frac{1}{L_N} = \left(w - \frac{b}{n_D} \right)^{-1} + \frac{N}{f_{DOE}}; \quad N \in \mathbb{Z}; \quad f_{DOE} < 0. \quad (\text{A.2.14})$$

The principal focus is found for $N = 1$, and the zeroth order $N = 0$ represents a wave that has not been diffracted at all, *i. e.*, this focus would be the one observed in absence of the diffractive structure on the glass substrate.

It should be noted that in equation (A.2.12), the product rd is constant (because the product λf_{DOE} is constant for an arbitrary wavelength λ). This means that the focal length of the DOE is inversely proportional to the wavelength:

$$f_{DOE}(\lambda) = \frac{rd}{\lambda} = \left(\frac{\lambda_0}{\lambda} \right) f_0, \quad (\text{A.2.15})$$

where $f_{DOE}(\lambda)$ is the focal length at wavelength λ , and f_0 is the focal length at the design wavelength λ_0 . Hence, the DOE acts as a stronger lens ($|f_{DOE}|$ is smaller) for longer wavelengths.

Bibliography

- [1] Swedish patent no 0201732-5, Resonator.
- [2] T. H. Maiman, "Stimulated optical radiation in ruby," *Nature*, vol. 187, no. 4736, pp. 493–494, 1960.
- [3] R. N. Hall, G. E. Fenner, J. D. Kingsley, T. J. Soltys, and R. O. Carlson, "Coherent Light Emission From GaAs Junctions," *Phys. Rev. Lett.*, vol. 9, no. 9, pp. 366–369, 1962.
- [4] B. Mroziewicz, "External cavity wavelength tunable semiconductor lasers - a review," *Opto-Electron. Rev.*, vol. 16, no. 4, pp. 347–366, 2008.
- [5] G. P. Agrawal, *Lightwave technology: telecommunication systems*. Hoboken, New Jersey: John Wiley & Sons, Inc., 2005.
- [6] J. Buus, M. Amann, and D. J. Blumenthal, *Tunable Laser Diodes and Related Optical Sources*. Hoboken, New Jersey: John Wiley & Sons, Inc., 2 ed., 2005.
- [7] C. Ye, *Tunable External Cavity Diode Lasers*. Singapore: World Scientific Publishing Co. Pte. Ltd, 2004.
- [8] New Focus (Newport Corp.). www.newfocus.com.
- [9] Thorlabs. www.thorlabs.com.
- [10] J. Buus, "Tunable laser sources for (D)WDM," *Proc. SPIE Int. Soc. Opt. Eng.*, vol. 5280, pp. 172–181, 2004.
- [11] A. D. White, "Reflecting prisms for dispersive optical maser cavities," *Appl. Opt.*, vol. 3, no. 3, pp. 431–521, 1964.
- [12] A. Q. Liu and X. M. Zhang, "A review of MEMS external-cavity tunable lasers," *J. Micromech. Microeng.*, vol. 17, pp. R1–R13, 2007.
- [13] F. J. Duarte, ed., *Tunable Lasers Handbook*. San Diego: Academic Press, 2005.
- [14] A. Q. Liu, X. M. Zhang, D. Y. Tang, and C. Lu, "Tunable laser using micromachined grating with continuous wavelength tuning," *Appl. Phys. Lett.*, vol. 85, no. 17, pp. 3684–3686, 2004.
- [15] D. Anthon, J. D. Berger, J. Drake, S. Dutta, A. Fennema, J. D. Grade, S. Hrinya, F. Ilkov, H. Jerman, D. King, H. Lee, A. Tselikov, and K. Yasumura, "External cavity diode lasers tuned with silicon MEMS," *Proc. OFC 2002, Opt. Fiber Commun. Conf. Exhibit (Anaheim, CA, 17-22 March 2002)*, pp. 97–98, 2002.
- [16] V. Heikkinen, J. Aikio, T. Alajoki, J. Hiltunen, A. Mattila, J. Ollila, and P. Karioja, "Single-mode tuning of a 1540-nm diode laser using a Fabry-Perot interferometer," *IEEE Photon. Technol. Lett.*, vol. 16, no. 4, pp. 1164–1166, 2004.
- [17] Z. Xu, S. Zhang, Y. Li, and W. Du, "Adjustment-free cat's eye cavity He-Ne laser and its outstanding stability," *Opt. Express*, vol. 13, no. 14, pp. 5565–5573, 2005.
- [18] A. Jechow, V. Raab, R. Menzel, M. Cenker, S. Stry, and J. Sacher, "1 W tunable near diffraction limited light from a broad area laser diode in an external cavity with a line width of 1.7 MHz," *Opt. Comm.*, vol. 277, no. 1, pp. 161–165, 2007.
- [19] B. Liu, Y. Liu, and Y. Braiman, "Linewidth reduction of a broad-area laser diode array in a compound external cavity," *Appl. Opt.*, vol. 48, no. 2, pp. 365–370, 2009.

- [20] D. Chen, Z. Fang, H. Cai, and R. Qu, "Polarization Characteristics of an External Cavity Diode Laser With Littman-Metcalf Configuration," *IEEE Photonics Technol. Lett.*, vol. 21, no. 14, pp. 984–986, 2009.
- [21] L. Qi-Hong, D. Jing-Xing, Z. Jun, and W. Yun-Rong, "Line-width reduction of a laser diode array using an external cavity with two feedback mirrors," *Chin. Phys. Lett.*, vol. 24, no. 9, pp. 2587–2589, 2007.
- [22] D. Wandt, M. Laschek, K. Przyklenk, A. Tünnermann, and H. Welling, "External cavity laser diode with 40 nm continuous tuning range around 825 nm," *Opt. Comm.*, vol. 130, no. 1-3, pp. 81–84, 1996.
- [23] L. Nilse, H. J. Davies, and C. S. Adams, "Synchronous tuning of extended cavity diode lasers: the case for an optimum pivot point," *Appl. Opt.*, vol. 38, no. 3, pp. 548–553, 1999.
- [24] W. Sorin, P. Zorabedian, and S. Newton, "Tunable single-mode fiber reflective grating filter," *J. Lightwave Technol.*, vol. 5, no. 9, pp. 1199–1202, 1987.
- [25] J. H. Lee, M. Y. Park, C. Y. Kim, S. Cho, W. Lee, G. Jeong, and B. W. Kim, "Tunable external cavity laser based on polymer waveguide platform for WDM access network," *IEEE Photonics Technol. Lett.*, vol. 17, no. 9, pp. 1956–1958, 2005.
- [26] V. Crozatier, B. K. Das, G. Baili, G. Gorju, F. Bretenaker, J. L. Gouët, I. Lorgeré, and W. Sohler, "Highly coherent electronically tunable waveguide extended cavity diode laser," *IEEE Photonics Technol. Lett.*, vol. 18, no. 14, pp. 1527–1529, 2006.
- [27] E. Muller, W. Reichert, C. Ruck, and R. Steiner, "External-cavity laser design and wavelength calibration," *Hewlett-Packard J.*, vol. 44, no. 1, pp. 20–27, 1993.
- [28] J. D. Merlier, K. Mizutani, S. Sudo, K. Sato, and K. Kudo, "Wavelength channel accuracy of an external cavity wavelength tunable laser with intracavity wavelength reference etalon," *J. Lightwave Technol.*, vol. 24, no. 8, pp. 3202–3209, 2006.
- [29] J. D. Merlier, K. Mizutani, S. Sudo, K. Naniwae, Y. Furushima, S. Sato, K. Sato, and K. Kudo, "Full C-Band External Cavity Wavelength Tunable Laser Using a Liquid-Crystal-Based Tunable Mirror," *IEEE Photonic Tech. L.*, vol. 17, no. 3, pp. 681–683, 2005.
- [30] P. Zorabedian and W. R. Trutna, Jr., "Interference-filter-tuned, alignment-stabilized, semiconductor external-cavity laser," *Opt. Lett.*, vol. 13, no. 10, pp. 826–828, 1988.
- [31] L. Levin, "Mode-hop-free electro-optically tuned diode laser," *Opt. Lett.*, vol. 27, no. 4, pp. 237–239, 2002.
- [32] A. Bösel, K. Salewski, and T. Kinder, "Fast mode-hop-free acousto-optically tuned laser with a simple laser diode," *Opt. Lett.*, vol. 32, no. 13, pp. 1956–1958, 2007.
- [33] G. A. Coquin and K. W. Cheung, "Electronically tunable external-cavity semiconductor laser," *Electron. Lett.*, vol. 24, no. 10, pp. 599–600, 1988.
- [34] K. Vilhelmsson, "Summary, Geltech 350390 and 350390 with DOE_C1." Alfa Exx AB, 2009.
- [35] D. Malacara, ed., *Optical Shop Testing*. New York: John Wiley & Sons, Inc., 2 ed., 1992.
- [36] M. V. R. K. Murty, "Some modifications of the Jamin interferometer useful in optical testing," *Appl. Opt.*, vol. 3, no. 4, pp. 535–538, 1964.
- [37] R. Carmona, W.-L. Hwang, and B. Torrèsani, *Practical Time-Frequency Analysis, Volume 9: Gabor and Wavelet Transforms, with an Implementation in S (Wavelet Analysis and Its Applications)*. San Diego: Academic Press, 1998.
- [38] B. E. A. Saleh and M. C. Teich, *Fundamentals of Photonics*. Hoboken, New Jersey: John Wiley & Sons, Inc., 2 ed., 2007.
- [39] Newport Corporation. www.newport.com.
- [40] J. Backlund, "Evaluation of DOE lenses ECL C1-C4_20090311jb." Alfa Exx AB, 2006 (2009).
- [41] C. Rydberg and J. Bengtsson, "Efficient numerical representation of the optical field for the propagation of partially coherent radiation with a specified spatial and temporal coherence function," *J. Opt. Soc. Am. A*, vol. 23, no. 7, pp. 1616–1625, 2006.